Phosphate and Sulphate Polyanionic Materials for Insertion-type Storage Batteries

西尾, 陽

Phosphate and Sulphate Polyanionic Materials for Insertion-type Storage Batteries

Akira Nishio

Interdisciplinary Graduate School of Engineering Sciences

Kyushu University

February 2022

Table of Contents

Chapter 1

Introduction

1.1 Research Background

Nowadays, energy and sustainability issues are at the forefront of public attention in advanced and developing countries. At the governmental and international level, an important driver for this change was the announcement by the United Nations (UN) in 2015 of the urgent need for countries to achieve 17 Sustainable Development Goals (SDGs). Energy issues and how we deal with them have now become hot topics that embrace many areas such as “affordable and clean energy (No.7)”, “industry, innovation and infrastructure (No.9)”, “responsible consumption and production (No.12)”. Renewable energy resources, in particular, are attractive given that they can contribute to a decrease in the emissions of greenhouse gases such as CO_2 and NO_x, and this is critical if we are to achieve the goals [1]. Renewable energy resources, however, are less stable in terms of energy output compared to conventional fossil fuel sources such as coal, oil and natural gas because the former depend on the weather and local conditions at the installation site. To stabilize the supply of renewable energy sources, energy storage devices can provide a solution [2,3]. Among the most promising energy storage devices

are rechargeable secondary batteries, which convert electrical energy into chemical energy.

Rechargeable batteries can be used not only to store energy that is intermittent in output, but can also replace fossil fuels as a source of energy for vehicles; alternatively, they can be incorporated into electric vehicles (EVs) and used as a medium for transporting energy in a section of a smart grid system [4]. The acceptance of such technology in EVs has increased rapidly in recent years [5], and has led to a sharp rise in the price of Li since the beginning of 2021. Expectations regarding the widespread uptake of EVs have also led to a spike in the stock prices of companies involved in the development and manufacture of battery materials.

Rechargeable batteries are not only expected to play an important role in addressing the afore-mentioned energy issues but will play an ever-increasing role in portable and advanced electronic devices such as mobile phones, wireless earphones, laptops and drones.

The multiple perspectives that we can identify highlight the strong public interest in battery technology and the paradigm shift that is about to take place in the energy transformation which we have yet to experience.

1.2. Li-ion Batteries (LIBs)

1.2.1. Basics of Li-ion Batteries

A secondary battery is a device that is able to convert chemical energy into electrical energy, and *vice versa*. The oldest primary batteries are thought to have existed over 2000 years ago and are known collectively as the "Baghdad battery". In the modern era, secondary batteries were first conceived as lead-acid batteries by Gaston Planté in France in 1859 [6]. The battery was assembled with a positive electrode made from lead dioxide and a negative electrode made from lead serving as the active materials. The electrodes were made by repeatedly charging and discharging the battery in dilute sulfuric acid, using two pieces of tape rolled into a cylindrical shape sandwiched between two lead plates. Since the late nineteenth century, many types of rechargeable batteries (lead-acid, nickel-cadmium (Ni-Cd), nickel-metal-hydride (Ni-MH), zinc-air, and LIBs) have been developed, and the trends are changing rapidly [7].

Recently, LIBs have become the preferred choice for rechargeable batteries for applications in consumer electronics because they are lightweight, and exhibit a large capacity and a high voltage due to Li being the most electropositive element and having the lowest standard electrode potential, properties which confer a high energy density to LIBs. The use of Li ions as charge carriers in batteries started with Li metal serving as the anode for the above reasons, and the element has now become the primary battery material used for power sources for diverse devices and equipment. Furthermore, it was found by Whittingham et al. that Li ions could be inserted into TiS_2, an inorganic compound, and the Li ions could be reversibly extracted [8,9]. The crystal structures of TiS_2 and $LiTiS_2$ are illustrated in Fig. 1-1, and it is clear that the structure does not change

before and after Li-ion insertion and extraction. Insertion and extraction reactions for ions in a two-dimensional layered structure are called intercalation reactions, because there are no changes in the crystal structure; the materials undergoing such reactions are called intercalation compounds.

To increase battery voltage and improve performance, Mizushima and Goodenough *et al*. developed the $LiCoO_2$ electrode in 1980 [10]. The use of a high-potential $LiCoO_2$ electrode has been the driver for the development of LIBs because materials that exhibit slightly higher potential than Li metal can be used as anode materials. In 1983, Yazami and Touzain reported the reversible electrochemical insertion and extraction (intercalation) of Li ions into graphite at a low potential [11]. This discovery led to the ability to avoid the hazard of short circuits due to dendrite growth on the Li metal anode [12], which previously had been a major problem. To apply $LiCoO_2$ as the cathode and carbonaceous materials as the anode, Yoshino carefully examined the type of nonaqueous electrolyte and its compatibility with the cathode and anode, and then submitted a patent [13]. This battery system is called a rocking chair battery because Li ions move repeatedly between the cathode and anode. In 1991, SONY made further improvements and succeeded in commercializing the first LIB in the world. In 2019, the Nobel Prize in Chemistry was awarded to M. S. Whittingham, J. B. Goodenough and A. Yoshino for their work in the development of LIBs [14].

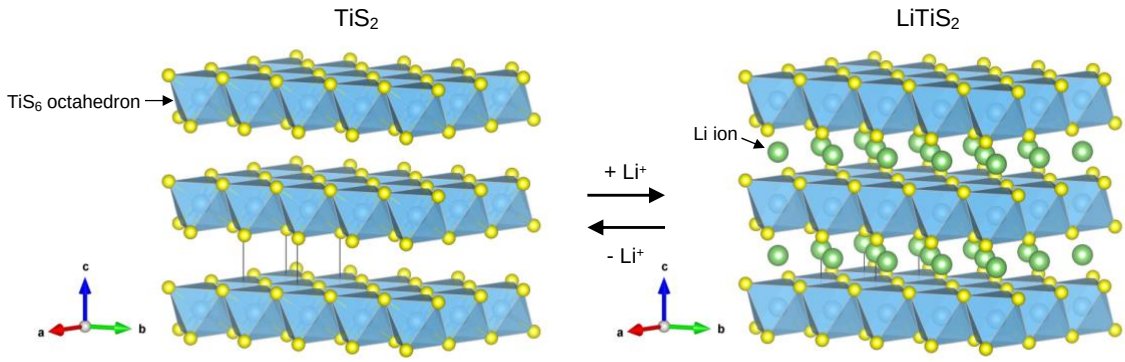

Figure 1-1 Crystal structure of TiS_2 and $LiTiS_2$. Li ions are inserted and extracted between the 2D layers of TiS_2, which functions as an intercalation material (or an insertion material). The crystal structures were downloaded from a materials project [15] and visualized using VESTA [16].

As described above, a LIB consists of three components: a cathode, an anode, and an electrolyte, as shown in Fig. 1-2. In commercially produced LIBs, the cathode and anode are divided by a separator, and the positive and negative electrodes are in contact with the current collector. The cathode is at a higher potential than the anode. The electrolyte does not contribute to the electrode reaction, but only serves to transport the Li ions from one electrode to the other. For a typical LIB based on $LiCoO_2$, the reactions at the cathode and the anode, and the overall reaction are given below.

$$\text{Cathode: } LiCo^{3+}O_2 \rightleftarrows Li_{1-x}Co^{(3+x)+}O_2 + xLi^+ + xe^- \quad (1\text{-}1)$$

$$\text{Anode: } 6C + xLi + xe^- \rightleftarrows Li_xC_6 \quad (1\text{-}2)$$

$$\text{Overall reaction: } LiCo^{3+}O_2 + 6C \rightleftarrows Li_{1-x}Co^{(3+x)+}O_2 + Li_xC_6 \quad (1\text{-}3)$$

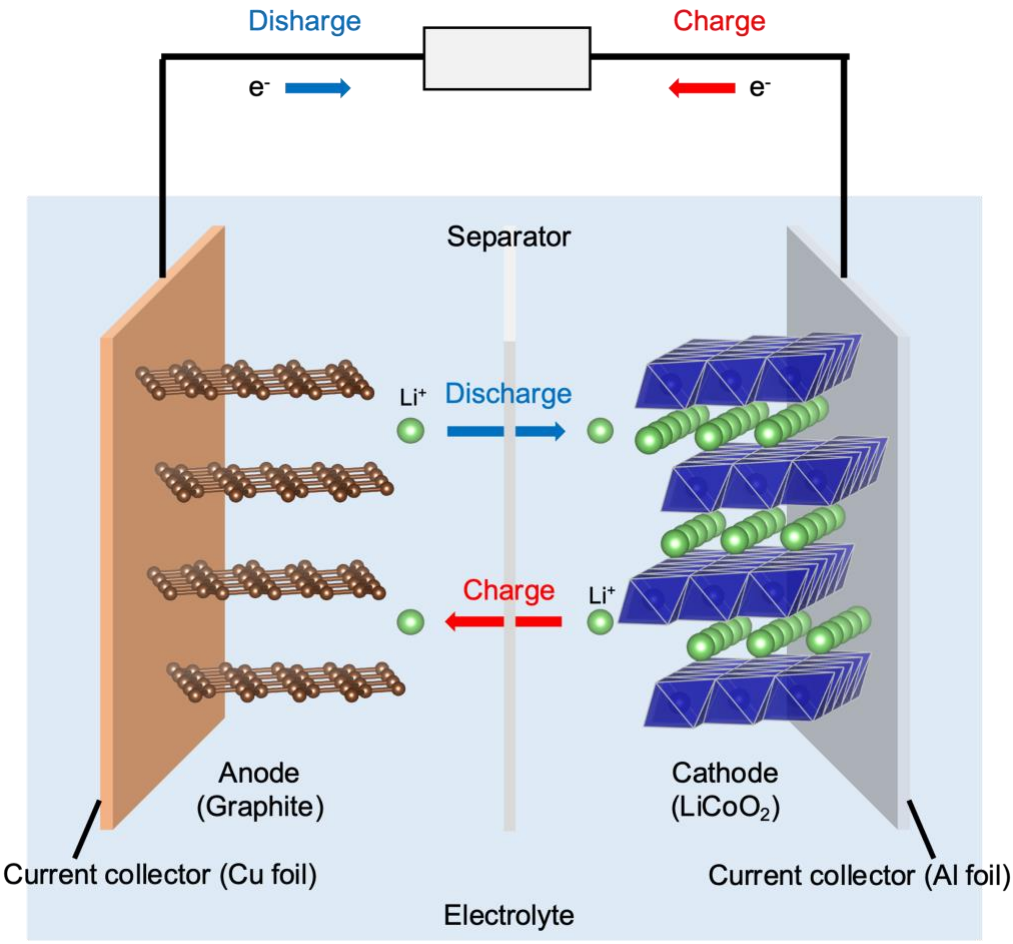

Figure 1-2 Schematic model of typical LIB.

The reaction mechanisms for the electrode materials consist of three main reaction types: an intercalation reaction, a conversion reaction, and an alloying reaction. Among them, the intercalation reaction is superior in terms of cyclability because it inserts and extracts Li ions without major changes in the crystal structure occurring. The conversion reaction suffers problems such as large irreversible capacity and low cyclability because the crystal structure changes significantly during charging and discharging. However, the conversion reaction can be expected to result in an increase in capacity because it can cause a multi-electron reaction. The alloying reaction occurs mainly on the anode side due to the low redox potential, and is caused by alloying of Li

with certain metallic elements. Due to the cyclability and reversibility issues, intercalation materials (or insertion materials) are now the predominant cathode materials.

The theoretical capacity Q and voltage V of the electrode material can be determined by the following formula:

$$Q = \frac{n \times \mathrm{F}}{3600 \times M} \quad (1\text{-}4), \quad V = -\frac{\mu_c - \mu_a}{n\mathrm{F}} \quad (1\text{-}5)$$

where n is the number of electrons in the reaction, F is the Faraday constant, M is the molecular weight of the active material, and μ_c and μ_a represent the chemical potentials of Li^+ in the cathode and anode, respectively.

There are many types of components used in LIBs, and they are listed in Table 1-1. As can be seen, these range from inorganic materials used for electrodes and current collection to organic compounds which serve as solvents in electrolytes and binders. In addition, it is necessary to consider the underlying electrochemistry when electricity is applied, and the electrode reactions that actually occur. It is no exaggeration to say that LIBs involve a "collection of chemistries". Next, aspects of relevant inorganic materials such as the cathode, anode and electrolyte salts are considered.

Table 1-1 List of components in LIBs

Components	Typical materials
Cathode active material	LiMO$_2$ (M: transition metal), LiMnO$_4$, LiFePO$_4$
Anode active material	Graphite, Hard carbon, Li$_4$Ti$_5$O$_{12}$ (LTO)
Binder	PVDF (polyvinylidene difluoride), PTFE (polytetrafluoroethylene)
Electrolyte solvent	EC (ethylene carbonate), PC (propylene carbonate), DMC (dimethyl carbonate), DEC (dimethyl carbonate), or mixtures of the aforementioned solvents
Electrolyte solute	LiPF$_6$, LiBF$_4$, LiClO$_4$
Separator	Microporous polyolefin membrane, PE (polyethylene), PP (polypropylene)

Cathode current collector	Al foil
Anode current collector	Cu foil

1.2.2. Anode Active Materials

Before the LIB was developed, Li metal was used as the anode and there was a risk of short circuiting due to growth of Li dendrites; however, the application of carbonous materials as the anode has dramatically reduced this risk. Currently, graphite is most widely used as an anode, and it has a high capacity and a low potential (~0.1 V vs. Li/Li^+). However, there is still a risk of Li deposition if the graphite is over-lithiated. because the potential is quite close to that for Li metal.

Lithium titanate (Li_2TiO_3; LTO) is also a widely used anode material, but its potential is not as low as that for Li metal or graphite. However, there is no concern regarding the deposition of Li metal because of its relatively high redox potential as an anode active material, and it also has an excellent cycle performance [17].

1.2.3. Cathode Active Materials

The cathode is the electrode with the higher potential of the two electrodes. Therefore, an active material with a high potential and a small electrochemical equivalent is desirable for the cathode. In addition, when the initial chemical composition of the cathode includes carrier ions, an oxidation reaction occurs at the cathode, so it is imperative that gases are not generated by oxidation and gases do not dissolve in the electrolyte after the electrode reaction.

In general, the cathode active material has a layered structure consisting of $LiMO_2$ (M = Co, Mn, Ni, Al, etc.), spinel-type $LiMnO_4$, or $LiFePO_4$, as shown in Table 1-1. $LiMO_2$ is

typically used today, but due to the increasing demand for cathode materials and the rising price of Co, reducing the Co content as much as possible and the use of inexpensive $LiFePO_4$ has become common [18−20]. The working potentials and capacities for $LiMO_2$, $LiMnO_4$, and $LiFePO_4$ are 3.7–4.1 V (vs. Li/Li^+), 3.7–4.0 V, 3.7–3.4 V, and ~150 mAh g^{-1}, ~120 mAh g^{-1}, ~160 mAh g^{-1}, respectively.

1.2.4. Electrolytes

The electrolyte plays an equally important role to that of the cathode and anode because it determines not only the performance of the battery but also its safety. Commercialized LIBs are made by dissolving Li salts in organic solvents (not aqueous solutions) so the electrolytes are called “nonaqueous electrolytes”. Carbonate-based organic solvents such as EC, PC, DMC, and DEC are typically used. These solvents are usually mixed with other solvents to ensure oxidation stability, reduction stability, or to reduce the viscosity of the electrolyte and adequately increase the ionic conductivity. To improve the oxidation or reduction stability, ether-based solvents are used, and attempts are made to change the electrolyte to an ionic liquid in which Li^+ can migrate, even though the ionic conduction is less than that for a commercial electrolyte. The Li salts are mainly $LiPF_6$, $LiClO_4$ and $LiBF_4$. These electrolyte solutes are used mainly in electrode evaluations at a concentration of 1 M which has the highest ionic conductivity; the concentrations of Li salts in commercially available batteries are similar.

1.3. Polyanionic Oxide Materials

1.3.1. Overview of Polyanionic Oxide Materials

Polyanionic compounds have been widely used in cathodes, anodes, and solid electrolytes, and have been studied from various perspectives [21−25]. These compounds can be divided broadly into olivine-type, NASICON-type, tavorite-type, and phosphate fluoride. Alluaudite- and eldfellite-type materials are also being actively researched, although they are used mainly in iron-based materials. The features of polyanionic materials are that they have a large framework of vertex and ridge sharing, which is advantageous for the diffusion of large ions such as Na ions; also, the oxygen-mediated inductive effect of polyanions can tune the redox potential of transition metals [26,27]. However, polyanions have a problem of low volume energy density due to their large volume. Among polyanionic compounds, there are crystal structures in which both Li and Na systems exist, while there are crystal structures in which only one of them exists; this is perhaps due to the existence of an optimal ratio between the size of the crystal framework and the size of the carrier cations. Given that polyanionic materials contain not only MO_6 octahedra consisting of a transition metal as the central element but also XO_4 (X is a hetero-element) tetrahedra consisting of a hetero-element as the central element that does not possess electronic conductivity, the electronic conductivity of the material itself is lower than that of pure oxide-based materials such as layered- and spinel-type materials. Therefore, when incorporating polyanion materials into an electrode, it is common to “add” electronic conductivity by the addition of a carbon-based material. For these reasons, for the development of cathode materials other than the layered oxide materials used in conventional LIBs, focus should be given to polyanionic compounds.

Another advantage of polyanionic compounds is that when applied to all-solid-state batteries (ASSBs), compounds with the same configuration can be used to eliminate the mismatch between the solid electrolyte and the electrode.

1.3.2. Olivine-type Materials

An olivine-based materials can be represented by $AMPO_4$ (*A* is an alkali metal) and the crystal structure is shown in Fig. 1-4, where carrier ions diffuse one-dimensionally in a tunnel [28]. An olivine-iron compound is a cathode material in actual use and is expected to become more popular in the future due to its low cost. It is a promising material with a redox potential of 3.4 V and a theoretical capacity of ~170 mAh g^{-1} [20,29]. The transition metal part of the structure can be substituted with Co due to its high redox potential (4.8 V), but this leads to degradation of the electrolyte [30]. Many examples of partial substitution with other transition metal elements such as Mn and Ti have been reported [31−33].

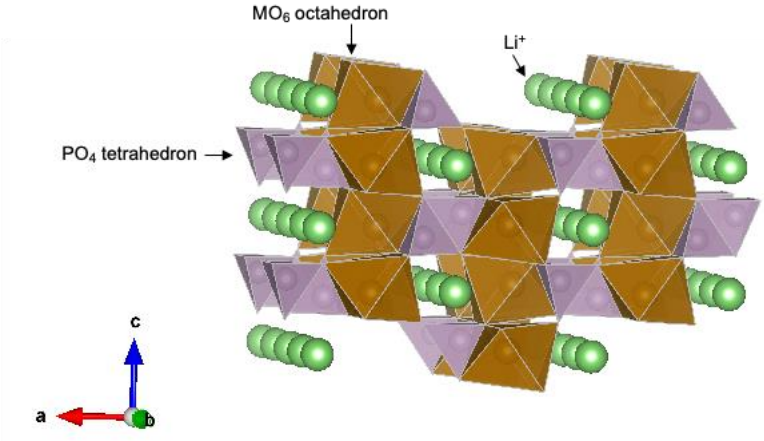

Figure 1-4 Crystal structure of olivine-type material, $LiFePO_4$.

1.3.3. NASICON-type Materials

NASICON (Na Super Ionic CONductor)-type materials are the most studied among the polyanionic materials because of their relative simplicity for synthesis and the possibility of using them not only as cathode materials but also as anode materials and solid electrolytes [34−37]. The crystal structure of NASICON compounds is composed of a MO_6 octahedron and an XO_4 tetrahedron, which are continuously connected by a shared vertex; the structure has a three-dimensional ion carrier path [38]. As a result, the diffusion barrier for carrier ions is small, and large ions such as Na ions can readily diffuse into the structure.

As solid electrolytes, $Na_3Zr_2Si_2PO_{12}$ for Na-based electrolytes [36,39] and $Li_{1+x}Al_xTi_{2-x}(PO_4)_3$ based on $LiTi(PO_4)_3$ for Li-based electrolytes [37,40,41] have been reported as fast ion conductors. High ionic conductivity can be achieved by partial substitution of the transition metal sites in these compounds and the hetero-element sites in the polyanions [42−44].

As an electrode, the redox center can be changed by selecting Ti, V, Cr, Mn, or Fe as the transition metal site [45−52], and the redox potential can be tuned by adjusting the induction effect by changing the hetero element in the polyanion [26,53,54].

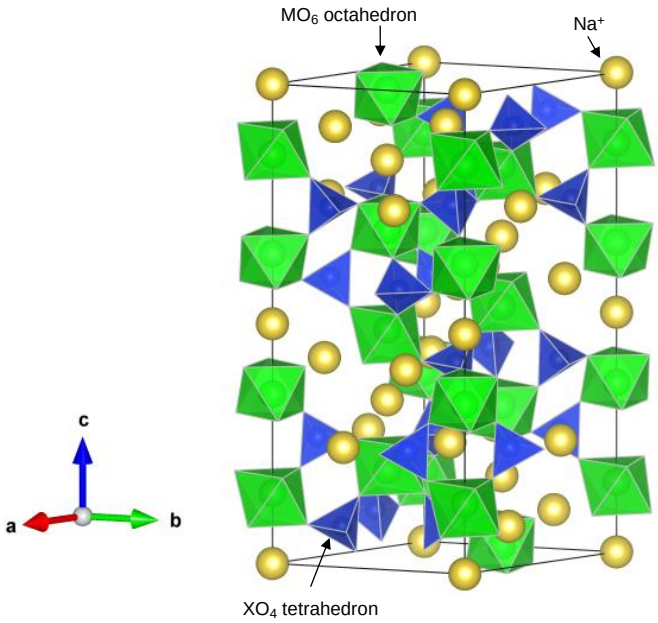

Figure 1-5 Crystal structure of NASICON-type material, $Na_4Zr_2(SiO_4)_3$.

1.3.4. Eldfellite-type Materials

The eldfellite-type material, $NaFe(SO_4)_2$, was discovered relatively recently as a mineral [55]. Its crystal structure is layered with alternating layers of polyanions and layers of Na^+ as shown in Fig. 1-6. Singh *et al.* reported that the charge/discharge properties of $NaFe(SO_4)_2$ are reversible with insertion and extraction of Na^+ [56]. There are some examples of partial substitution of transition metal elements at the Fe sites, but this has not led to improved properties [57,58].

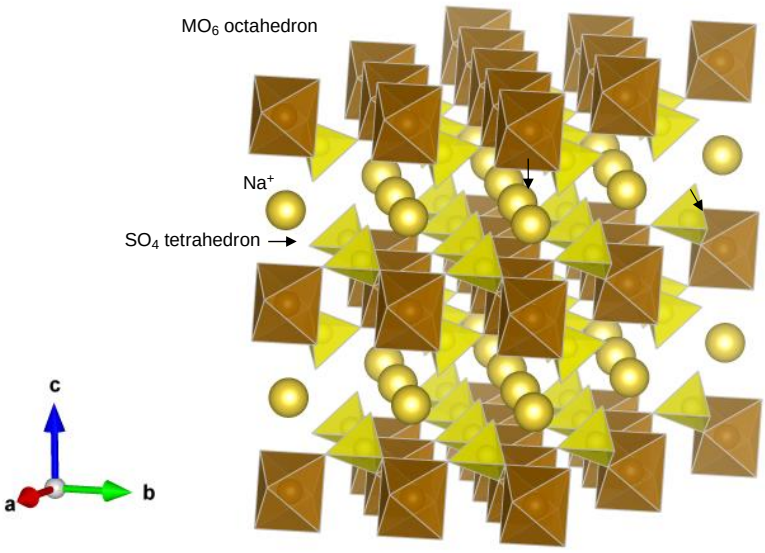

Figure 1-6 Crystal structure of eldfellite-type material, $NaFe(SO_4)_2$.

1.4. All-solid-state Batteries

1.4.1. Overview of all-solid-state Batteries

ASSBs are now one of the hottest topics in energy-related research around the world, and the number of papers and studies on ASSBs and solid electrolytes (SEs) is rapidly increasing [59－61]. Much of the research on ASSBs has focused on the development of SEs [62−66]. The main components of an ASSB are essentially similar to those of a liquid battery, i.e., a cathode, an anode, and a SE. In an ASSB, the SE plays the role of electrolyte and separator, so it is possible to realize a configuration that does not contain any organic compounds. The reason ASSBs are attracting attention as post-LIBs is that they are predicted to surpass conventional batteries in terms of safety, energy density, and power output characteristics. Unless a polymer-type electrolyte is used for the electrolyte in the ASSBs, an inorganic SE is used, so even if a short circuit were to occur, the risk of ignition is low, and the safety of the electrolyte is higher than that of a nonaqueous electrolyte using an organic solvent.

ASSBs can result in a reduction in cell volume by stacking the cathode, anode, SE, and current collector to form a bipolar structure. In the case of liquid batteries, one electrode pair and the electrolyte are sealed in a single cell, and a current collector is attached to both the cathode and anode. If multiple electrodes are placed in one cell, an electromotive force can only be obtained for one pair of electrodes because of the liquid junction. However, in the case of ASSB, there is no carrier ion wrapping around the cell, so even with a bipolar structure in a single cell, the electromotive force for multiple electrodes can be extracted. In addition, the bipolar structure can effectively halve the area of the current collector, which clearly reduces the volume requirements of the cell.

Not only do cations move in a typical liquid electrolyte, but anions also move. Therefore, in the case of non-aqueous electrolytes, the transport number of carrier ions is $t_{Li^+} < 0.4$. However, in the case of SEs, species other than carrier ions do not move because they are part of the crystal structure, and only the carrier ions move, so the transport number is considered to be $t_{Li^+} = 1$. This is a great advantage in terms of ionic transfer and causes the ionic conductivity to be the same for solid and liquid electrolytes. A SE can move practically twice as many carrier ions as a liquid electrolyte because of the difference in transfer number. The ionic conductivity of sulfide SEs has been reported to be superior to that of liquid electrolytes, and there are great expectations in terms of the electrical output characteristics, including a large current flow.

However, ASSBs do suffer from various problems. Sulfide SEs, which exhibit high ionic conductivity as described above, may react with oxygen and moisture in the atmosphere and produce harmful substances such as hydrogen sulfide. Oxide SEs have been widely studied as candidates for SEs, but their ionic conductivity is much lower than that of sulfide SEs, and considerably less than that of current liquid electrolytes. Therefore, exploration of electrolyte materials to improve ionic conductivity is an urgent issue. The junction between the electrode active material and the electrolyte is very important for smooth ion transport. In the case of a liquid electrolyte, the liquid stains the electrode layer so that a smooth contact between the electrode and electrolyte can be obtained, but in the case of a SE, the solid-solid interface makes intimate contact more challenging, and the interfacial resistance between electrodes and electrolytes for ASSBs is higher than those for conventional liquid-type batteries.

In an ASSB, the amount of SE in the electrode phase must also be carefully considered. In the case of liquid batteries, only a small amount of electrolyte is needed because the electrolyte seeps into the electrode phase, but in the case of an ASSB, a

certain amount of SE is needed to ensure the conduction path for carrier ions. Therefore, the amount of electrode active material in the electrode phase is lower, and this may reduce the energy density compared to liquid-type batteries.

In addition to the chemical factors associated with the compound itself, there are also engineering factors that affect the properties of SEs. When the same material is prepared as SE pellets in different laboratories under the same conditions and then subjected to electrical measurements, the results show that the ionic conductivity and activation energy are different for each laboratory [67]. Therefore, various factors that influence the production process need to be studied and controlled for development of high ionic conductivity ASSBs in order to realize a reliable method for production of identical samples.

1.4.2. Solid Electrolytes

A list of Li-ion conducting SE materials is presented in Table 1-2. The mainstream SEs materials, which are sulfide and oxide SEs, are described in detail below.

Table 1-2 Li-ion conducting SE materials

Type	Material	Conductivity / S cm^{-1}	Classification	Reference
(Liquid-type)	(1 M $LiPF_6$ in EC-PC)	~10^{-2}	-	-
Sulfide	Li_6PS_5X (X = Cl, Br)	~10^{-3}	Argyrodite	[68,69]
	$Li_{9.54}Si_{1.74}P_{1.44}S_{11.7}Cl_{0.3}$	2.5 × 10^{-2}	Thio-LISICON (LIthium Super Ionic CONductor)	[70]
	$Li_7P_3S_{11}$	1.7 × 10^{-2}	-	[71,72]
	$Li_{10}GeP_2S_{12}$	1.2 × 10^{-2}	Thio-LISICON	[73,74]
	Li_3PS_4	1.3 × 10^{-3}	Thio-LISICON	[75,76]
	Li_2S-P_2S_5	1.6 × 10^{-4}	Glass	[76,77]
	Li_4SnS_4	7.1 × 10^{-5}	Thio-LISICON	[78]
Oxide	$Li_{0.34}La_{0.56}TiO_3$	1.4 × 10^{-3}	Perovskite	[79]
	$Li_{1+x}Al_xTi_{2-x}(PO_4)_3$	7 × 10^{-4}	NASICON (NAtrium Super Ionic CONductor)	[37,80]
	$Li_7La_3Zr_2O_{12}$	3 × 10^{-4}	Garnet	[81]
	$Li_{2.9}PO_{3.3}N_{0.46}$ (LIPON)	3.3 × 10^{-6}	Amorphous (film)	[82]
Nitride	Li_3N	4 × 10^{-4}	-	[83,84]
Halide	Li_3ScCl_6	3.02 × 10^{-3}	-	[85]
	$Li_{2.5}Y_{0.5}Zr_{0.5}Cl_6$	1.4 × 10^{-3}	-	[86]
	Li_3YCl_6	5.1 × 10^{-4}	-	[87]
Hydride	$LiBH_4$	~10^{-3} (at 120°C)	-	[88]
	$Li_2(BH_4)(NH_2)$	2 × 10^{-4}	-	[89]
	$0.7(LiCB_9H_{10})-0.3(LiCB_{11}H_{12})$	6.7 × 10^{-3}	-	[90]
Hydroxy halide	Li_2OHBr	1.6 × 10^{-6}	Anti-perovskite	[91]
	Li_2OHCl	~10^{-8}	Anti-perovskite	[92]

1.4.2.1. Sulfide Solid Electrolyte

The SE materials showing the highest Li- and Na-ion conductivity reported to date are sulfide SEs [59]. Given that sulfide SEs contain sulfur, an element which has a high polarization, they release Li and Na ions more readily than other anion frameworks, and their ionic conductivity is also higher. This large polarizability also confers additional advantages in terms of a high formability. Given that the Young's modulus for sulfide SEs is very low, and they are soft materials, they can be formed only by cold pressing at room temperature; also, sintered products show quite high ionic conductivity. There are two types of sulfide SEs: amorphous glass types (such as Li_2S-P_2S_5 [76,77] and Li_2S-SiS_2 [93]) and glass-ceramics types (such as Li_3PS_4 [75,76] and $Li_7P_3S_{11}$ [71,77,94]), which are obtained by heating glass SEs. However, the instability of sulfide SE materials causes a difficulty for commercialization due to the generation of H_2S as a result of contact with air. The development of materials to suppress the generation of H_2S has been actively pursued, and it is expected that materials based on Li_4SnS_4 or Li_3SbS_4, in which P is substituted for Sn or Sb, i.e., Li_3PS_4, will be developed [78,95−102]. For Na-ion conductors, a larger framework is needed because the Na-ion radius and volume are larger than those of Li ions. A widely used SE material for Na-ion conduction is the composite material, Na_3PS_4, which is the Na counterpart of Li_3PS_4 in the Li system; this material yields a lower conductivity of 4.6×10^{-4} S cm^{-1} as a result of cold pressing at room temperature [103,104] compared to that for Li_3PS_4. In contrast, the highest ionic conductivity is realized for the Na-ion conductive type material, $Na_{2.88}Sb_{0.88}W_{0.12}S_4$, where the room temperature conductivity for a sintered pellet is 3.2×10^{-2} S cm^{-1} [105]. Of course, the advantage of this material is the enhanced safety due to less H_2S being generated compared to Na_3PS_4 because of the base composition of Na_3SbS_4 [105]. The

highest conductivity is realized by partially substituting Sb with W, leading to the generation of Na-ion vacancies and stabilization of the cubic phase.

1.4.2.2. Oxide Solid Electrolyte

Oxide SEs have the advantage of being stable in air at room temperature, but compared to sulfide SEs, they use O, which has a lower polarization ratio than S. Thus, alkali-ionic diffusion is more difficult than in the case of sulfide SEs. Related to this, the moldability is also lower, and a high relative density and high ionic conductivity cannot be achieved by cold pressing alone [106,107]. Therefore, oxide SEs are typically sintered at high temperature after pelletization. This is not a problem when sintering is performed for a single material, but when it is performed for composite electrode materials or carbonous materials (to provide electronic conductivity), the presence of impurities can be problematic or the samples are reduced to the unwanted [108].

1.4.2.3. Other Solid Electrolytes

Hydride Li-ion conductors have recently become the focus of attention due to their unique properties [109]. $LiBH_4$ undergoes a phase transition at 115°C and shows very high ionic conductivity in the high-temperature phase [88]. Furthermore, by adding 25% LiI, $LiBH_4$ can retain its high-temperature phase even at room temperature, and the material exhibits an impressive ionic conductivity [110]. Combining $(BH_4)^-$ and $(NH_2)^-$ anions, the ionic conductivity is increased to 2×10^{-4} S cm^{-1} for $Li_2(BH_4)(NH_2)$ [89]. The extremely high ionic conductivity (6.7×10^{-3} S cm^{-1}) of the *closo*-type complex hydride

materials, $0.7Li(CB_9H_{10})–0.3Li(CB_{11}H_{12})$, raises high expectations for further development of hydride materials for alkali-ionic conductors [90].

Halide materials are also attracting attention as next-generation SEs due to their high ionic conductivity and oxidation stability. In the 1990s–2000s, halide Li-ion conductors were thought to have been unstable and not highly ion-conductive, but the possibility of ionic mobility has been reevaluated by a research group at Panasonic [87]. The group studied Li_3YCl_6 and Li_3YBr_6 and demonstrated ionic conductivities of 5.1×10^{-4} and 7.2×10^{-4} S cm^{-1} at room temperature. Surprisingly, those SEs showed good coulombic efficiency in charging and discharging with $LiCoO_2$ without any carbonous electronic conductive additive or protective layer coating. The substitution of Y by Zr as in $Li_{2.5}Y_{0.5}Zr_{0.5}Cl_6$ was found to enhance the ionic conductivity up to 1.4×10^{-3} S cm^{-1} at room temperature [86]. In other transition metal systems involving Li_3MCl_6, a higher conductivity has been reported (2.04×10^{-3} S cm^{-1} for *M* = In [111], 3.02×10^{-3} S cm^{-1} for *M* = Sc [85]), and Zr substitution by *M* has been shown to be effective at increasing the ionic conductivity [112,113]. The study of halide alkali ion conductors has only recently been revisited, and the results of theoretical calculations suggest that a variety of candidates can be expected [114−116]; hence, this topic should receive much attention in the near future.

Hydroxy halide systems have been investigated for Li-ion conduction despite the relatively low oxidation or reduction stability. Li_2OHBr has a conductivity of 1.6×10^{-6} S cm^{-1}, and charge and discharge characteristics that are compatible with $Fe_2(MoO_4)_3$ at room temperature [91].

1.4.3. "*in-situ* formed" Electrodes or Electrolytes, and Single-phase All-solid-state Batteries

The resistance at the interface between the SE and the electrode is one of the major problems for practical application of ASSBs. The reason for this is that there is a large difference in the chemical potentials of the SE and electrode materials at the interface, resulting in a space charge layer at the point of contact, and an impedance mismatch. A novel concept to ultimately reduce the interfacial resistance between the electrode and the SE is an "*in-situ* formed" electrode (or electrolyte) that can facilitate the construction of a dense interface. A model scheme for this is depicted in Fig. 1-3. *in-situ* formation relates to forming an electrode (or SE) in the vicinity of the current collector by applying a current through what is originally a SE (or electrode).

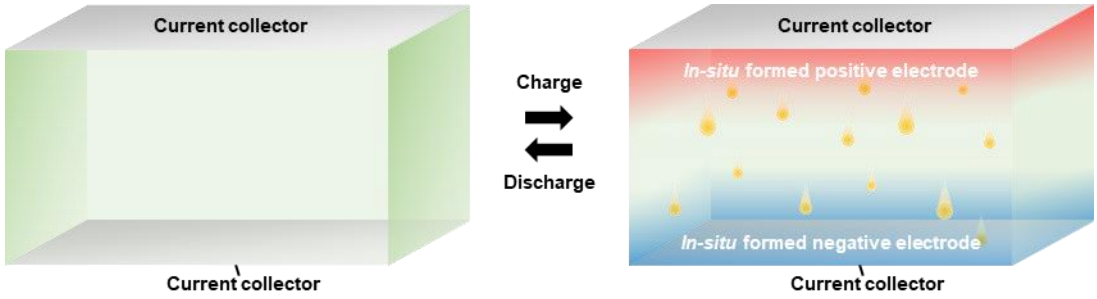

Figure 1-3 Schematic models of single-phase ASSBs.

The original application of the *in-situ* formation concept was its use in a primary Li battery for a pacemaker in 1971, where a composite of iodine and poly-2-vinylpyralidide served as the cathode and Li metal was the anode [117]. When iodine and Li metal contact each other, LiI is formed as an *in-situ* formed SE, and each electrode part can generate power until it is completely consumed. For the first *in-situ* formed

electrode, the Li metal and Li-based compounds are deposited on a Ni substrate using a nonaqueous electrolyte with a three-pole cell [118−120]. In 2000, an *in-situ* formed Li metal anode on a Cu current collector was used as a film-type battery with a $LiCoO_2$ or $Li_xV_2O_5$ cathode (Li source during charging/discharging), $Li_{2.9}PO_{3.3}N_{0.46}$ (LIPON) electrolyte, and an anode current collector attached to the LIPON, so that a reversible capacity was successfully acquired. SEM images indicated the formation of Li metal after 100 cycles. However, the repeated dissolution and plating of Li metal is not safe and many SEs are unstable and are reduced by Li metal, making them unsuitable for SEs other than LIPON; therefore, materials that can be inserted and can extract Li ions are of great interest.

It has been reported that the Li^+ insertion/desorption reaction for the perovskite-type SE $Li_{0.29}La_{0.57}TiO_3$ occurs reversibly in a nonaqueous electrolyte system, but the capacity is very small. Li^+ insertion/desorption into amorphous Li-V-Si-O thin film electrodes has been reported to increase the reversible capacity with each cycle, although the overvoltage is large [121]. Moreover, the depth profile obtained X-ray photoelectron spectroscopy (XPS) after charging shows that the valence of V changes to a higher oxidation number as the distance from the surface increases, suggesting that the electrode reaction occurs near the current collector. A thin-film electrode of Li_2O-Al_2O_3-TiO_2-P_2O_5 (LATP) glass-ceramic functioning as an oxide SE charges and discharges at about 2.2 V vs. Li/Li^+ in a non-aqueous system, and even in a thin-film ASSB with an amorphous Li-Mn-O cathode, the SE acts as an *in-situ* formed negative electrode [122]. A transmission electron microscopy - electron energy loss spectroscopy analysis of an *in-situ* formed electrode from a LATP film indicated that the Li intensity was stronger near the collector, and a Ti chemical shift to a higher oxidation state occurred [123]. *in-situ* formed

electrodes have been examined by optical microscopy, and it was found that Li ions migrated from the vicinity of the current collector and Ti^{4+} was reduced [124].

The principle of the *in-situ* formed electrode is based on the cathode and anode in a single-phase ASSB. In a single-phase ASSB, the electrodes are originally formed from a material with a single composition, so the electrode is called the "positive electrode" for the higher-potential side and the "negative electrode" for the lower-potential side. A battery made from a single material was first reported by Han *et al*. using the sulfide SE, $Li_{10}GeP_2S_{12}$ (LGPS) [125]. This first single-phase ASSB exhibited a large reversible capacity in the first cycle; however, the study involved the use of 25% carbon black to supplement the electronic conductivity (so that the cathode phase, anode phase, and SE phase were actually separated) and used the conversion reaction of LGPS which have a quite low cyclability due to the significant structural changes. The reaction mechanisms determined using density functional theory (DFT) calculations [126] are outlined below.

$$\text{Cathode: } Li_{10}GeP_2S_{12} \rightleftarrows GeS_2 + S + P_2S_5 + 10Li^+ + 10e^- \qquad (1\text{-}6)$$

$$\text{Anode: } Li_{10}GeP_2S_{12} + 10Li^+ + 10e^- \rightleftarrows Li_2S + Li_{15}Ge_4 + Li_3P \qquad (1\text{-}7)$$

To avoid the above problems in a conversion system using a sulfide SE, the current research focus is on insertion materials. Three factors are necessary for insertion materials to be useful in single-phase ASSBs: they should have sufficient ionic conductivity ($\geqq 10^{-6}$ S cm^{-1}; as an electrolyte), the elements can participate in redox reactions in two steps to ensure a potential gap (as positive or negative electrodes), and the elements have the ability to insert and extract carrier ions without major crystal structure changes (for the insertion reaction). Materials that can satisfy these requirements

include NASICON-type materials, $A_xM_2(PO_4)_3$ ($A = Li^+, Na^+, K^+, Ag^+$), which allow 3D diffusion of Li^+ or Na^+. The NASICON-type structure is excellent for both SEs and electrode materials because it has a wide bottleneck with a vertex-sharing framework and there is a large number of choices regarding selection of transition metal elements (the details of NASICON-type materials will be discussed later in the section on "polyanionic oxide materials"). In addition, NASICON-type materials are oxide-based materials with a very high atmospheric stability and are relatively easy to synthesize by a solid-state method. As for the problem of high-temperature sintering with oxide-based materials, the single-phase ASSB consists of a uniform material with a single composition, and there is no concern about side reactions even under high-temperature heat treatment. On this basis, Inoishi *et al.* designed NASICON-type materials to create oxide single-phase ASSBs. They found that $Li_3V_2(PO_4)_3$ and $Na_3V_2(PO_4)_3$ can operate as single-phase ASSBs [127,128]. The electrode reactions for the positive and negative electrodes are as follows (1-8, 1-9):

$$\text{Positive electrode: } A_3V^{3+}{}_2(PO_4)_3 \rightleftarrows A_{(3-x)}V^{(3+x/2)+}{}_2(PO_4)_3 + xA^+ + xe^- \quad (1\text{-}8)$$

$$\text{Negative electrode: } A_3V^{3+}{}_2(PO_4)_3 + xA^+ + xe^- \rightleftarrows A_{(3+x)}V^{(3-x/2)+}{}_2(PO_4)_3 \quad (1\text{-}9)$$

where A is Li or Na. The potential gap between the positive and negative electrodes gives the cell voltage. For the above electrode reactions, a cell voltage of 1.7 V is estimated for the potential gap between the V^{2+}/V^{3+} and V^{3+}/V^{4+} redox reactions for $Li_3V_2(PO_4)_3$ and $Na_3V_2(PO_4)_3$ [52,129,130]. Other materials suitable for functioning as single-phase ASSBs include $Li_{1.5}Cr_{0.5}Ti_{1.5}(PO_4)_3$ and $Ag_{1.5}Cr_{0.5}Ti_{1.5}(PO_4)_3$ as described in Chapter 2 [131,132]. Thus, it is important to select transition metal elements for single-phase ASSB materials that can undergo a redox reaction in two steps, or alternatively that there are

two elements with different redox potentials that can complete the desired reaction. In this thesis, it is reported that the addition of alkali salts is effective for improving the properties of single-phase ASSBs, as detailed in Chapters 3 and 4 [133,134].

1.5. Na-ion Batteries (NIBs)

1.5.1. Challenges and Motivations

There is increasing demand for large-scale batteries for renewable energy storage, and consequently for battery materials and components that are cheap and exhibit excellent performance. In this context, the price of Li for LIBs has risen sharply in 2021 due in particular to the rise in electric vehicle usage. Moreover, in the future, there is likely to be a shortage of materials used in the manufacture of LIBs, and this coupled with an uneven distribution of raw materials among countries, will mean that the commodity prices in mineral producing countries, particularly with regard to Li but also other key components, will be subject to fluctuations in line with global supply and demand.

Given the above situation, NIBs are attractive as rechargeable batteries with excellent cost-benefit performance because they can be prepared from abundant and inexpensive materials [135–139]. However, because the standard electrode potential for Na (-2.71 V vs. standard hydrogen electrode (SHE)) is ~0.3 V higher than that of Li (-3.04 V vs. SHE), the working voltage for a Na-ion battery is lower than that for a Li-ion battery by this amount. In addition, the ionic volume of a Na ion is twice as large as that of a Li ion; hence, a Na-ion battery cathode material would have a relatively wide Na-ion bottleneck and a broad Na-ion diffusion framework structure.

Despite these deficiencies, efforts geared to developing higher performance NIBs have been ongoing for some time. In fact, in recent years, given the increase in practical applications, manufacturers of secondary batteries have expressed their commitment to ongoing development of NIBs. Furthermore, various studies have been

carried out on specific properties of NIBs, which are different from those of LIBs [137,139−143].

1.5.2. Anode Active Materials

Graphite is widely used as an anode material for LIBs, but it is not suitable for NIBs [144]. Hard carbon is a promising candidate as an anode material for NIBs, and its actual capacity is increasing year by year due to active development [145,146]. Polyanion-based materials with low potential are also being developed. Alloy-based anodes that do not depend on the crystal structure are also being actively researched [147], and organic materials that can be adjusted in terms of the width of the framework are also receiving attention [148].

1.5.3. Cathode Active Materials

Given that the standard electrode potential for Na is about 0.3 V higher than that for Li, cathode materials for NIBs are required to have an even higher potential. also, since the ionic volume of Na ions is more than twice as large as that of Li ions, a large framework is appropriate for the crystal structure of cathode materials for NIBs. The most widely studied cathode materials for Na ions are oxide-based materials and polyanionic materials.

Many oxide-based materials that have previously been studied as Li-based cathode materials have been modified for use as Na-based cathode materials. The charge/discharge properties of Li-based and Na-based materials are quite different, reflecting the large differences in ion volume and diffusion barrier [149−151].

To overcome the natural difficulties related to the development of NIBs, polyanionic materials have been intensively investigated as materials that fulfil the two basic requirements, i.e., a high potential and a large framework [22−24,152]. Polyanions, which are strongly electronegative, tend to increase the electrode potential because anions with such high electronegativity can pull electrons from cations, rendering the cations electron-deficient, thereby lowering the Fermi surface and increasing the electrode potential [27,153]. Moreover, the structure around MO_6 octahedra and XO_4 (where *X* is a hetero-element such as B, C, Si, P, S, As, Mo, or W) tetrahedra forms a suitable framework for Na-ion diffusion. Notably, the electronegativity of hetero-elements also affects polyanions and these hetero-elements can tune the redox potential of 3*d* transition metals. For instance, $Li_xFe_2(XO_4)_3$ (*X* = P, S, As, Mo, W), which is a Li-based polyanionic NASICON-type material, exhibited a proportional relationship between the electronegativity of *X* and the redox potential of Fe^{2+}/Fe^{3+} in the materials vs. Li metal [53,154−156]. Among those hetero-elements, S has the highest electronegativity, and thus focus has been given to exploring high-potential cathode materials that contain the sulphate anion (SO_4^{2-}) for use in NIBs as documented in Chapter 5.

1.6. Research Objectives

Given that polyanionic insertion compounds offer a considerable number of options for element selection and material design, there is considerable scope for discovery of innovative materials for next-generation batteries. At the same time, ASSBs have attracted much attention in recent years, but the interfacial resistance between the electrodes and the solid electrolyte, which is much larger than the ionic conductivity of the solid electrolyte, has hindered the commercialization of ASSBs. In this study, polyanionic (especially NASICON-type) materials have been designed to reduce the interfacial resistance on account of the small structural change occurring during charging and discharging, the excellent ionic conductivity, and the wide choice of suitable transition metals. Particular focus has been given to single-phase ASSBs using *in-situ* formed electrodes. To improve the performance of single-phase ASSBs, the effect of addition of an alkali salt, which has only ionic conductivity, was verified.

A key aim of this research on ASSBs is to construct a battery with higher performance than conventional LIBs. Initial work commenced with the development of high-potential cathode materials, the objective being to improve the energy density in NIBs, which are a potential replacement for LIBs. Polyanionic materials can achieve high potentials due to the inductive effect of the polyanions, and hence sulphate materials with the highest induced effect on polyanionic materials were investigated.

Chapter 1 outlines the research background and the introduction of LIBs, NIBs, ASSBs, and polyanion compounds as insertion materials.

The challenges of operating single-phase ASSBs using $Li_{1.5}Cr_{0.5}Ti_{1.5}(PO_4)_3$ are discussed in Chapter 2. $Li_{1.5}Cr_{0.5}Ti_{1.5}(PO_4)_3$ acts as a positive and negative electrode, and

as an electrolyte with the *in-situ* electrode formed from a single compound. It was confirmed that the system functions not only at room temperature but also at sub-zero temperatures. The redox centers of the positive and negative electrodes were identified.

Chapter 3 describes the effect of the addition of Li_3BO_3 into $Li_{1.5}Cr_{0.5}Ti_{1.5}(PO_4)_3$ single-phase ASSBs. Li_3BO_3, which has a low melting point, was added as a flux to fill the grain boundaries to increase the pellet densification and improve the electrochemical and battery performance.

Chapter 4 discusses how the addition of Na_3BO_3 to $Na_3V_2(PO_4)_3$ affects the *in-situ* formed electrodes. The relative densities and electrochemical properties for electrodes prepared with and without addition of Na_3BO_3 are compared and the state of electrode formation near the current collector is examined based on observations by optical microscopy.

The cathode properties of an eldfellite-type insertion material, $NaV(SO_4)_2$, in terms of the electrochemical properties and redox mechanisms during charging/discharging are explored in Chapter 5. $NaV(SO_4)_2$ exhibited a two-step redox reaction and generated a reversible capacity of 102 mAh g^{-1}, which is as large as the theoretical capacity for a one-electron reaction. With respect to charge compensation, it was revealed that there are regions with only a contribution from V and regions with contributions from both V and O based on measurements using synchrotron radiation and on DFT calculations.

The main conclusions of the research are given in Chapter 6.

References

[1] B. Bose, *IEEE Ind. Electron. Mag.* **4** (2010) 6–17.

[2] M.A. Hannan, A.Q. Al-Shetwi, R.A. Begum, P. Jern Ker, S.A. Rahman, M. Mansor, M.S. Mia, K.M. Muttaqi, Z.Y. Dong, *J. Energy Storage*. **42** (2021) 103040.

[3] A.G. Olabi, C. Onumaegbu, T. Wilberforce, M. Ramadan, M.A. Abdelkareem, A.H. Al – Alami, *Energy*. **214** (2021) 118987.

[4] H. Farhangi, *IEEE Power Energy Mag.* **8** (2010) 18–28.

[5] J. Speirs, M. Contestabile, Y. Houari, R. Gross, *Renew. Sustain. Energy Rev.* **35** (2014) 183–193.

[6] P. Kurzweil, *J. Power Sources*. **195** (2010) 4424–4434.

[7] M. Armand, J.-M. Tarascon, *Nature*. **451** (2008) 652–657.

[8] M.S. Whittingham, *J. Electrochem. Soc.* **123** (1976) 315–320.

[9] M.S. Whittingham, *Science* **192** (1976) 1126–1127.

[10] K. Mizushima, P.C. Jones, P.J. Wiseman, J.B. Goodenough, *Mater. Res. Bull.* **15** (1980) 783–789.

[11] R. Yazami, P. Touzain, *J. Power Sources*. **9** (1983) 365–371.

[12] D. Aurbach, Y. Gofer, J. Langzam, *J. Electrochem. Soc.* **136** (1989) 3198–3205.

[13] A. Yoshino, *Angew. Chemie - Int. Ed.* **51** (2012) 5798–5800.

[14] P. V. Kamat, L.F.J. Piper, A. Manthiram, S. Okada, M.S. Islam, Y.S. Meng, X. Li, B.D. McCloskey, Y.K. Sun, L. Nazar, S. Banerjee, *ACS Energy Lett.* **4** (2019) 2763–2769.

[15] A. Jain, S.P. Ong, G. Hautier, W. Chen, W.D. Richards, S. Dacek, S. Cholia, D. Gunter, D. Skinner, G. Ceder, K.A. Persson, *APL Mater.* **1** (2013) 011002.

[16] K. Momma, F. Izumi, *J. Appl. Crystallogr.* **44** (2011) 1272–1276.

[17] T. Ohzuku, A. Ueda, N. Yamamoto, *J. Electrochem. Soc.* **142** (1995) 1431–1435.

[18] E.J. Plichta, W.K. Behl, *J. Power Sources*. **88** (2000) 192–196.

[19] N. Yabuuchi, T. Ohzuku, *J. Power Sources*. **119**–**121** (2003) 171–174.

[20] A.K. Padhi, K.S. Nanjundaswamy, C. Masquelier, S. Okada, J.B. Goodenough, *J. Electrochem. Soc.* **144** (1997) 1609–1613.

[21] Y. Fang, J. Zhang, L. Xiao, X. Ai, Y. Cao, H. Yang, *Adv. Sci.* **4** (2017) 1600392.

[22] C. Masquelier, L. Croguennec, *Chem. Rev.* **113** (2013) 6552–6591.

[23] P. Barpanda, L. Lander, S.I. Nishimura, A. Yamada, *Adv. Energy Mater.* **8** (2018) 1703055.

[24] T. Jin, H. Li, K. Zhu, P.F. Wang, P. Liu, L. Jiao, *Chem. Soc. Rev.* **49** (2020) 2342–2377.

[25] L. Lander, J.M. Tarascon, A. Yamada, *Chem. Rec.* **18** (2018) 1394–1408.

[26] A.K. Padhi, V. Manivannan, J.B. Goodenough, *J. Electrochem. Soc.* **145** (1998) 1518–1520.

[27] B.C. Melot, J.M. Tarascon, *Acc. Chem. Res.* **46** (2013) 1226–1238.

[28] S.-I. Nishimura, G. Kobayashi, K. Ohoyama, R. Kanno, M. Yashima, A. Yamada, *Nat. Mater.* **7** (2008) 707–711.

[29] A.K. Padhi, K.S. Nanjundaswamy, J.B. Goodenough, *J. Electrochem. Soc.* **144** (1997) 1188–1194.

[30] S. Okada, S. Sawa, M. Egashira, J.I. Yamaki, M. Tabuchi, H. Kageyama, T. Konishi, A. Yoshino, *J. Power Sources*. **97**–**98** (2001) 430–432.

[31] R. Gupta, S. Saha, M. Tomar, · V K Sachdev, V. Gupta, *J Mater Sci Mater Electron*. **28** (1234) 5192–5199.

[32] L.T.N. Huynh, P.P.N. Le, V.D. Trinh, H.H. Tran, V.M. Tran, M.L.P. Le, *J. Chem.* **2019** (2019).

[33] S. Kim, V. Mathew, J. Kang, J. Gim, J. Song, J. Jo, J. Kim, *Ceram. Int.* **42** (2016) 7230–7236.

[34] N. Anantharamulu, K. Koteswara Rao, G. Rambabu, B. Vijaya Kumar, V. Radha, M. Vithal, *J. Mater. Sci.* **46** (2011) 2821–2837.

[35] Z. Deng, G. Sai Gautam, S.K. Kolli, J.N. Chotard, A.K. Cheetham, C. Masquelier, P. Canepa, *Chem. Mater.* **32** (2020) 7908–7920.

[36] Y.B. Rao, K.K. Bharathi, L.N. Patro, *Solid State Ionics*. **366**–**367** (2021) 115671.

[37] W. Xiao, J. Wang, L. Fan, J. Zhang, X. Li, *Energy Storage Mater.* **19** (2019) 379–400.

[38] Y. Ishado, A. Inoishi, S. Okada, *Electrochemistry*. **88** (2020) 457–462.

[39] J.B. Goodenough, H.Y.P. Hong, J.A. Kafalas, *Mater. Res. Bull.* **11** (1976) 203–220.

[40] N. Voronina, J.H. Jo, J.U. Choi, A. Konarov, J. Kim, S.T. Myung, *J. Power Sources*. **455** (2020) 227976.

[41] H. Aono, E. Sugimoto, Y. Sadaoka, N. Imanaka, G.-Y. Adachi, *J. Electrochem. Soc.* **137** (1990) 1023–1027.

[42] E. VOGEL, R. CAVA, E. RIETMAN, *Solid State Ionics*. **14** (1984) 1–6.

[43] R.J. Cava, E.M. Vogel, D.W. Johnson, *J. Am. Ceram. Soc.* **65** (1982) c157–c159.

[44] P. Zhang, H. Wang, Q. Si, M. Matsui, Y. Takeda, O. Yamamoto, N. Imanishi, *Solid State Ionics*. **272** (2015) 101–106.

[45] A.K. Padhi, K.S. Nanjundaswamy, C. Masquelier, J.B. Goodenough, *J. Electrochem. Soc.* **144** (1997) 2581–2586.

[46] K. Kawai, W. Zhao, S. Nishimura, A. Yamada, *ACS Appl. Energy Mater.* **1** (2018) 928–931.

[47] K. Kawai, D. Asakura, S. ichi Nishimura, A. Yamada, *Chem. Commun.* **55** (2019) 13717–13720.

[48] J. Wang, Y. Wang, D.H. Seo, T. Shi, S. Chen, Y. Tian, H. Kim, G. Ceder, *Adv. Energy Mater.* **10** (2020) 1903968.

[49] Y. Uebou, T. Kiyabu, S. Okada, J. Yamaki, *Reports Inst. Adv. Mater. Study, Kyushu Univ.* **16** (2002) 1–5.

[50] M. Reichardt, S. Sallard, C. Marino, D. Sheptyakov, P. Novák, C. Villevieille, *J. Energy Storage*. **15** (2018) 266–273.

[51] R. Rajagopalan, B. Chen, Z. Zhang, X.L. Wu, Y. Du, Y. Huang, B. Li, Y. Zong, J. Wang, G.H. Nam, M. Sindoro, S.X. Dou, H.K. Liu, H. Zhang, *Adv. Mater.* **29** (2017) 1605694.

[52] X.H. Rui, N. Yesibolati, C.H. Chen, *J. Power Sources*. **196** (2011) 2279–2282.

[53] S. Okada, H. Arai, J. Yamaki, *Denki Kagaku*. **65** (1997) 802–808.

[54] C. Masquelier, A.K. Padhi, K.S. Nanjundaswamy, J.B. Goodenough, *J. Solid State Chem.* **135** (1998) 228–234.

[55] T. Balić-Žunic, A. Garavelli, P. Acquafredda, E. Leonardsen, S.P. Jakobsson, *Mineral. Mag.* **73** (2009) 51–57.

[56] P. Singh, K. Shiva, H. Celio, J.B. Goodenough, *Energy Environ. Sci.* **8** (2015) 3000–3005.

[57] U. Nisar, M.H. Gulied, R.A. Shakoor, R. Essehli, Z. Ahmad, A. Alashraf, R. Kahraman, S. Al-Qaradawi, A. Soliman, *RSC Adv.* **8** (2018) 32985–32991.

[58] G.C. Ri, S.H. Choe, C.J. Yu, *J. Power Sources*. **378** (2018) 375–382.

[59] O. Sheng, C. Jin, X. Ding, T. Liu, Y. Wan, Y. Liu, J. Nai, Y. Wang, C. Liu, X. Tao, *Adv. Funct. Mater.* **31** (2021) 2100891.

[60] J.C. Bachman, S. Muy, A. Grimaud, H.-H. Chang, N. Pour, S.F. Lux, O. Paschos, F. Maglia, S. Lupart, P. Lamp, L. Giordano, Y. Shao-Horn, *Chem. Rev.* **116** (2016) 140–162.

[61] S. Ohno, A. Banik, G.F. Dewald, M.A. Kraft, T. Krauskopf, N. Minafra, P. Till, M. Weiss, W.G. Zeier, *Prog. Energy*. **2** (2020) 022001.

[62] M. Shoji, E.J. Cheng, T. Kimura, K. Kanamura, *J. Phys. D. Appl. Phys.* **52** (2019) 103001.

[63] Z. Li, P. Liu, K. Zhu, Z. Zhang, Y. Si, Y. Wang, L. Jiao, *Energy & Fuels*. **35** (2021) 9063–9079.

[64] T. Ye, L. Li, Y. Zhang, *Adv. Funct. Mater.* **30** (2020) 1–20.

[65] Z. Ma, H.G. Xue, S.P. Guo, *J. Mater. Sci.* **53** (2018) 3927–3938.

[66] R. Schlem, C.F. Burmeister, P. Michalowski, S. Ohno, G.F. Dewald, A. Kwade, W.G. Zeier, *Adv. Energy Mater.* **11** (2021) 2101022.

[67] S. Ohno, T. Bernges, J. Buchheim, M. Duchardt, A.K. Hatz, M.A. Kraft, H. Kwak, A.L. Santhosha, Z. Liu, N. Minafra, F. Tsuji, A. Sakuda, R. Schlem, S. Xiong, Z. Zhang, P. Adelhelm, H. Chen, A. Hayashi, Y.S. Jung, B. V. Lotsch, B. Roling, N.M. Vargas-Barbosa, W.G. Zeier, *ACS Energy Lett.* **5** (2020) 910–915.

[68] H.J. Deiseroth, S.T. Kong, H. Eckert, J. Vannahme, C. Reiner, T. Zaiß, M. Schlosser, *Angew. Chemie - Int. Ed.* **47** (2008) 755–758.

[69] H.J. Deiseroth, J. Maier, K. Weichert, V. Nickel, S.T. Kong, C. Reiner, *Zeitschrift Fur Anorg. Und Allg. Chemie*. **637** (2011) 1287–1294.

[70] Y. Kato, S. Hori, T. Saito, K. Suzuki, M. Hirayama, A. Mitsui, M. Yonemura, H. Iba, R. Kanno, *Nat. Energy*. **1** (2016) 16030.

[71] Y. Seino, T. Ota, K. Takada, A. Hayashi, M. Tatsumisago, *Energy Environ. Sci.* **7** (2014) 627–631.

[72] H. Yamane, M. Shibata, Y. Shimane, T. Junke, Y. Seino, S. Adams, K. Minami, A. Hayashi, M. Tatsumisago, *Solid State Ionics*. **178** (2007) 1163–1167.

[73] N. Kamaya, K. Homma, Y. Yamakawa, M. Hirayama, R. Kanno, M. Yonemura, T. Kamiyama, Y. Kato, S. Hama, K. Kawamoto, A. Mitsui, *Nat. Mater.* **10** (2011) 682–686.

[74] Y. Sun, K. Suzuki, S. Hori, M. Hirayama, R. Kanno, *Chem. Mater.* **29** (2017) 5858–5864.

[75] M. Murayama, N. Sonoyama, A. Yamada, R. Kanno, *Solid State Ionics*. **170** (2004) 173–180.

[76] A. Hayashi, T. Ohtomo, F. Mizuno, K. Tadanaga, M. Tatsumisago, *Electrochem. Commun.* **5** (2003) 701–705.

[77] F. Mizuno, A. Hayashi, K. Tadanaga, M. Tatsumisago, *Adv. Mater.* **17** (2005) 918–921.

[78] T. Kaib, S. Haddadpour, M. Kapitein, P. Bron, C. Schröder, H. Eckert, B. Roling, S. Dehnen, *Chem. Mater.* **24** (2012) 2211–2219.

[79] S. Stramare, V. Thangadurai, W. Weppner, *Chem. Mater.* **15** (2003) 3974–3990.

[80] H. Aono, E. Sugimoto, Y. Sadaoka, N. Imanaka, G. ya Adachi, *Solid State Ionics*. **40**–**41** (1990) 38–42.

[81] R. Murugan, V. Thangadurai, W. Weppner, [R Murugan, W. Weppner, V. Thangadurai, *Angew. Chemie Int. Ed.* **46** (2007) 7778–7781.

[82] J. Bates, *Solid State Ionics*. **53**–**56** (1992) 647–654.

[83] R.A. Huggins, *Electrochim. Acta*. **22** (1977) 773–781.

[84] J.R. Rea, D.L. Foster, P.R. Mallory, Co. Inc., *Mater. Res. Bull.* **14** (1979) 841–846.

[85] J. Liang, X. Li, S. Wang, K.R. Adair, W. Li, Y. Zhao, C. Wang, Y. Hu, L. Zhang, S. Zhao, S. Lu, H. Huang, R. Li, Y. Mo, X. Sun, *J. Am. Chem. Soc.* **142** (2020) 7012–7022.

[86] K.-H. Park, K. Kaup, A. Assoud, Q. Zhang, X. Wu, L.F. Nazar, *ACS Energy Lett.* **5** (2020) 533–539.

[87] T. Asano, A. Sakai, S. Ouchi, M. Sakaida, A. Miyazaki, S. Hasegawa, *Adv. Mater.* **30** (2018) 1803075.

[88] M. Matsuo, Y. Nakamori, S. Orimo, H. Maekawa, H. Takamura, *Appl. Phys. Lett.* **91** (2007) 224103.

[89] M. Matsuo, A. Remhof, P. Martelli, R. Caputo, M. Ernst, Y. Miura, T. Sato, H. Oguchi, H. Maekawa, H. Takamura, A. Borgschulte, A. Züttel, S.I. Orimo, *J. Am. Chem. Soc.* **131** (2009) 16389–16391.

[90] S. Kim, H. Oguchi, N. Toyama, T. Sato, S. Takagi, T. Otomo, D. Arunkumar, N. Kuwata, J. Kawamura, S. Orimo, *Nat. Commun.* **10** (2019) 1081.

[91] K. Yoshikawa, T. Yamamoto, M.K. Sugumar, M. Motoyama, Y. Iriyama, *Energy & Fuels*. **35** (2021) 12581–12587.

[92] Z.D. Hood, H. Wang, A. Samuthira Pandian, J.K. Keum, C. Liang, *J. Am. Chem. Soc.* **138** (2016) 1768–1771.

[93] N. Machida, K. Kobayashi, Y. Nishikawa, T. Shigematsu, *Solid State Ionics*. **175** (2004) 247–250.

[94] S. Ujiie, A. Hayashi, M. Tatsumisago, *Mater. Renew. Sustain. Energy*. **3** (2014) 18.

[95] G. Sahu, Z. Lin, J. Li, Z. Liu, N. Dudney, C. Liang, *Energy Environ. Sci.* **7** (2014) 1053–1058.

[96] K.H. Park, D.Y. Oh, Y.E. Choi, Y.J. Nam, L. Han, J.Y. Kim, H. Xin, F. Lin, S.M. Oh, Y.S. Jung, *Adv. Mater.* **28** (2016) 1874–1883.

[97] Y.E. Choi, K.H. Park, D.H. Kim, D.Y. Oh, H.R. Kwak, Y.G. Lee, Y.S. Jung, *ChemSusChem*. **10** (2017) 2605–2611.

[98] K. Kanazawa, S. Yubuchi, C. Hotehama, M. Otoyama, S. Shimono, H. Ishibashi, Y. Kubota, A. Sakuda, A. Hayashi, M. Tatsumisago, *Inorg. Chem.* **57** (2018) 9925–9930.

[99] N. Minafra, S.P. Culver, C. Li, A. Senyshyn, W.G. Zeier, *Chem. Mater.* **31** (2019) 3794–3802.

[100] H. Kwak, K.H. Park, D. Han, K.W. Nam, H. Kim, Y.S. Jung, *J. Power Sources*. **446** (2020) 227338.

[101] Z. Zhang, J. Zhang, Y. Sun, H. Jia, L. Peng, Y. Zhang, J. Xie, *J. Energy Chem.* **41** (2020) 171–176.

[102] T. Kimura, A. Kato, C. Hotehama, A. Sakuda, A. Hayashi, M. Tatsumisago, *Solid State Ionics*. **333** (2019) 45–49.

[103] A. Hayashi, K. Noi, A. Sakuda, M. Tatsumisago, *Nat. Commun.* **3** (2012) 2–6.

[104] A. Hayashi, K. Noi, N. Tanibata, M. Nagao, M. Tatsumisago, *J. Power Sources*. **258** (2014) 420–423.

[105] A. Hayashi, N. Masuzawa, S. Yubuchi, F. Tsuji, C. Hotehama, A. Sakuda, M. Tatsumisago, *Nat. Commun.* **10** (2019) 5266.

[106] K. Suzuki, Y. Nakamura, N. Tanibata, A. Hayashi, M. Tatsumisago, *J. Asian Ceram. Soc.* **4** (2016) 6–10.

[107] K. Nagao, M. Nose, A. Kato, A. Sakuda, A. Hayashi, M. Tatsumisago, *Solid State Ionics*. **308** (2017) 68–76.

[108] Y. Noguchi, E. Kobayashi, L.S. Plashnitsa, S. Okada, J.I. Yamaki, *Electrochim. Acta*. **101** (2013) 59–65.

[109] R. Mohtadi, S. Orimo, *Nat. Rev. Mater.* **2** (2017) 16091.

[110] H. Maekawa, M. Matsuo, H. Takamura, M. Ando, Y. Noda, T. Karahashi, S.I. Orimo, *J. Am. Chem. Soc.* **131** (2009) 894–895.

[111] S. Wang, Q. Bai, A.M. Nolan, Y. Liu, S. Gong, Q. Sun, Y. Mo, *Angew. Chemie Int. Ed.* **58** (2019) 8039–8043.

[112] B. Helm, R. Schlem, B. Wankmiller, A. Banik, A. Gautam, J. Ruhl, C. Li, M.R. Hansen, W.G. Zeier, *Chem. Mater.* **33** (2021) 4773–4782.

[113] S.Y. Kim, K. Kaup, K.-H. Park, A. Assoud, L. Zhou, J. Liu, X. Wu, L.F. Nazar, *ACS Mater. Lett.* **3** (2021) 930–938.

[114] K. Kim, D. Park, H.-G. Jung, K.Y. Chung, J.H. Shim, B.C. Wood, S. Yu, *Chem. Mater.* **33** (2021) 3669–3677.

[115] D. Park, H. Park, Y. Lee, S.-O. Kim, H.-G. Jung, K.Y. Chung, J.H. Shim, S. Yu, *ACS Appl. Mater. Interfaces*. **12** (2020) 34806–34814.

[116] Y. Liu, S. Wang, A.M. Nolan, C. Ling, Y. Mo, *Adv. Energy Mater.* **10** (2020) 2002356.

[117] W. Greatbatch, J.H. Lee, W. Mathias, M. Eldridge, J.R. Moser, A.A. Schneider, *IEEE Trans. Biomed. Eng.* **BME-18** (1971) 317–324.

[118] V.R. Koch, J.L. Goldman, C.J. Mattos, M. Mulvaney, *J. Electrochem. Soc.* **129** (1982) 1–4.

[119] T. Osaka, T. Homma, T. Momma, H. Yarimizu, *J. Electroanal. Chem.* **421** (1997) 153–156.

[120] K. Kanamura, S. Shiraishi, Z. Takehara, *J. Electrochem. Soc.* **141** (1994) L108–L110.

[121] C. Yada, Y. Iriyama, T. Abe, K. Kikuchi, Z. Ogumi, *J. Electrochem. Soc.* **153** (2006) A1148.

[122] Y. Iriyama, C. Yada, T. Abe, Z. Ogumi, K. Kikuchi, *Electrochem. Commun.* **8** (2006) 1287–1291.

[123] K. Yamamoto, R. Yoshida, T. Sato, H. Matsumoto, H. Kurobe, T. Hamanaka, T. Kato, Y. Iriyama, T. Hirayama, *J. Power Sources*. **266** (2014) 414–421.

[124] T. Yamamoto, Y. Sugiura, H. Iwasaki, M. Motoyama, Y. Iriyama, *Solid State Ionics*. **337** (2019) 19–23.

[125] F. Han, T. Gao, Y. Zhu, K.J. Gaskell, C. Wang, *Adv. Mater.* **27** (2015) 3473–3483.

[126] F. Han, Y. Zhu, X. He, Y. Mo, C. Wang, *Adv. Energy Mater.* **6** (2016) 1501590.

[127] A. Inoishi, T. Omuta, E. Kobayashi, A. Kitajou, S. Okada, *Adv. Mater. Interfaces*. **4** (2017) 3–7.

[128] A. Inoishi, T. Omuta, Y. Yoshioka, E. Kobayashi, A. Kitajou, S. Okada, *ChemistrySelect.* **2** (2017) 7925–7929.

[129] T. Akçay, M. Häringer, K. Pfeifer, J. Anhalt, J.R. Binder, S. Dsoke, D. Kramer, R. Mönig, *ACS Appl. Energy Mater.* **4** (2021) 12688–12695.

[130] E. Kobayashi, A. Kitajou, S. Okada, J.I. Yamaki, *J. Power Sources*. **244** (2013) 312–317.

[131] A. Inoishi, A. Nishio, Y. Yoshioka, A. Kitajou, S. Okada, *Chem. Commun.* **54** (2018) 3178–3181.

[132] A. Inoishi, A. Nishio, A. Kitajou, S. Okada, *ChemistrySelect*. **3** (2018) 9965–9968.

[133] A. Nishio, A. Inoishi, A. Kitajou, S. Okada, *J. Ceram. Soc. Japan*. **127** (2019) 18–21.

[134] A. Nishio, N. Shirai, H. Minami, H. Izumi, A. Inoishi, S. Okada, *Electrochemistry*. **89** (2021) 244–249.

[135] V. Palomares, P. Serras, I. Villaluenga, K.B. Hueso, J. Carretero-González, T. Rojo, *Energy Environ. Sci.* **5** (2012) 5884.

[136] K. Kubota, S. Komaba, *J. Electrochem. Soc.* **162** (2015) A2538–A2550.

[137] J.Y. Hwang, S.T. Myung, Y.K. Sun, *Chem. Soc. Rev.* **46** (2017) 3529–3614.

[138] C. Vaalma, D. Buchholz, M. Weil, S. Passerini, *Nat. Rev. Mater.* **3** (2018) 18013.

[139] K. Chayambuka, G. Mulder, D.L. Danilov, P.H.L. Notten, *Adv. Energy Mater.* **8** (2018) 1800079.

[140] S. Daugela, (2019) 154.

[141] Y. You, A. Manthiram, *Adv. Energy Mater.* **8** (2018) 1–11.

[142] G. Zhu, X. Tian, H.-C. Tai, Y.-Y. Li, J. Li, H. Sun, P. Liang, M. Angell, C.-L. Huang, C.-S. Ku, W.-H. Hung, S.-K. Jiang, Y. Meng, H. Chen, M.-C. Lin, B.-J. Hwang, H. Dai, *Nature*. **596** (2021) 525–530.

[143] C. Delmas, *Adv. Energy Mater.* **8** (2018) 1703137.

[144] P. Ge, M. Fouletier, *Solid State Ionics*. **28**–**30** (1988) 1172–1175.

[145] D.A. Stevens, J.R. Dahn, *J. Electrochem. Soc.* **147** (2000) 1271.

[146] M. Dahbi, N. Yabuuchi, K. Kubota, K. Tokiwa, S. Komaba, *Phys. Chem. Chem. Phys.* **16** (2014) 15007–15028.

[147] K. Song, C. Liu, L. Mi, S. Chou, W. Chen, C. Shen, *Small*. **17** (2021).

[148] A. V. Desai, R.E. Morris, A.R. Armstrong, *ChemSusChem*. **13** (2020) 4866–4884.

[149] N. Yabuuchi, M. Kajiyama, J. Iwatate, H. Nishikawa, S. Hitomi, R. Okuyama, R. Usui, Y. Yamada, S. Komaba, *Nat. Mater.* **11** (2012) 512–517.

[150] Y. Tsuchiya, A.M. Glushenkov, N. Yabuuchi, *ACS Appl. Nano Mater.* **1** (2018) 364–370.

[151] S. Komaba, C. Takei, T. Nakayama, A. Ogata, N. Yabuuchi, *Electrochem. Commun.* **12** (2010) 355–358.

[152] S.K. Sapra, J. Pati, P.K. Dwivedi, S. Basu, J. Chang, R.S. Dhaka, *WIREs Energy Environ.* **10** (2021) 37.

[153] J.B. Goodenough, Y. Kim, *Chem. Mater.* **22** (2010) 587–603.

[154] A. Manthiram, J.B. Goodenough, *J. Solid State Chem.* **71** (1987) 349–360.

[155] A. Manthiram, J.B. Goodenough, *J. Power Sources*. **26** (1989) 403–408.

[156] K.S. Nanjundaswamy, A.K. Padhi, J.B. Goodenough, S. Okada, H. Ohtsuka, H. Arai, J. Yamaki, *Solid State Ionics*. **92** (1996) 1–10.

Chapter 2

A single-phase all-solid-state lithium battery based on $Li_{1.5}Cr_{0.5}Ti_{1.5}(PO_4)_3$ for high-rate capability and low temperature operation

2.1. Introduction

All-solid-state LIBs provide a solution to challenges associated with traditional LIBs, such as safety concerns and low energy densities. Many solid electrolytes have been investigated for this purpose, including LISICON [1], thio-LISICON [2], NASICON [3,4], perovskites [5], garnets [6], lithium borohydride [7] and sulfide-based materials [8]. Sulfide-based electrolytes offer the advantages of high ionic conductivity and good contact between the electrolyte and electrode following cold pressing at room temperature [8]. Cold pressing also avoids side reactions between the electrolyte and electrode because it does not require high-temperature calcination to connect the two materials. This reduces the interfacial resistance between the electrolyte and electrode and improves the performance of the battery [8–11]. Because sulfide-based electrolytes tend to generate gaseous H_2S, oxide-based lithium-ion conducting solid electrolytes are considered to be safer. However, oxide-based ASSBs tend to exhibit a high interfacial

resistance between the electrolyte and electrode as a result of side reactions during the high-temperature sintering required for good contact between the electrolyte and electrode. This resistance in turn limits the rate capability of the battery, even if the conductivity of the oxide-based solid electrolyte is high. A battery made from a single material would therefore be ideal, because there would be no chance of side reactions during fabrication. Han *et al*. demonstrated the concept of a single-material battery using $Li_{10}GeP_2S_{12}$ as the electrolyte, anode and cathode to eliminate interfacial resistance between the electrode and electrolyte [12]. Recently, Inoishi *et al.* reported all-solid-state cells composed of a single material, using either $Na_{3-x}V_{2-x}Zr_x(PO_4)_3$ [13] or $Li_3V_{2-x}Al_x(PO_4)_3$ [14], which they term "single-phase ASSBs." In these new batteries, a single material functions as the anode, cathode and electrolyte. These NASICON (Na Super Ionic CONductor)- type materials have demonstrated high (lithium or sodium) ionic conductivity and undergo redox reactions based on the V^{3+}/V^{2+} (negative electrode) and V^{3+}/V^{4+} (positive electrode) pairs [15–18]. One of the most important advantages of a so-called single-phase battery is low inter- facial resistance stemming from an ideal interface between the electrolyte and electrode. Therefore, a single-phase battery is a promising new concept that could allow high-rate, all-solid-state oxide-based batteries. However, the electrical conductivities of $Na_{2.6}V_{1.6}Zr_{0.4}(PO_4)_3$ and $Li_3V_{1.6}Al_{0.4}(PO_4)_3$ at room temperature are 5 x 10^{-6} S cm^{-1} and 6 x 10^{-6} S cm^{-1}, respectively [13,14]. These values are much lower than those for typical lithium-ionic conductors such as a NASICON-type ionic conductor [4] or a garnet-type ionic conductor [7]. Therefore, to decrease the large IR drop, superior lithium ionic-conducting materials must be applied to the fabrication of single-phase ASSBs. It is well known that $LiTi_2(PO_4)_3$-based NASICON-type compounds exhibit significant lithium-ionic conductivity at room temperature, and so they may be the best choice for a single- phase battery. Iriyama *et al.* reported that a

$LiTi_2(PO_4)_3$ solid electrolyte can be used as both the electrolyte and anode, based on the Ti^{4+}/Ti^{3+} redox pair [19]. Therefore, if this material can also function as the cathode, single-phase $LiTi_2(PO_4)_3$-based cells could be possible. It has also been reported that Cr-doped $LiTi_2(PO_4)_3$ ($Li_{1.5}Cr_{0.5}Ti_{1.5}(PO_4)_3$) shows an elevated ionic conductivity of more than 10 x 4 S cm^{-1} [4,20]. In addition, $Li_3Cr_2(PO_4)_3$ acting as a cathode material has produced a high voltage plateau based on the Cr^{3+}/Cr^{4+} redox pair [21]. Therefore, Cr-doped $LiTi_2(PO_4)_3$ is one of the best candidates for use in single-phase batteries with high ionic conductivity, simultaneously functioning as the anode and cathode. Herein, I report a single- phase all-solid-state lithium-ion battery using the NASICON-type compound $Li_{1.5}Cr_{0.5}Ti_{1.5}(PO_4)_3$ as the cathode, anode and electrolyte. A diagram showing the experimental single-phase lithium-ion battery based on $Li_{1.5}Cr_{0.5}Ti_{1.5}(PO_4)_3$ is presented in Fig. 2-1. During charging, the following reactions are assumed to have occurred (2-1, 2-2):

(Cathode, Cr^{3+}/Cr^{4+}) $Li_{1.5}Cr_{0.5}Ti_{1.5}(PO_4)_3 \rightarrow LiCr_{0.5}Ti_{1.5}(PO_4)_3 + 0.5Li^+ + 0.5e^-$ (2-1)

(Anode, Ti^{4+}/Ti^{3+}) $Li_{1.5}Cr_{0.5}Ti_{1.5}(PO_4)_3 + 1.5Li^+ + 1.5e^- \rightarrow Li_3Cr_{0.5}Ti_{1.5}(PO_4)_3$ (2-2)

From the values reported previously, the cathode and anode potentials are assumed to be 4.8 V[21] and 2.5 V [22,23], respectively.

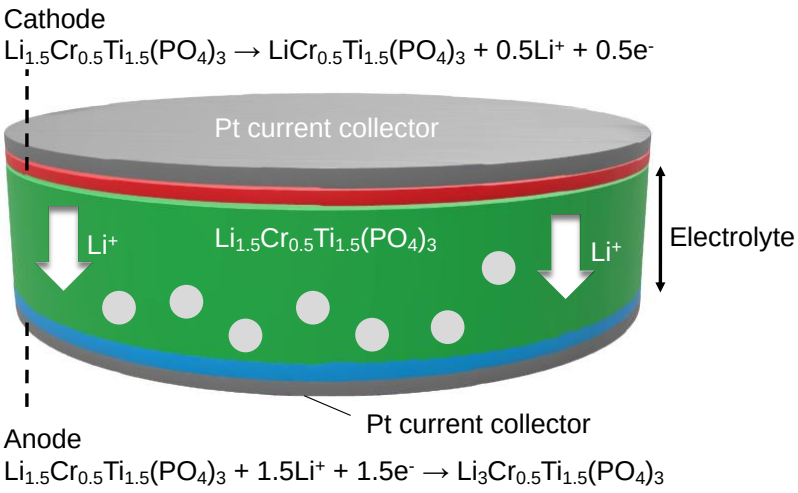

Figure 2-1 Schematic of a Pt/$Li_{1.5}Cr_{0.5}Ti_{1.5}(PO_4)_3$/Pt cell studied in this work as a single-phase, all-solid-state lithium-ion battery (shown during charging).

2.2. Experimental

2.2.1. Materials Synthesis and Pelletization

$Li_{1.5}Cr_{0.5}Ti_{1.5}(PO_4)_3$ was prepared by the conventional solid- state reaction method. Li_2CO_3, Cr_2O_3, TiO_2 and $NH_4H_2PO_4$ were mixed in stoichiometric amounts and calcined at 573 K for 2 h in air. The product was subsequently ground and calcined at 1273 K for 5 h in air. The resulting powder was again ground and then ball-milled at 200 rpm for 2 h, followed by pelletization and annealing at 1373 K in air for 5 h.

2.2.2. Electrochemical Characterization

A thin platinum layer was applied to both sides of the resulting pellet (B9mm in diameter, 0.6 mm in thickness) via sputtering. This single- phase all-solid-state cell was subsequently sealed into an HS cell (Hohsen Corp.), working in an Ar-filled glove box. Charge–discharge tests were terminated based on a charging capacity of 10 mA h while the discharge termination voltage was set at 10 mV. Electrochemical half-cell tests were performed using a typical electrochemical cell in conjunction with an organic electrolyte (1 M $LiPF_6$/EC-DMC), a Li metal anode and mixtures composed of 75% by mass of the active material and 25% by mass of acetylene black. PTFE was added at an additional 5% by mass (based on the total active material/acetylene black mass) as a binder to assist in fabricating electrode pellets. Pressed pellets (approximately 10 mm in diameter, 20 mg in mass) were produced from these mixtures. The test cell was fabricated using a 2032 coin-type cell in conjunction with the organic electrolyte and a polypropylene separator (Celgard 3501, Celgard) with lithium metal.

2.3. Results and Discussion

2.3.1. Materials Observation

Figure 2-2 shows X-ray diffraction (XRD) patterns for $Li_{1.5}Cr_{0.5}Ti_{1.5}(PO_4)_3$ sintered at 1373 K. These data confirm that the samples show a NASICON-type phase without any impurities, in agreement with prior research [4]. Fig. 2-3 shows a scanning electron microscopy (SEM) image of the $Li_{1.5}Cr_{0.5}Ti_{1.5}(PO_4)_3$ pellet in which pores can be seen. The result of the Energy Dispersive X-ray Spectrometry (EDS) showed that the ratio of Cr to Ti in the $Li_{1.5}Cr_{0.5}Ti_{1.5}(PO_4)_3$ was 1.0:3.0. It was in good agreement with the target composition. The porosity of this specimen, as determined using Archimedes' principle, was 83%, which is not overly high compared to values for typical NASICON-type lithium-ionic conductors [4].

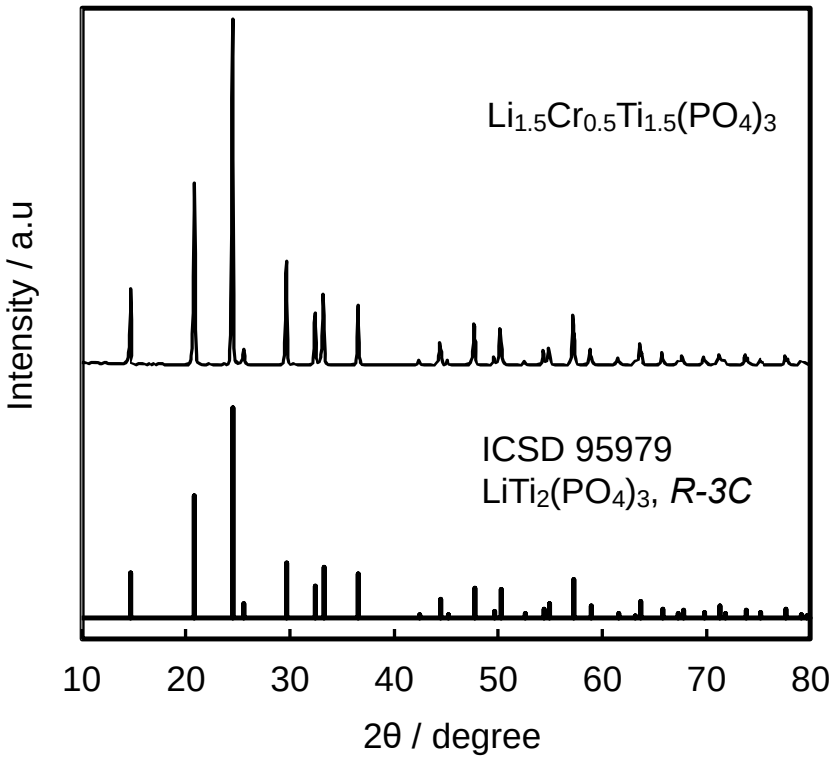

Figure 2-2 XRD pattern for as-prepared $Li_{1.5}Cr_{0.5}Ti_{1.5}(PO_4)_3$.

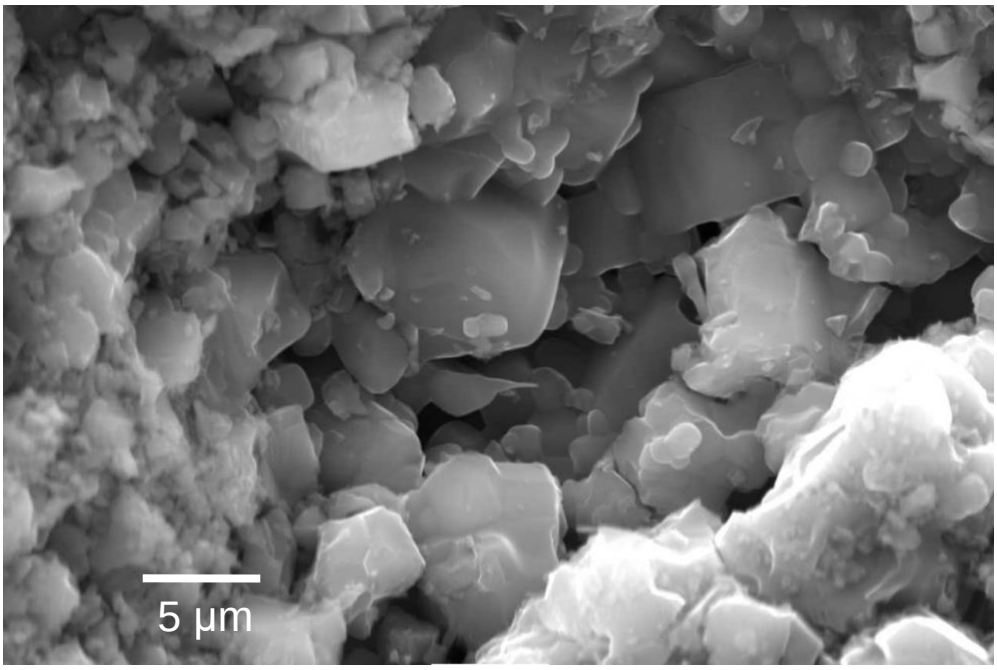

Figure 2-3 SEM image of surface of $Li_{1.5}Cr_{0.5}Ti_{1.5}(PO_4)_3$ pellet.

2.3.2. Electrochemical Properties

Figure 2-4 presents an impedance plot for the Pt/ $Li_{1.5}Cr_{0.5}Ti_{1.5}(PO_4)_3$/Pt cell at 298 K. The inset to this figure provides the entire plot between 1 MHz and 0.1 Hz. These data conform to the typical impedance spectrum of a solid electrolyte attached to a blocking electrode. A semicircle associated with grain boundaries is evident between 1 MHz and 10 kHz, while below 10 kHz capacitance resulting from ion-blocking electrodes is observed. These results indicate that the interface between the Pt and the test material represents a blocking electrode under open-circuit conditions without any applied potential. Fig. 2-4b plots the electrical conductivity of the $Li_{1.5}Cr_{0.5}Ti_{1.5}(PO_4)_3$ sintered at 1373 K in air. The conductivity at 298 K of 2×10^{-4} S cm^{-1} is in good agreement with a previously reported value [4]. At a relatively low temperature of 233 K, it still exhibited a conductivity of 1×10^{-5} S cm^{-1}. The activation energy below 273 K was 0.29 eV, which is comparable with that reported previously for a typical high-performance lithium-ionic

conductor [7,10]. Fig. 2-5a presents the charge–discharge profile acquired from a half cell using the $Li_{1.5}Cr_{0.5}Ti_{1.5}(PO_4)_3$ electrode in conjunction with a Li metal anode in an organic liquid electrolyte. As a result of lithium extraction, a high-voltage plateau appears at approximately 4.8 V based on the Cr^{3+}/Cr^{4+} redox couple, in good agreement with the redox potential of the Cr^{3+}/Cr^{4+} couple in $Li_3Cr_2(PO_4)_3$ [21]. The initial Cr^{3+}/Cr^{4+} charge capacity is close to that expected for a 0.5 electron reaction, and thus in concordance with the theoretical capacity of the $Li_{1.5}Cr_{0.5}Ti_{1.5}(PO_4)_3$ cathode. In contrast, lithium insertion into the $Li_{1.5}Cr_{0.5}Ti_{1.5}(PO_4)_3$ produces a plateau at approximately 2.5 V based on the Ti^{4+}/Ti^{3+} redox couple. This is also in agreement with the redox potential of the Ti^{4+}/Ti^{3+} couple in $LiTi_2(PO_4)_3$ [22,23]. The initial Ti^{4+}/Ti^{3+} charge capacity is almost equivalent to that for a 1.5 electron reaction, as expected based on the theoretical capacity of the $Li_{1.5}Cr_{0.5}Ti_{1.5}(PO_4)_3$ anode. From these results, I can assume that the ‘‘full-cell’’ voltage is 2.2 V when $Li_{1.5}Cr_{0.5}Ti_{1.5}(PO_4)_3$ is used as both cathode and anode. Fig. 2-5b and 2-5c show the room temperature charge–discharge profiles for a full cell composed of a single-phase all-solid-state type cell and a liquid electrolyte-type cell, respectively. Both the single-phase and liquid-type cells generated an operational voltage of 2.2 V, demonstrating reasonable performance from the single-phase battery using $Li_{1.5}Cr_{0.5}Ti_{1.5}(PO_4)_3$. Surprisingly, the current density obtained from the single-phase cell was 0.1 mA cm^{-2} even though a very thick electrolyte (B600 mm) was used. This high-rate capability is attributed to the increased ionic conductivity and low interfacial resistance of the single-phase cell design. However, the coulombic efficiency of the battery is about 40%. One of the reasons of the low coulombic efficiency might be caused by the electron leakage in the $Li_{1.5}Cr_{0.5}Ti_{1.5}(PO_4)_3$. The rough estimation of the thickness of the ‘‘*in-situ* formed cathode/anode’’ from the capacity was B600 nm. The estimated thickness is almost the same as the reported value of the ‘‘*in-situ* formed anode’’ in the

$LiTi_2(PO_4)_3$-based NASICON-type solid electrolyte. Therefore, the capacity of the full-cell might be limited by the anode. Figures 2-6a, 2-6b, and 2-6c show the first charge–discharge curves of the Pt/ $Li_{1.5}Cr_{0.5}Ti_{1.5}(PO_4)_3$/Pt cell with different current densities at 298 K. The highest capacity was obtained with a current density of 0.1 mA cm^{-2} (Fig. 2-5b). Cycling properties with different current densities are shown in Fig. 2-6d. The most stable cycling was performed when the current density was 0.1 mA cm^{-2}. Figure 2-5d shows the charge–discharge profile for the single-phase all-solid-state cell using $Li_{1.5}Cr_{0.5}Ti_{1.5}(PO_4)_3$ at 233 K. Although the current density was decreased to 1.5 μA cm^{-2} because of the decreased electrical conductivity, a reasonable charge–discharge profile was obtained. The inset provides the charge–discharge profile for the full cell using the liquid electrolyte at 233 K. This cell was evidently not operational, although the conductivity of the liquid electrolyte was much higher than that of the $Li_{1.5}Cr_{0.5}Ti_{1.5}(PO_4)_3$ at 233 K [24]. This result can possibly be attributed to the significant resistance of the highly viscous liquid electrolyte.

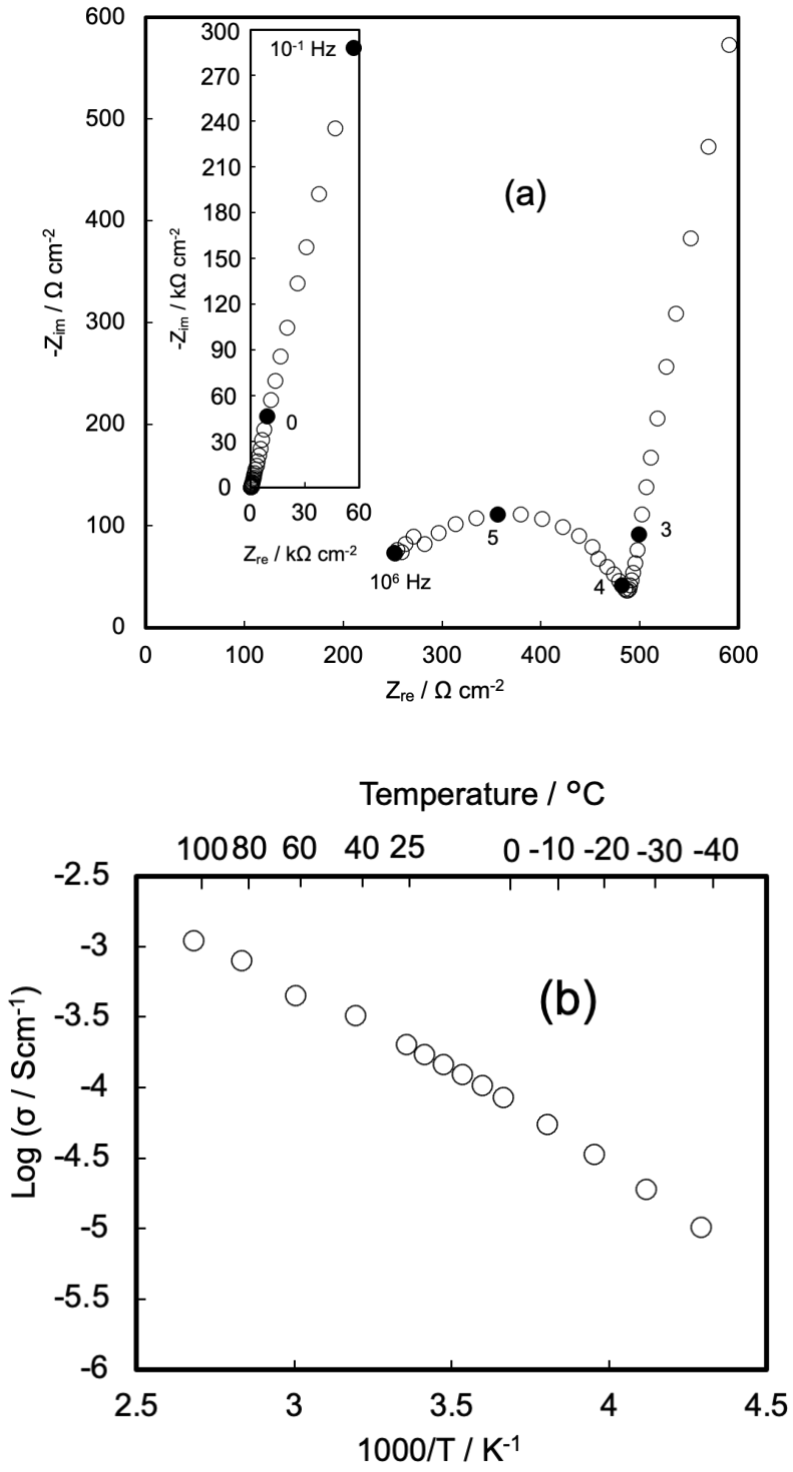

Figure 2-4 (a) Impedance plot for a Pt/ $Li_{1.5}Cr_{0.5}Ti_{1.5}(PO_4)_3$/Pt device at 298 K (inset: entire frequency ranges from 1 MHz to 0.1 Hz) and (b) electrical conductivity of $Li_{1.5}Cr_{0.5}Ti_{1.5}(PO_4)_3$ sintered at 1373 K in air.

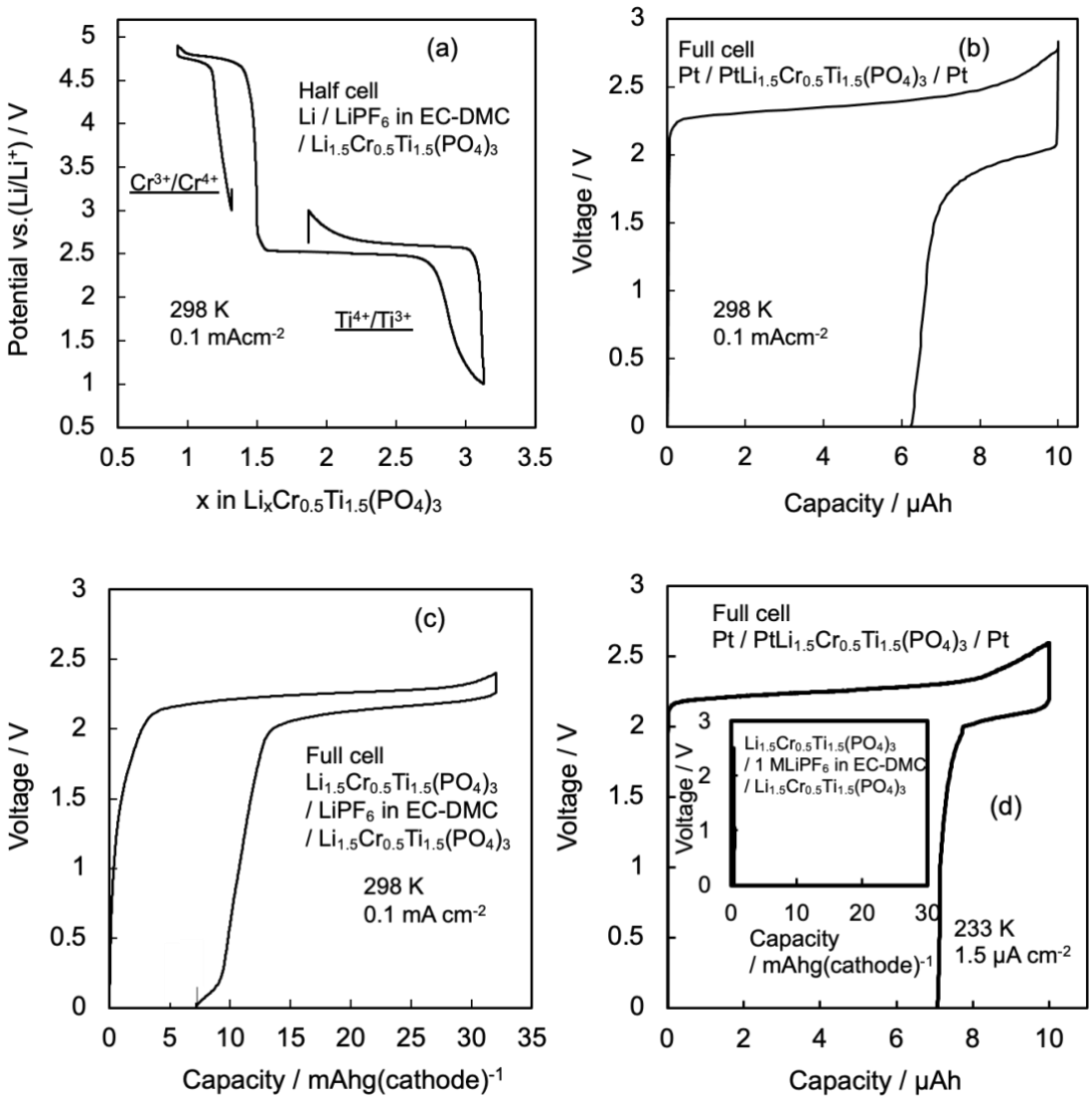

Figure 2-5 (a) Charge–discharge profiles for a half cell using a $Li_{1.5}Cr_{0.5}Ti_{1.5}(PO_4)_3$ electrode and a Li metal anode in an organic liquid electrolyte, (b) charge– discharge profiles for a single-phase all-solid-state cell with a Pt/ $Li_{1.5}Cr_{0.5}Ti_{1.5}(PO_4)_3$/Pt structure at 298 K and (c) charge–discharge profiles for a liquid-type "full cell" using a $Li_{1.5}Cr_{0.5}Ti_{1.5}(PO_4)_3$ electrode at 298 K. (d) Charge–discharge profile of a single-phase all-solid-state cell with a Pt/ $Li_{1.5}Cr_{0.5}Ti_{1.5}(PO_4)_3$/Pt structure at 233 K (inset: charge–discharge profile for a liquid-type "full cell" using a $Li_{1.5}Cr_{0.5}Ti_{1.5}(PO_4)_3$ electrode at 233 K)

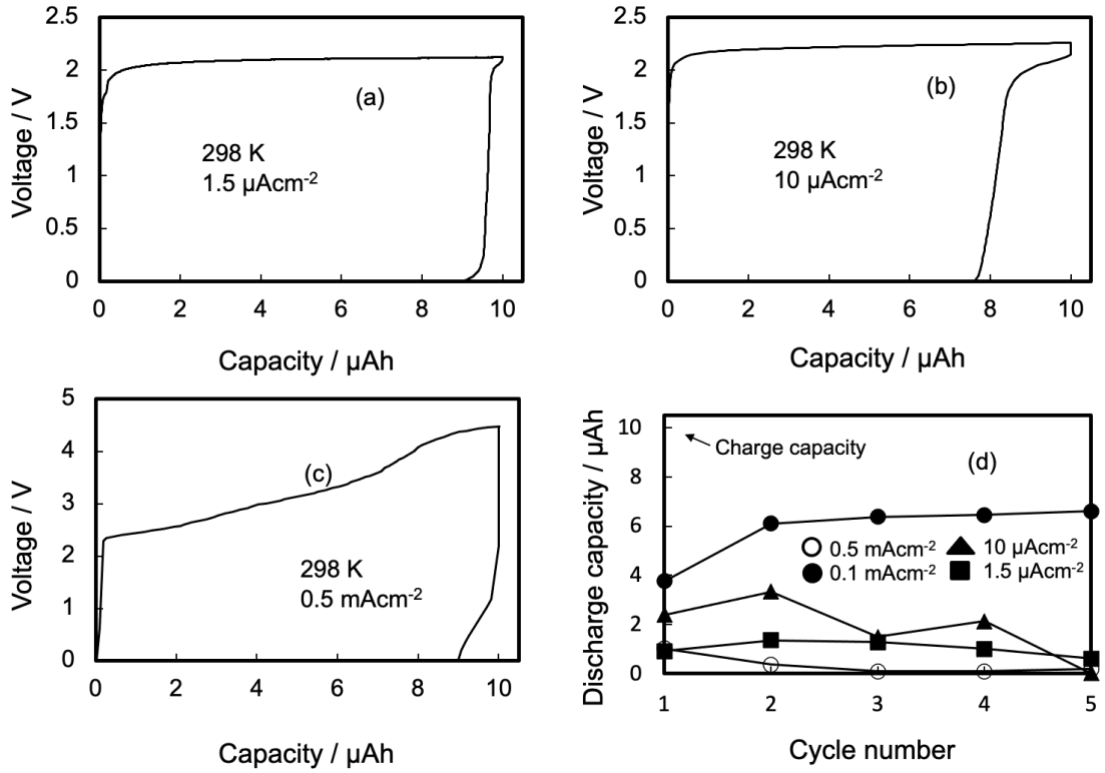

Figure 2-6 First charge-discharge curve of the Pt/ $Li_{1.5}Cr_{0.5}Ti_{1.5}(PO_4)_3$/Pt cell with different current density at 298 K, (a) 1.5 μA cm^{-2}, (b) 10 μA cm^{-2} and (c) 0.5 mA cm^{-2}. (d) Cycle property of the Pt/ $Li_{1.5}Cr_{0.5}Ti_{1.5}(PO_4)_3$/Pt cell with different current density at 298 K. The first charge-discharge curve at 0.1 mA cm^{-2} is shown in Fig. 2-5b.

2.3.3. Reaction Mechanism

In order to compare the morphology before and after the cycling test, transmission electron microscopy (TEM) is utilized. Figs. 2-7a, 2-7b, and 2-7c show the TEM images of the $Li_{1.5}Cr_{0.5}Ti_{1.5}(PO_4)_3$ before and after the cycling test. In the initial state, a brock-like particle has a smooth surface, and its particle size is in the 2–5 μm range. The smoothness of the surface was decreased after the cycling test. Therefore, connections in grain boundaries might be destroyed with charge– discharge cycling. Mapping results of EDS are shown in Fig. 2-8. In all cases, consistent elements are

uniformly dispersed. XPS was carried out to examine the oxidation states of chromium and titanium during charging, and Fig. 2-9 shows the Cr $2p_{3/2}$ XPS spectra of the cathode side of the Pt/ $Li_{1.5}Cr_{0.5}Ti_{1.5}(PO_4)_3$/Pt cell before and after charging. After charging, the XPS peak shifted to higher energy, indicating that the oxidation state of the chromium was increased. These spectra are consistent with reported values for the binding energies (Cr $2p_{3/2}$ binding energies for Cr^{3+} and Cr^{4+} of 577.6 and 579.2 eV, respectively) [21]. These results suggest that the charging plateau at 4.8 V is related to the oxidation of Cr^{3+} to Cr^{4+}. The anode side was also examined by XPS (Fig. 2-9b). After charging, the Ti $2p_{3/2}$ peak was shifted to a lower energy, indicating that the oxidation state of the titanium was decreased. Again, the binding energy values are consistent with the reported values (Ti $2p_{3/2}$ binding energies of 460 and 459 eV for Ti^{4+} and Ti^{3+}, respectively) [22,23]. One potential disadvantage of a single-phase all-solid-state battery is the electron leakage of the electrolyte. Because a single-phase cell includes an electrolyte and electrode, it conducts not only lithium ions but also electrons. Electron conduction in the $Li_{1.5}Cr_{0.5}Ti_{1.5}(PO_4)_3$ was assessed by investigating the self-discharge of the single-phase battery using this material, and Fig. 2-10 shows the time course of the open-circuit voltage for a Pt/$Li_{1.5}Cr_{0.5}Ti_{1.5}(PO_4)_3$/Pt cell after an initial charge. The cell voltage was maintained at over 2 V for approximately 20 h and the total time required for the voltage to decrease to 0 V was approximately 18 days. Therefore, the self-discharge rate for this cell was reasonably slow.

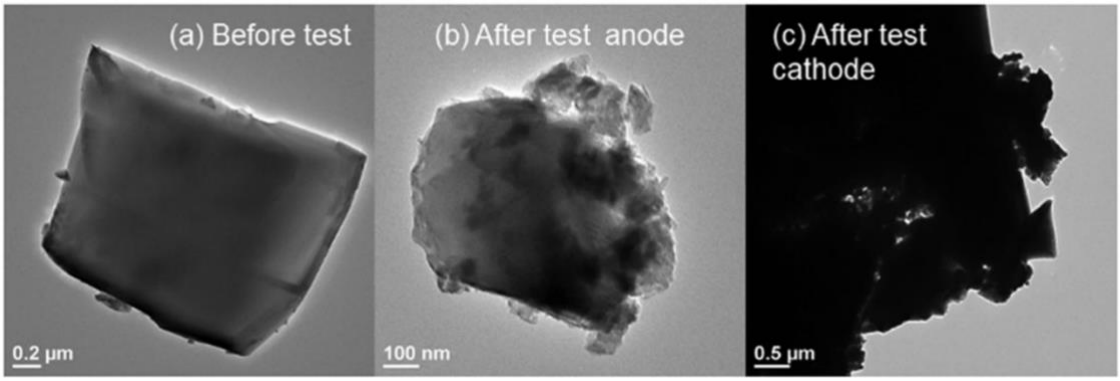

Figure 2-7 TEM images of $Li_{1.5}Cr_{0.5}Ti_{1.5}(PO_4)_3$ before and after the cycling test: (a) the initial state after sintering, (b) the anode surface after the 5th discharge, and (c) the cathode surface after the 5th discharge. All of the tests were carried out at 0.1 mA cm^{-2} and 298 K.

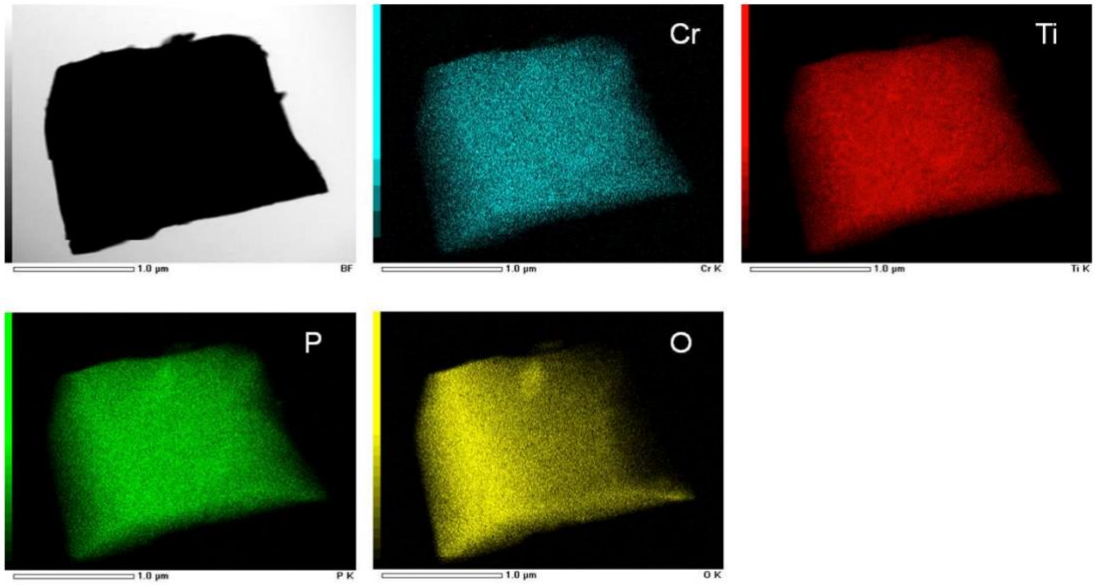

Figure 2-8 (a) Mapping results (TEM-EDS) of the $Li_{1.5}Cr_{0.5}Ti_{1.5}(PO_4)_3$ before cycling test.

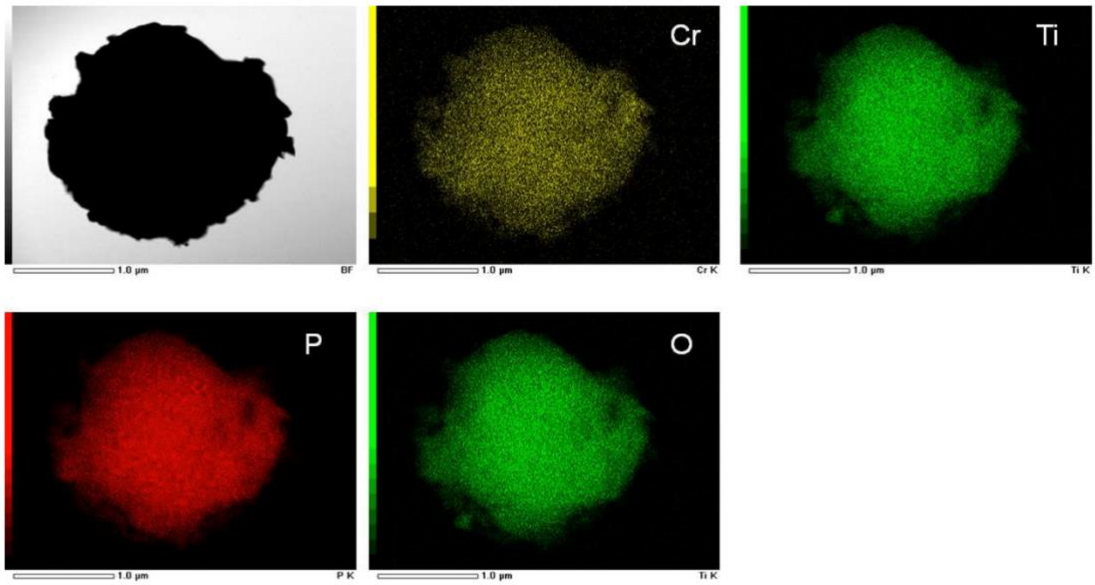

Figure 2-8 (b) Mapping results (TEM-EDS) of the anode side of $Li_{1.5}Cr_{0.5}Ti_{1.5}(PO_4)_3$ after cycling test.

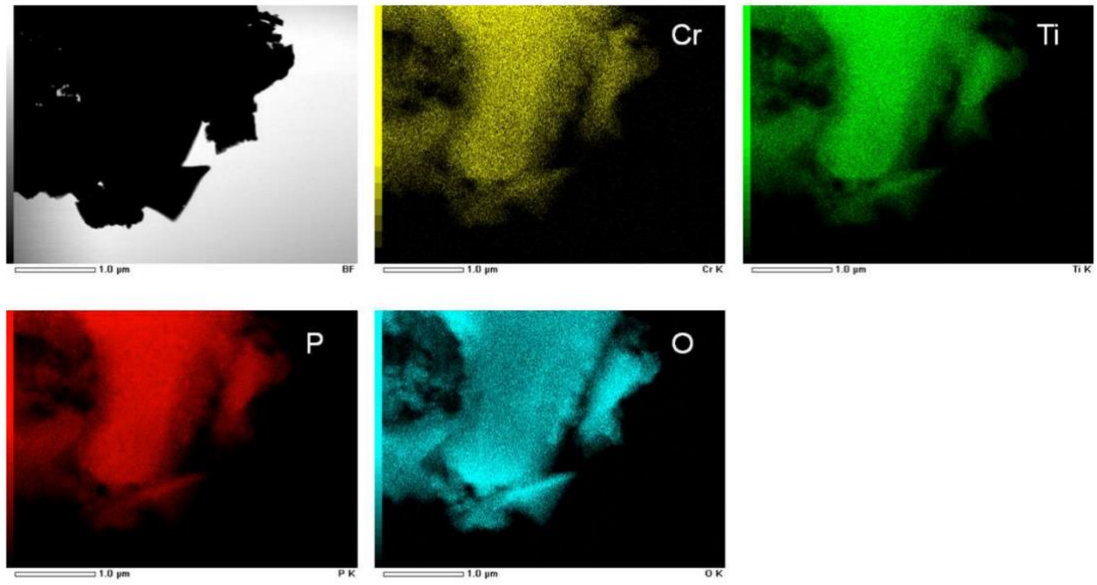

Figure 2-8 (c) Mapping results (TEM-EDS) of the cathode side of $Li_{1.5}Cr_{0.5}Ti_{1.5}(PO_4)_3$ after cycling test.

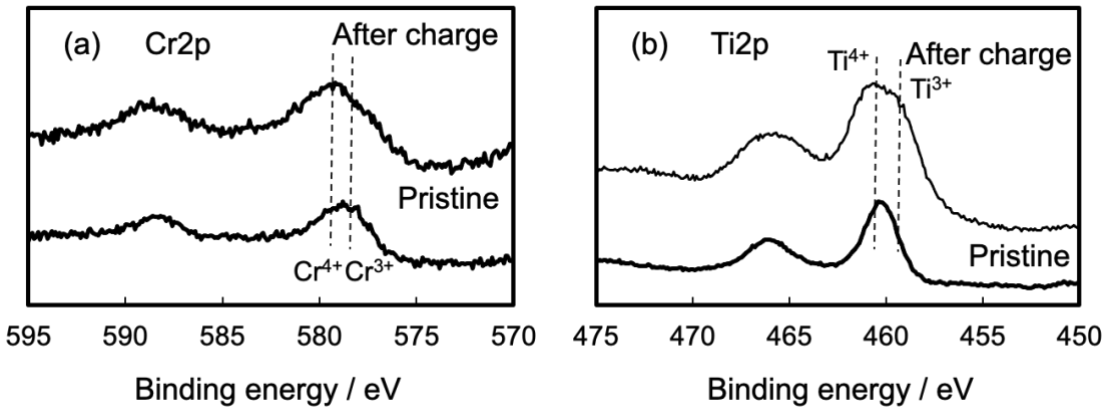

Figure 2-9 XPS spectra of $Li_{1.5}Cr_{0.5}Ti_{1.5}(PO_4)_3$ before and after charging: (a) Cr 2*p* spectra of cathode side and (b) Ti 2*p* spectra of anode side.

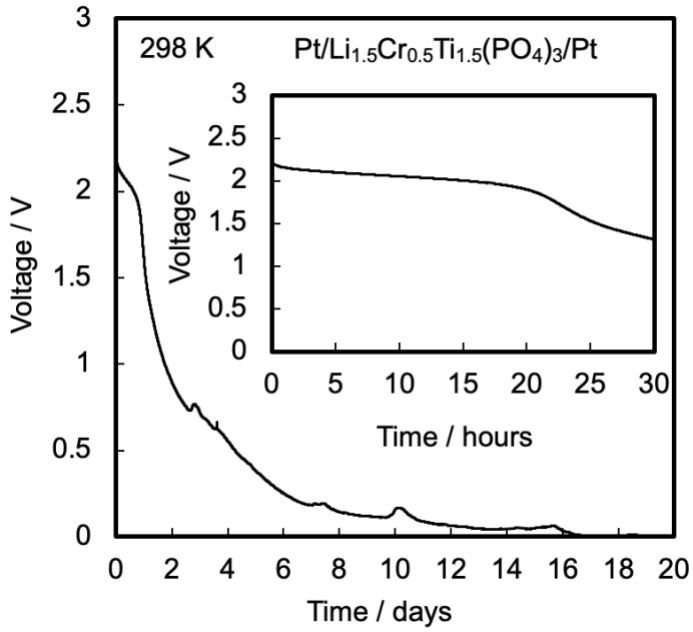

Figure 2-10 Time course of open-circuit voltage after initial charge.

2.4. Conclusions

In summary, the NASICON-type material $Li_{1.5}Cr_{0.5}Ti_{1.5}(PO_4)_3$ exhibited high ionic conductivity and was able to function as both a cathode and an anode based on the redox activity of the Cr^{3+}/Cr^{4+} and Ti^{4+}/Ti^{3+} couples, respectively. A high-rate capability (0.1 mA cm^{-2} at room temperature) and very low-temperature operation (233 K) were possible as a result of the superior ionic conductivity and low interfacial resistance obtained from the single-phase cell design. This concept of a single-phase battery with high ionic conductivity is expected to allow the development of new oxide-based ASSBs with high-rate capabilities.

References

[1] X. Xu, K. Takada, K. Watanabe, I. Sakaguchi, K. Akatsuka, B.T. Hang, T. Ohnishi, T. Sasaki, *Chem. Mater.* **23** (2011) 3798–3804.

[2] T. Inada, T. Kobayashi, N. Sonoyama, A. Yamada, S. Kondo, M. Nagao, R. Kanno, *J. Power Sources*. **194** (2009) 1085–1088.

[3] B. Lang, B. Ziebarth, C. Elsässer, *Chem. Mater.* **27** (2015) 5040–5048.

[4] H. Aono, E. Sugimoto, Y. Sadaoka, N. Imanaka, G.-Y. Adachi, *J. Electrochem. Soc.* **137** (1990) 1023–1027.

[5] J.F. Ihlefeld, P.G. Clem, B.L. Doyle, P.G. Kotula, K.R. Fenton, C.A. Apblett, *Adv. Mater.* **23** (2011) 5663–5667.

[6] J. van den Broek, S. Afyon, J.L. M Rupp, J. van den Broek, S. Afyon, J.L. M Rupp ETH Zurich, *Adv. Energy Mater.* **6** (2016) 1600736.

[7] L. Zeng, K. Kawahito, S. Ikeda, T. Ichikawa, H. Miyaoka, Y. Kojima, *Chem. Commun.* **51** (2015) 9773–9776.

[8] Y. Seino, T. Ota, K. Takada, A. Hayashi, M. Tatsumisago, *Energy Environ. Sci.* **7** (2014) 627–631.

[9] A. Hayashi, T. Ohtomo, F. Mizuno, K. Tadanaga, M. Tatsumisago, *Electrochem. Commun.* **5** (2003) 701–705.

[10] N. Kamaya, K. Homma, Y. Yamakawa, M. Hirayama, R. Kanno, M. Yonemura, T. Kamiyama, Y. Kato, S. Hama, K. Kawamoto, A. Mitsui, *Nat. Mater.* **10** (2011) 682–686.

[11] M. Nagao, A. Hayashi, M. Tatsumisago, *J. Mater. Chem.* **22** (2012) 10015–10020.

[12] F. Han, T. Gao, Y. Zhu, K.J. Gaskell, C. Wang, *Adv. Mater.* **27** (2015) 3473–

3483.

[13] A. Inoishi, T. Omuta, E. Kobayashi, A. Kitajou, S. Okada, *Adv. Mater. Interfaces*. **4** (2017) 3–7.

[14] A. Inoishi, T. Omuta, Y. Yoshioka, E. Kobayashi, A. Kitajou, S. Okada, *ChemistrySelect*. **2** (2017) 7925–7929.

[15] L.S. Plashnitsa, E. Kobayashi, Y. Noguchi, S. Okada, J. Yamaki, *J. Electrochem. Soc.* **157** (2010) A536.

[16] E. Kobayashi, A. Kitajou, S. Okada, J.I. Yamaki, *J. Power Sources*. **244** (2013) 312–317.

[17] E. Kobayashi, L.S. Plashnitsa, T. Doi, S. Okada, J.I. Yamaki, *Electrochem. Commun.* **12** (2010) 894–896.

[18] Y. Kee, N. Dimov, E. Kobayashi, A. Kitajou, S. Okada, *Solid State Ionics*. **272** (2015) 138–143.

[19] K. Yamamoto, Y. Iriyama, T. Asaka, T. Hirayama, H. Fujita, K. Nonaka, K. Miyahara, Y. Sugita, Z. Ogumi, *Electrochem. Commun.* **20** (2012) 113–116.

[20] P. Zhang, H. Wang, Q. Si, M. Matsui, Y. Takeda, O. Yamamoto, N. Imanishi, *Solid State Ionics*. **272** (2015) 101–106.

[21] M. Herklotz, F. Scheiba, R. Glaum, E. Mosymow, S. Oswald, J. Eckert, H. Ehrenberg, *Electrochim. Acta*. **139** (2014) 356–364.

[22] G.M. Weng, L.Y. Simon Tam, Y.C. Lu, *J. Mater. Chem. A*. **5** (2017) 11764–11771.

[23] J.-Y. Luo, L.-J. Chen, Y.-J. Zhao, P. He, Y.-Y. Xia, *J. Power Sources*. **194** (2009) 1075–1080.

[24] E.J. Plichta, W.K. Behl, *J. Power Sources*. **88** (2000) 192–196.

Chapter 3

Effect of Li_3BO_3 addition to NASICON-type Single-Phase All-Solid-State Lithium Battery Based on $Li_{1.5}Cr_{0.5}Ti_{1.5}(PO_4)_3$

3.1. Introduction

Rechargeable all-solid-state lithium-ion batteries with inorganic solid electrolytes have been attracting special attention recently as next-generation secondary batteries due to their non-flammability and high volumetric energy density [1–4]. Remarkably large ionic conductivity has been reported in sulfide-based solid electrolytes, which have lower Young's moduli than oxide-based solid electrolytes [5–8]. Dense sulfide-based electrolytes can thus be produced by cold pressing without a heating process to ensure sufficient contact between electrode and electrolyte materials. However, sulfide-based electrolytes potentially generate toxic H_2S due to reaction with water. In contrast, oxide-based solid electrolytes are rather stable in the atmosphere, although they have lower ionic conductivity and must be sintered at high temperature to achieve good contact between the electrode and electrolyte materials. Nevertheless, the reason why oxide-based ASSBs have not been put to practical use is that their interfacial resistance is

much larger than their electrolyte resistance [9]. One effective method to solve this problem is to construct a battery from a single material because we are released from the side reaction during preparation of the cell [10]. In that case, a single material must play three roles as the cathode, anode and electrolyte. The advantage of such a battery is a dense interface between the electrode and electrolyte by high-temperature sintering without interdiffusion. Inoishi *et al.* have recently reported some NASICON (Na Super Ionic CONductor)-type "single-phase" ASSBs that were fabricated from a single material [11–13]. A single-phase all-solid-state battery using NASICON-type $Li_{1.5}Cr_{0.5}Ti_{1.5}(PO_4)_3$ exhibited higher lithium-ionic conductivity and operating voltage than the $Li_3V_{2-x}Al_x(PO_4)_3$-based single-phase all-solid-state battery reported by Inoishi *et al.* previously [13]. As shown in Fig. 3-1, the $Li_{1.5}Cr_{0.5}Ti_{1.5}(PO_4)_3$ single-phase all- solid-state battery exhibits charge-discharge reactions based on the redox reactions of the Cr^{3+}/Cr^{4+} (cathode) and Ti^{4+}/Ti^{3+} (anode), which results in an operating voltage of 2.2 V. However, $Li_{1.5}Cr_{0.5}Ti_{1.5}(PO_4)_3$ has a low relative density, which results in low ionic conductivity [14]. According to Aono *et al*., the addition of Li_3BO_3 to $LiTi_2(PO_4)_3$ improves its density and ionic conductivity because Li_3BO_3 fills the voids in $LiTi_2(PO_4)_3$ [15,16]. On the other hand, $Li_{1.5}Cr_{0.5}Ti_{1.5}(PO_4)_3$ does exhibit slight electron leakage, which causes a low reversible capacity [13]. It is expected that mixing of the Li_3BO_3 "pure ionic conductor" with $Li_{1.5}Cr_{0.5}Ti_{1.5}(PO_4)_3$ would be effective to suppress this electron leakage, which would lead to a higher operating voltage and reversible capacity. In this paper, I report the effect of Li_3BO_3 addition to $Li_{1.5}Cr_{0.5}Ti_{1.5}(PO_4)_3$ on the porosity, ionic conductivity and charge-discharge performance of the battery.

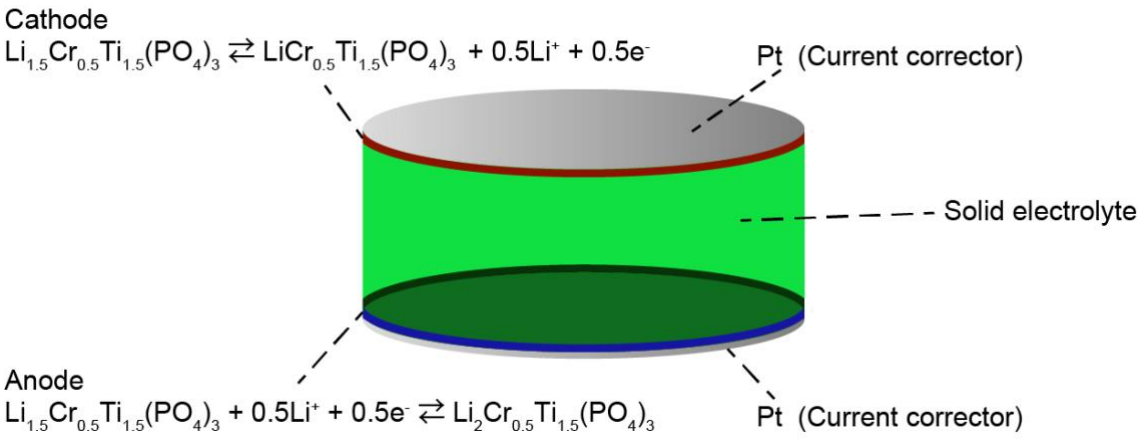

Figure 3-1 Schematic illustration of a single-phase all-solid-state battery cell.

3.2. Experimental

3.2.1. Materials Synthesis and Pelletization

$Li_{1.5}Cr_{0.5}Ti_{1.5}(PO_4)_3$ powder was stoichiometrically prepared using Li_2CO_3 (Wako Pure Chemical Industries, Ltd.), Cr_2O_3 (Wako Pure Chemical Industries, Ltd.), TiO_2 (Sigma Aldrich) and $NH_4H_2PO_4$ (Nacalai Tesque, Inc.) by the conventional solid-state reaction method. The mixture was sintered at 1273 K for 5 h in air. The product was then pelletized and annealed at 1373 K for 5 h in air. To prepare a $Li_{1.5}Cr_{0.5}Ti_{1.5}(PO_4)_3$-$Li_3BO_3$ composite pellet, $Li_{1.5}Cr_{0.5}Ti_{1.5}(PO_4)_3$ powder and Li_3BO_3 powder (Toshima Manufacturing Co., Ltd.) were mixed in a molar ratio of 10:1, and annealed at 1273 K for 5 h in air.

3.2.2. Materials Characterization

The XRD measurements (Cu Kα) were conducted using a Rigaku MiniFlex600 diffractometer. The scanning electron microscopy (SEM) analysis was performed using a JEOL JSM-6340F microscope.

3.2.3. Electrochemical Characterization

A thin platinum layer was sputtered on both sides of a sample pellet as a current collector. The cell was finally sealed into an HS cell (Hohsen Corp.) in an Ar-filled glove box. The electrochemical charge-discharge measurements were performed using the galvanostatic method with a charge-discharge cycle instrument (BTS2400W, Nagano

Electric Co.). The AC impedance measurements were executed under open-circuit conditions using an impedance analyzer (VersaSTAT3-400, AMETEC. Inc.) over the frequency range from 10 MHz to 0.1 Hz.

3.3. Results and Discussion

3.3.1. Materials Characterization

Figure 3-2 shows XRD pattern of the formed pellets, which confirm the NASICON-type structure. The SEM images in Fig. 3-3 show that the $Li_{1.5}Cr_{0.5}Ti_{1.5}(PO_4)_3$-$Li_3BO_3$ pellet has higher density than the $Li_{1.5}Cr_{0.5}Ti_{1.5}(PO_4)_3$ pellet. The relative densities of the $Li_{1.5}Cr_{0.5}Ti_{1.5}(PO_4)_3$ and $Li_{1.5}Cr_{0.5}Ti_{1.5}(PO_4)_3$-$Li_3BO_3$ pellets were calculated based on the Archimedes' method to be 80.1% and 91.9%, respectively. The relative density was increased due to Li_3BO_3 acting as binder and filling the pores.

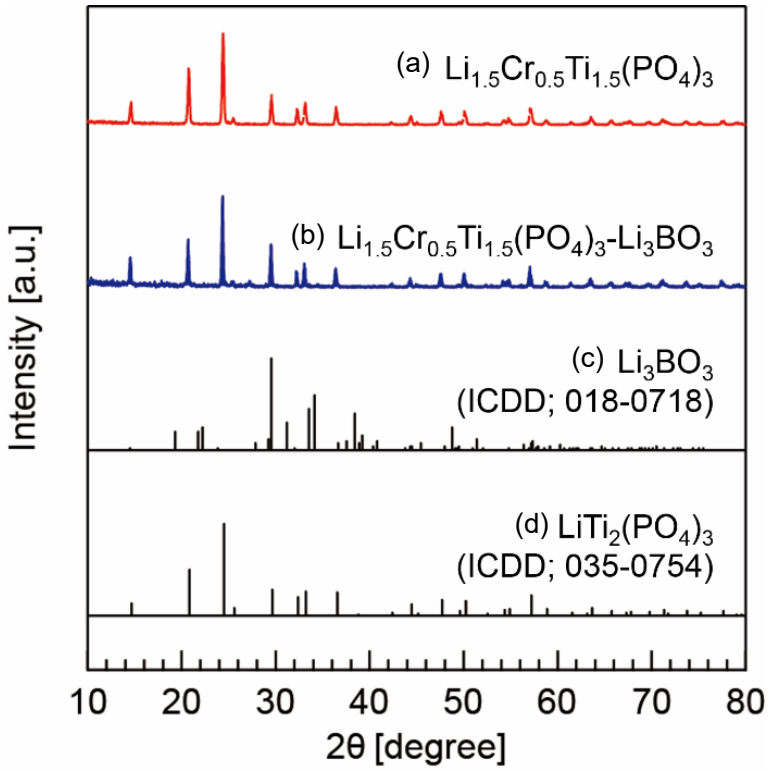

Figure 3-2 XRD patterns of the (a) $Li_{1.5}Cr_{0.5}Ti_{1.5}(PO_4)_3$ pellet, (b) $Li_{1.5}Cr_{0.5}Ti_{1.5}(PO_4)_3$-$Li_3BO_3$ pellet, and ICSD of (c) Li_3BO_3 and (d) $LiTi_2(PO_4)_3$.

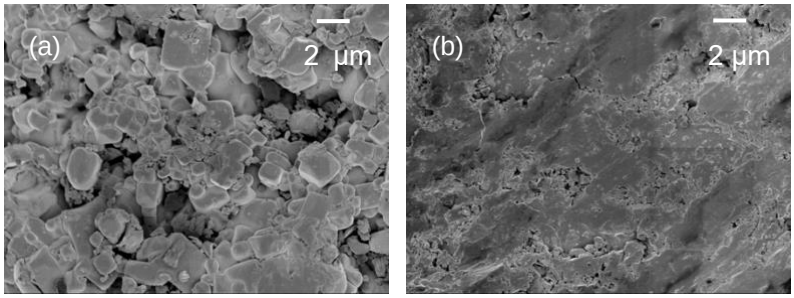

Figure 3-3 SEM images of (a) $Li_{1.5}Cr_{0.5}Ti_{1.5}(PO_4)_3$ and (b) $Li_{1.5}Cr_{0.5}Ti_{1.5}(PO_4)_3$-$Li_3BO_3$ pellets.

3.3.2. Electrochemical Properties

For electrochemical measurements, the pellets were sputtered on both faces with Pt to function as a current collector. Figures 3-4a and 3-4b show impedance plots for $Li_{1.5}Cr_{0.5}Ti_{1.5}(PO_4)_3$ and $Li_{1.5}Cr_{0.5}Ti_{1.5}(PO_4)_3$-$Li_3BO_3$, respectively. The impedance spectra for both pellets had a semicircle and a spike in the low-frequency region. It should be noted that the measured conductivity includes not only ionic conductivity but also electronic conductivity because $Li_{1.5}Cr_{0.5}Ti_{1.5}(PO_4)_3$ contains transition metals. Therefore, the measured conductivity is mixed conductivity. Figure 3-5 shows the temperature dependence of the electrical conductivity, from which $Li_{1.5}Cr_{0.5}Ti_{1.5}(PO_4)_3$-$Li_3BO_3$ pellet exhibited the highest electrical conductivity of 2.6×10^{-4} S cm^{-1} at 298 K, even though the electrical conductivity of $Li_{1.5}Cr_{0.5}Ti_{1.5}(PO_4)_3$ was only 1.4×10^{-4} Scm^{-1}. The observed electrical conductivity of $Li_{1.5}Cr_{0.5}Ti_{1.5}(PO_4)_3$-$Li_3BO_3$ pellet is still lower than the ionic conductivity of $Li_{1.3}Al_{0.3}Ti_{1.7}(PO_4)_3$. ($7\times10^{-4}$ Scm^{-1}) [14]. One of the important factors to increase conductivity is to increase the relative density. The relative density of the $Li_{1.5}Cr_{0.5}Ti_{1.5}(PO_4)_3$-$Li_3BO_3$ pellet was larger than that of $Li_{1.5}Cr_{0.5}Ti_{1.5}(PO_4)_3$ pellet,

which may indicate that the higher electrical conductivity of the $Li_{1.5}Cr_{0.5}Ti_{1.5}(PO_4)_3$-$Li_3BO_3$ pellet was due to its larger relative density. Figure 3-6 shows the first charge-discharge curves of the Pt/$Li_{1.5}Cr_{0.5}Ti_{1.5}(PO_4)_3$/Pt and Pt/$Li_{1.5}Cr_{0.5}Ti_{1.5}(PO_4)_3$-$Li_3BO_3$/Pt cells at room temperature. The Pt/$Li_{1.5}Cr_{0.5}Ti_{1.5}(PO_4)_3$-$Li_3BO_3$/Pt cell showed a larger overpotential than the Pt/$Li_{1.5}Cr_{0.5}Ti_{1.5}(PO_4)_3$/Pt cell. Some possible reasons for this are, first, increased electrode resistance due to the reaction of $Li_{1.5}Cr_{0.5}Ti_{1.5}(PO_4)_3$ and Li_3BO_3. Second, the charge-transfer resistance is increased by the decrease in electronic conductivity by the addition of the pure lithium-ionic conductor, Li_3BO_3. On the other hand, the operating voltage of the Pt/$Li_{1.5}Cr_{0.5}Ti_{1.5}(PO_4)_3$-$Li_3BO_3$/Pt cell was higher than that of the Pt/ $Li_{1.5}Cr_{0.5}Ti_{1.5}(PO_4)_3$/Pt cell. In addition, a larger reversible capacity was observed for the Pt/ $Li_{1.5}Cr_{0.5}Ti_{1.5}(PO_4)_3$-$Li_3BO_3$/Pt cell. The cycling properties were also improved by the addition of Li_3BO_3 (Fig. 3-7). These results indicate that internal short circuiting is suppressed by the addition of Li_3BO_3. Generally, the lithium-ion transference number of the solid electrolyte is expressed according to the following equation:

$$E_R = t_i \times E_t \qquad (1)$$

where E_R is the observed cell voltage, t_i is the ionic transference number of the electrolyte, and E_t is the theoretical cell voltage, respectively. Therefore, it is expected that ionic transport number of $Li_{1.5}Cr_{0.5}Ti_{1.5}(PO_4)_3$-$Li_3BO_3$ is larger than that of $Li_{1.5}Cr_{0.5}Ti_{1.5}(PO_4)_3$ if the theoretical EMF is same. To compare the electronic conduction, the time-dependence of the open-circuit voltage (OCV) was measured after initial charging of 10 μAh at 0.1 $mAcm^{-2}$ (Fig. 3-8). The decrease of the OCV is caused by self-discharge of the cell. Figure 3-8 shows that the Pt/$Li_{1.5}Cr_{0.5}Ti_{1.5}(PO_4)_3$-$Li_3BO_3$/Pt cell took a longer time to completely short-circuit and decrease until 0 V than the Pt/$Li_{1.5}Cr_{0.5}Ti_{1.5}(PO_4)_3$/Pt cell. In other words, $Li_{1.5}Cr_{0.5}Ti_{1.5}(PO_4)_3$-$Li_3BO_3$ has less electronic conductivity than $Li_{1.5}Cr_{0.5}Ti_{1.5}(PO_4)_3$. Considering both the results of the electrical conductivity

measurements and the self-discharge profiles, it is obvious that the lithium-ionic conductivity was increased and the electronic conductivity decreased by the addition of Li_3BO_3 to $Li_{1.5}Cr_{0.5}Ti_{1.5}(PO_4)_3$. I consider that Li_3BO_3 suppressed the electronic conducting paths and increased the ionic conducting paths because Li_3BO_3 has a low melting point and does not exhibit electron conductivity.

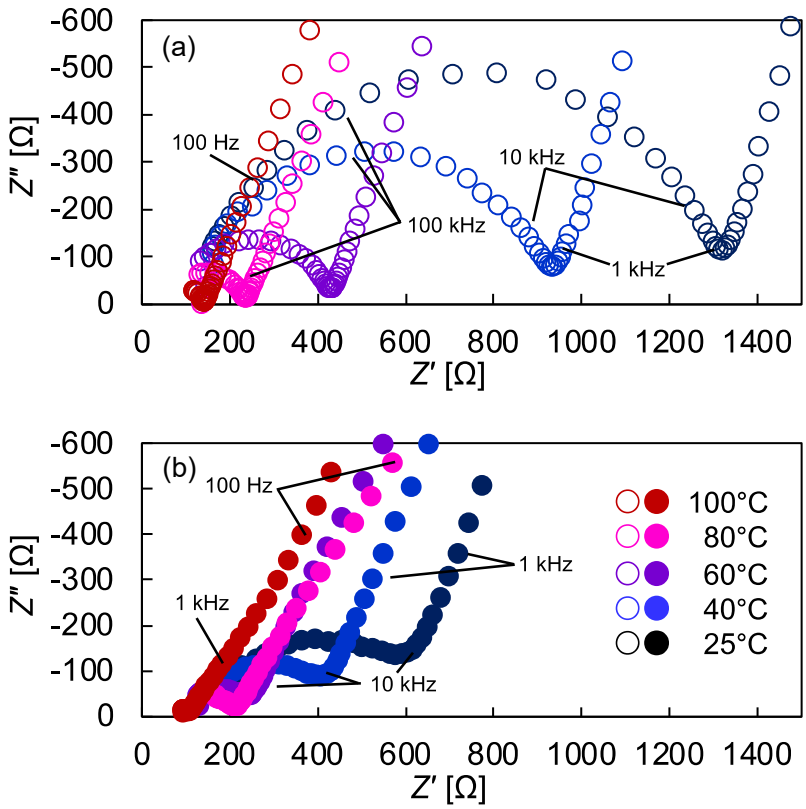

Figure 3-4 Impedance plots for (a) $Li_{1.5}Cr_{0.5}Ti_{1.5}(PO_4)_3$ and (b) $Li_{1.5}Cr_{0.5}Ti_{1.5}(PO_4)_3$-$Li_3BO_3$ at various temperature

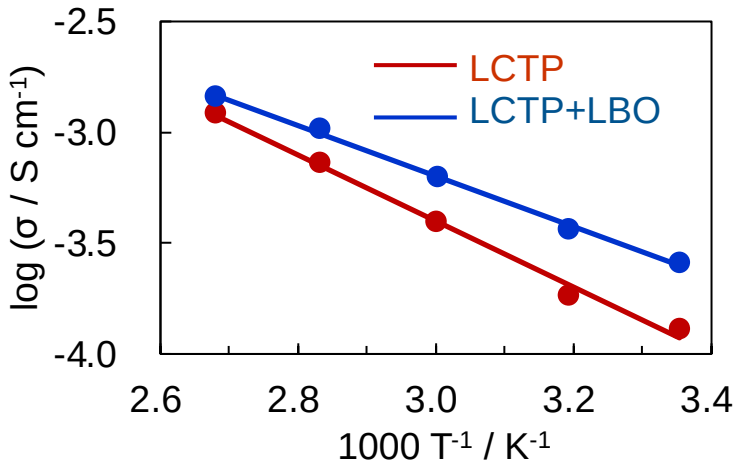

Figure 3-5 Arrhenius plots of the temperature-dependence conductivities for $Li_{1.5}Cr_{0.5}Ti_{1.5}(PO_4)_3$ and $Li_{1.5}Cr_{0.5}Ti_{1.5}(PO_4)_3$-$Li_3BO_3$.

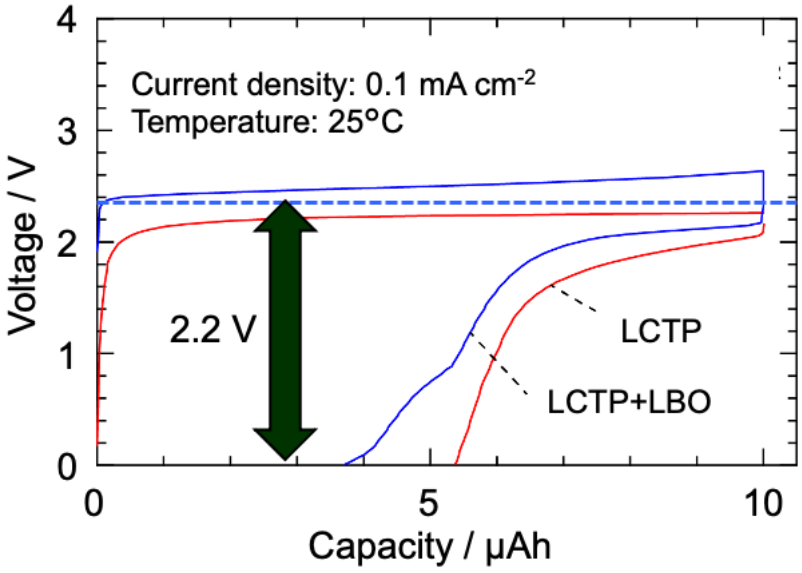

Figure 3-6 Charge-discharge profiles of the Pt/$Li_{1.5}Cr_{0.5}Ti_{1.5}(PO_4)_3$ /Pt (red line) and Pt/$Li_{1.5}Cr_{0.5}Ti_{1.5}(PO_4)_3$-$Li_3BO_3$/Pt (blue line) cells at a rate of 0.1 mA cm^{-2} at 298 K.

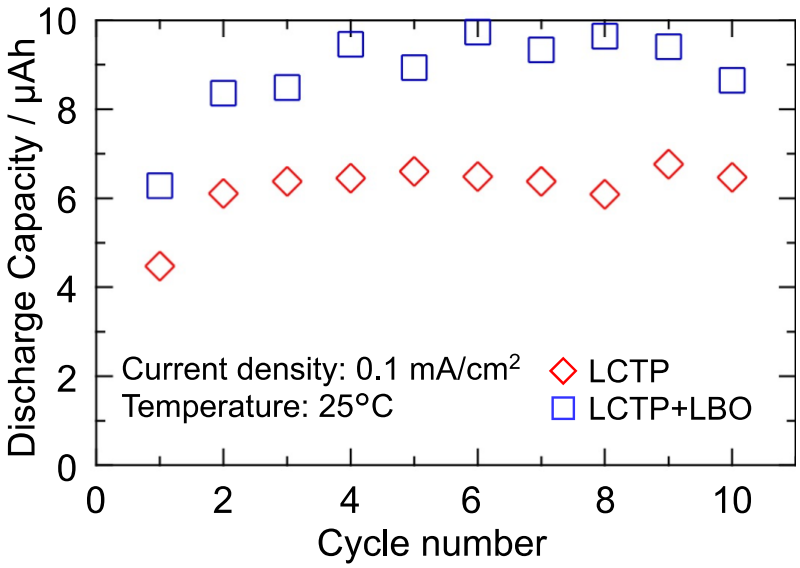

Figure 3-7 Cyclabilities of Pt/$Li_{1.5}Cr_{0.5}Ti_{1.5}(PO_4)_3$/Pt (◇) and Pt/$Li_{1.5}Cr_{0.5}Ti_{1.5}(PO_4)_3$-$Li_3BO_3$/Pt (□) cells at a rate of 0.1 mA cm^{-2} at 298 K.

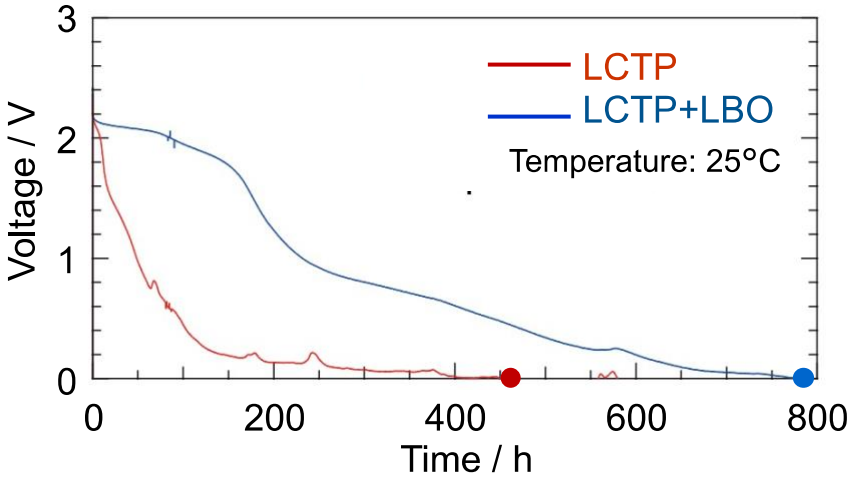

Figure 3-8 Self-discharge curves of the Pt/$Li_{1.5}Cr_{0.5}Ti_{1.5}(PO_4)_3$/Pt (red line) and Pt/ $Li_{1.5}Cr_{0.5}Ti_{1.5}(PO_4)_3$-$Li_3BO_3$/Pt (blue line) cells at 298 K.

3.4. Conclusions

Single-phase all-solid-state lithium-ion batteries were prepared using $Li_{1.5}Cr_{0.5}Ti_{1.5}(PO_4)_3$, and the effect of Li_3BO_3 addition to $Li_{1.5}Cr_{0.5}Ti_{1.5}(PO_4)_3$ was investigated. The density and the lithium-ion transference number of $Li_{1.5}Cr_{0.5}Ti_{1.5}(PO_4)_3$ was successfully improved by Li_3BO_3, although the overpotential of the battery cells increased. It was also confirmed that the operation voltage and the reversible capacity increased due to the increase of the lithium-ion transference number. Suppression of the electron leakage was observed by the addition of Li_3BO_3 to $Li_{1.5}Cr_{0.5}Ti_{1.5}(PO_4)_3$. Therefore, it is expected that Li_3BO_3 addition will be an effective approach to improve the properties of single-phase all-solid-state lithium-ion batteries with mixed conducting materials. In future research, I will elucidate the mechanism for the increased lithium-ionic conductivity by Li_3BO_3 addition and the effect of compositing lithium salt into battery materials.

References

[1] J.-M.M. Tarascon, M. Armand, *Nature*. **414** (2001) 359–367.

[2] K. Takada, *Acta Mater.* **61** (2013) 759–770.

[3] C. Yada, A. Ohmori, K. Ide, H. Yamasaki, T. Kato, T. Saito, F. Sagane, Y. Iriyama, *Adv. Energy Mater.* **4** (2014) 5–6.

[4] Y. Gambe, Y. Sun, I. Honma, *Sci. Rep.* **5** (2015) 10–13.

[5] N. Kamaya, K. Homma, Y. Yamakawa, M. Hirayama, R. Kanno, M. Yonemura, T. Kamiyama, Y. Kato, S. Hama, K. Kawamoto, A. Mitsui, *Nat. Mater.* **10** (2011) 682–686.

[6] A. Hayashi, K. Noi, A. Sakuda, M. Tatsumisago, *Nat. Commun.* **3** (2012) 2–6.

[7] Y. Seino, T. Ota, K. Takada, A. Hayashi, M. Tatsumisago, *Energy Environ. Sci.* **7** (2014) 627–631.

[8] Z. Ma, H.G. Xue, S.P. Guo, *J. Mater. Sci.* **53** (2018) 3927–3938.

[9] K. Takada, *Langmuir*. **29** (2013) 7538–7541.

[10] F. Han, T. Gao, Y. Zhu, K.J. Gaskell, C. Wang, *Adv. Mater.* **27** (2015) 3473–3483.

[11] A. Inoishi, T. Omuta, E. Kobayashi, A. Kitajou, S. Okada, *Adv. Mater. Interfaces*. **4** (2017) 3–7.

[12] A. Inoishi, T. Omuta, Y. Yoshioka, E. Kobayashi, A. Kitajou, S. Okada, *ChemistrySelect.* **2** (2017) 7925–7929.

[13] A. Inoishi, A. Nishio, Y. Yoshioka, A. Kitajou, S. Okada, *Chem. Commun.* **54** (2018) 3178–3181.

[14] H. Aono, E. Sugimoto, Y. Sadaoka, N. Imanaka, G. ya Adachi, *Solid State Ionics*. **40**–**41** (1990) 38–42.

[15] H. Aono, E. Sugimoto, Y. Sadaoka, N. Imanaka, G. ya Adachi, *Solid State Ionics*. **47** (1991) 257–264.

[16] H. Aono, E. Sugimoto, Y. Sadaoka, N. Imanaka, G. Adachi, *Chem. Lett.* **19** (1990) 331–334.

Chapter 4

Effect of Na_3BO_3 Addition into $Na_3V_2(PO_4)_3$ Single-Phase All-Solid-State Batteries

4.1. Introduction

The demand for safe batteries has also increased and ASSBs have been considered as one of the safest battery types due to the use of inorganic solid electrolytes, which are nonflammable materials, in contrast to conventional batteries that employ flammable organic electrolytes [1–3]. Furthermore, sulfide materials in sulfide-based batteries can react with oxygen and moisture in the air and emit harmful SO_x and H_2S. Therefore, oxide-based ASSBs promise to be the safest batteries due to their nonflammability and atmospheric stability. Many types of oxide-based solid electrolytes have been studied for application to LIBs. On the other hand, there have been few studies on novel oxide-based Na-ion conductors, such as $Na_3Zr_2Si_2PO_{12}$ (NZSP), which is a Na-ion Super Ionic CONductor (NASICON)-type compound, and β-Al_2O_3 [4–6]. The main problem with the oxide-based ASSBs is the interfacial resistance between the solid electrodes and solid electrolyte. The interfacial resistance is caused by the impedance mismatch, space charge layer and impurity formation due to side reactions between the

electrodes and solid electrolyte materials during high-temperature firing [2,7]. To overcome such difficulties, I have focused on a new battery system termed a single-phase all-solid-state battery, which is constructed from a single material that has all the functions of the positive electrode, negative electrode and electrolyte [8–12]. For single-phase ASSBs, the electrodes must be formed *in-situ* from the solid electrolyte by current flow. Some *in-situ* formed electrodes have been investigated, and the Li_2O-Al_2O_3-TiO_2-P_2O_5 glass ceramics sheet, which has a similar composition to the $Li_{1.5}Al_{0.5}Ti_{1.5}(PO_4)_3$ NASICON-type Li-ion conductor, has been investigated the most [13–15]. NASICON-type materials have an ideal crystal structure for single-phase ASSBs due to their wide bottle neck and facile substitution by elements such as alkali metals and transition metals [5]. One of the NASICON-type materials, $Na_{3-x}V_{2-x}Zr_x(PO_4)_3$, has been reported to possess the properties of Na-ion migration for single-phase ASSBs, and has exhibited reasonable characteristics for solid electrolyte and electrodes [9]. To further improve the properties, I have also reported the addition of a lithium salt, Li_3BO_3, which has a low melting point, to a single-phase all-solid-state Li-ion battery that uses $Li_{1.5}Cr_{0.5}Ti_{1.5}(PO_4)_3$. The ionic conductivity and the charge/discharge properties were successfully increased by filling the voids of the high porosity $Li_{1.5}Cr_{0.5}Ti_{1.5}(PO_4)_3$ sintered body with Li_3BO_3 which is a Li-ionic conductor [16].

In this chapter, I investigated the effect of Na_3BO_3 (NBO) addition into $Na_3V_2(PO_4)_3$ (NVP) to improve the properties of NVP for application as a single-phase all-solid-state battery. NVP has previously been reported to exhibit battery properties with the mechanism shown in Fig. 4-1 [9]. NVP and NBO were synthesized and characterized as the precursor for a sintered body. The precursors were mixed in certain ratios, and the addition of NBO was evaluated with respect to the resultant electrochemical properties of NVP. Optical observation was employed at the end of this research to confirm if the

NBO additive and the porosity of the pellets had an effect on the *in-situ* formation of the electrodes.

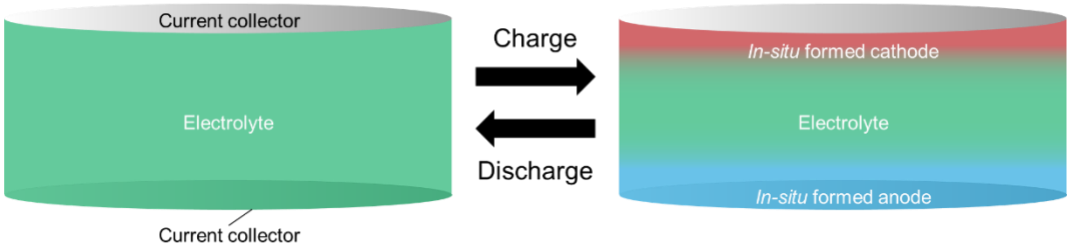

Cathode: $Na_3V_2(PO_4)_3 \rightleftarrows NaV_2(PO_4)_3 + 2Na^+ + 2e^-$

Anode: $Na_3V_2(PO_4)_3 + Na^+ + e^- \rightleftarrows Na_4V_2(PO_4)_3$

Figure 4-1 Schematic model of an NVP-based single-phase all-solid-state battery cell.

4.2. Experimental

4.2.1. Materials Synthesis

NVP powder and NBO powder were synthesized by the conventional solid-state reaction method. NaH_2PO_4 (Fujifilm Wako; min 99.0 %) and V_2O_5 (Fujifilm Wako; min 99.0 %) were mixed in a stoichiometric ratio by hand milling in an agate mortar as the raw materials for NVP. The mixture was then sintered at 900 °C for 20 h under Ar+5 %H_2 gas flow for reduction of the valence of vanadium from pentavalent to trivalent. The fired mixture was crushed and sintered again under the same conditions to obtain single-phase NVP. NBO was synthesized in an Ar-filled glove box using NaOH (Fujifilm Wako; 97.0 %) and H_3BO_3 (Fujifilm Wako, min; 99.5 %) which were dried under vacuum at 350 °C before being placed in the glove box. The primary materials were mixed and calcined at 400 °C for 4 h. The precursor was then crushed and sintered at 450 °C for 2 h.

4.2.2. Pelletization

NVP powder and NBO powder were mixed in molar ratios of 95:5, 90:10 and 85:15 by hand-milling with an agate mortar in an Ar-filled glove box. The precursor powder was uniaxially pressed at 255 MPa and then isostatically pressed at 300 MPa after packing the pellets in a plastic cover under vacuum. The pellets were annealed at 900 °C or 800 °C for 5 h in an Ar+5 %H_2 atmosphere on a precursor powder bed on an alumina plate. The pellets obtained were polished with sandpaper to adjust the thickness to between 0.7 and 0.8 mm. The ball-milled precursor powder was also supplementary

employed to improve the electrical conductivity of the pellets. The precursor was ball-milled at 150 rpm for 3 h using a planetary mill (Pulverisette 7, Fritsch).

4.2.3. Materials Characterization

XRD data for NVP, NBO and the pellets were collected to identify the crystal structure at room temperature using an X-ray diffractometer (Miniflex 600, Rigaku) with Cu Kα radiation. The samples were measured in steps of 0.01° in the 2θ angular range of 10–80° at a scan rate of 10° min^{-1}. The morphology and composition of the NVP, NBO and pellet samples were obtained using scanning electron microscopy-energy dispersive X-ray spectroscopy (SEM-EDS; NeoScope JCM-7000, JEOL) analysis.

4.2.4. Electrochemical Characterization

Thin platinum layers were sputtered on both sides of a sample pellet as current collectors. The pellets were then evacuated at 150 °C to remove any moisture and oxygen. An HS cell (Hohsen Corp.) was employed for all electrochemical measurements. All the cells were assembled in an Ar-filled glove box (dew point < -80 °C). Impedance measurements were performed using an impedance analyzer (SP-300; Biologic) in the frequency range of 0.1 Hz to 7 MHz at temperatures from 25 °C to 120 °C. Impedance fitting was conducted using equivalent circuit modeling software (ZView, Scribner Associates, Inc.). Charge and discharge measurements were performed using a galvanostatic instrument (HJ1020mSD8, Hokuto Denko) at 100 °C. The current density was 15 μA cm^{-2} and the capacity was regulated to 30 μAh to maintain a constant state of charge each time because the single-phase all-solid-state battery did not have a clear

electrode area.

4.2.5. Investigation of *in-situ* Formed Electrode

The *in-situ* formed electrode was investigated by observation of the surface on the negative electrode side of a charged pellet because compared to the initial color of the pellet, the color of the negative electrode side changed much more than that of the positive electrode side. The NVP and NVP+NBO pellets were charged to 3.0 V at 0.015 mA cm^{-2} and then removed from the HS cell in air. The pellets were immediately observed and optical micrographs were obtained, and SEM and an EDS mapping system were employed. The surface of the pellets was observed at an arbitrary thickness using sandpaper to slightly polish the surface of the pellets until there were no color-changed areas which was the maximum area that the *in-situ* electrode formed.

4.3. Results & Discussion

4.3.1. Materials Characterization

NVP and NBO powders were synthesized by the conventional solid-state reaction method following the procedures given in the experimental section. The XRD profiles for NVP and NBO powder are presented with the ICSD for $Na_3V_2(PO_4)_3$ (No. 248140; $R\bar{3}c$) and Na_3BO_3 (No. 1351; $P12_1/c1$) in Fig. 4-2. The XRD pattern for as-synthesized NVP was consistent with the ICSD for $Na_3V_2(PO_4)_3$ with a secondary phase of V_2O_3. The as-synthesized NBO was confirmed to be single phase. The NVP+NBO(85:15) pellet was annealed at 800 °C because the pellet sintered at 900 °C adhered to the alumina plate and was difficult to remove. Figure 4-3 shows XRD patterns for the NVP and the NVP+NBO pellets with NVP:NBO mixing ratios of 95:5, 90:10 and 85:15. The NVP phase was observed in the XRD profiles for all of the NVP+NBO pellets, and trace amounts of an unknown impurity were confirmed, the peak intensity of which increased with the amount of added NBO. In addition, it is assumed that no NBO phase was observed due to its amorphization by high-temperature annealing.

The relative densities of the NVP and NVP+NBO pellets were calculated based on the Archimedes method and the results are shown in Fig. 4-4a. The addition of NBO to NVP increased the relative density of the sintered pellets; however, excess addition such as >15 % NBO was not as effective as the addition of 5 % and 10 % NBO. The relative densities of the NVP and NVP+NBO (95:5, 90:10 and 85:15) pellets were 77.3, 81.7, 86.7 and 81.1 %, respectively. Figs. 4-4b and 4-4c show SEM images of the NVP and NVP+NBO (95:5) pellets. The voids in the NVP+NBO pellet were more filled than those in the NVP pellet. The reduction of voids by the addition of NBO to NVP as shown

in the SEM images is consistent with the increase in the relative densities of the NVP+NBO pellets.

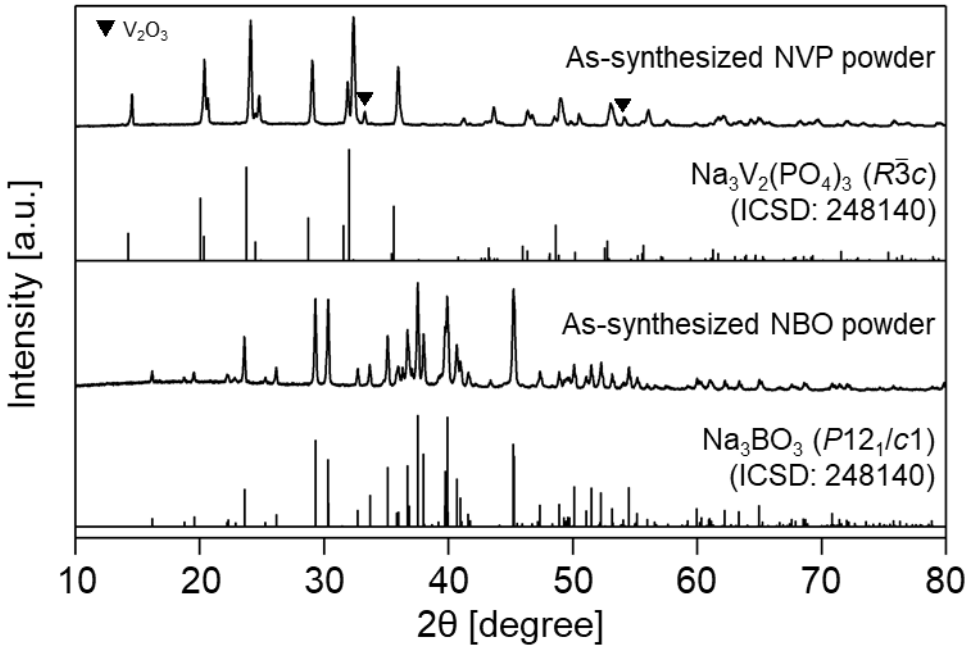

Figure 4-2 XRD profiles for the as-synthesized NVP powder, NBO powder, and ICSD of $Na_3V_2(PO_4)_3$ (No. 248140) and Na_3BO_3 (No. 1351).

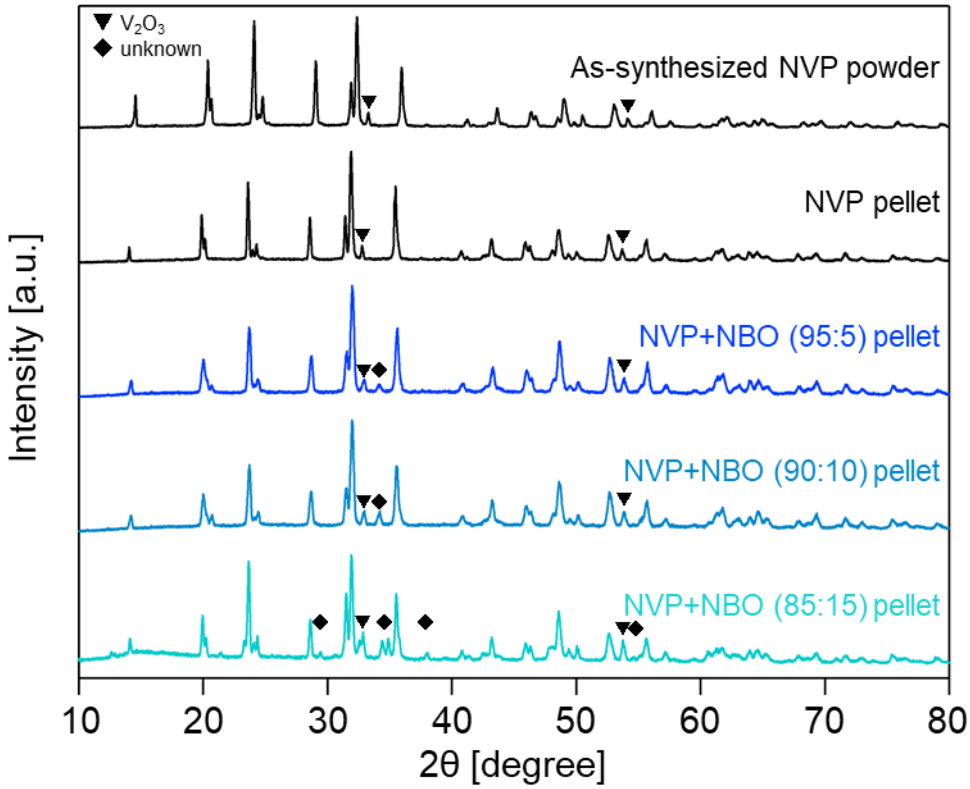

Figure 4-3 XRD profiles for the as-synthesized NVP powder and NVP+NBO pellets for each mixing ratio (NVP:NBO = 100:0, 95:5, 90:10, 85:15).

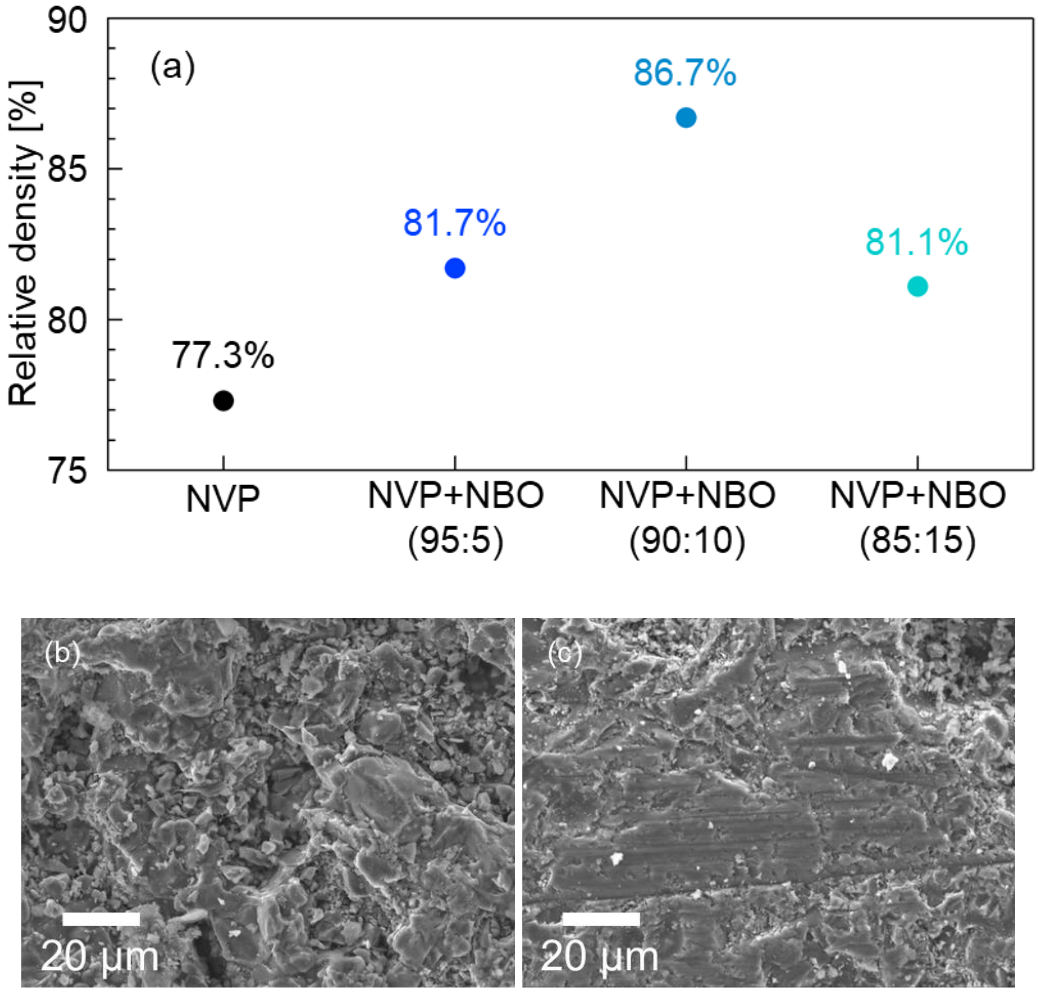

Figure 4-4 (a) Relative densities of the NVP and the NVP+NBO pellets (95:5, 90:10 and 85:15). Cross-sectional SEM micrographs of the (b) NVP and (c) NVP+NBO pellets.

4.3.2. Impedance Analysis

Figs. 4-5a and 4-5b show Nyquist plots and Arrhenius plots of the total electrical conductivity (σ_{total}) for the Pt/NVP/Pt and Pt/NVP+NBO(95:5)/Pt cells. The mixing ratio of NVP:NBO = 95:5 was the optimum ratio and this pellet showed the highest conductivity among the NVP+NBO pellets, as shown in Table 1. Note that the

conductivity of the NVP pellet is not indicated as ionic conductivity but as electrical conductivity, which is the sum of the ionic conductivity and electronic conductivity, because NVP is not only an ionic conductor but also an electrical conductor because the 3*d* transition metal vanadium is included. From this point on, all measurements were performed using NVP+NBO pellets with a mixing ratio of 95:5. In Fig. 4-5a, the total resistance was calculated as the value of the sum for the bulk resistance and the grain boundary resistance. Two capacitive semicircles were apparent for the Pt/NVP/Pt and the Pt/NVP+NBO/Pt cells, while three capacitive semicircles were most suitable for fitting the impedance as a result of the bulk resistance, the grain boundary resistance and the contact resistance between the pellet and Pt film current collectors, as shown in Fig. 4-6. Figure 4-5b compares Arrhenius plots of the total electrical conductivity (σ_{total}) for the NVP and NVP+NBO pellets; the slope for the NVP+NBO pellet was steeper than that for the NVP pellet, suggesting that the activation energy was increased by the addition of NBO to NVP. For more detailed analysis, impedance fitting was conducted for each temperature, and the electrical conductivities and activation energies were calculated based on the bulk resistance and grain boundary resistance. The bulk, grain boundary and total electrical conductivities (σ_{bulk}, σ_{gb}, σ_{total}, respectively) and the activation energy (E_a) for the NVP and NVP+NBO pellets are given in Table 1. The Arrhenius plots of σ_{bulk} and σ_{gb} for the NVP and NVP+NBO pellets are shown in Fig. 4-5c. σ_{total} was improved from 4.9×10^{-6} S cm^{-1} to 8.5×10^{-5} S cm^{-1} at 100 °C, and σ_{bulk} and σ_{gb} were also increased at each temperature by the addition of NBO to NVP. On the other hand, $E_{a\ total}$ for the NVP+NBO pellet was larger than that for the NVP pellet, although $E_{a\ bulk}$ was the same for both the NVP and NVP+NBO pellets. The increase in $E_{a\ total}$ was most likely due to the doubling of $E_{a\ gb}$. These results could be due to the addition of NBO with a lower melting point, which filled the voids between NVP particles, but also increased the transfer barrier for

Na ions as the ions pass through the NVP particles to the NBO particles with lower ionic conductivity. In addition, as shown in Table 1, the electrical conductivity was successfully improved by the ball-milling process before pelletization due to the decrease in the grain size of the precursor powder.

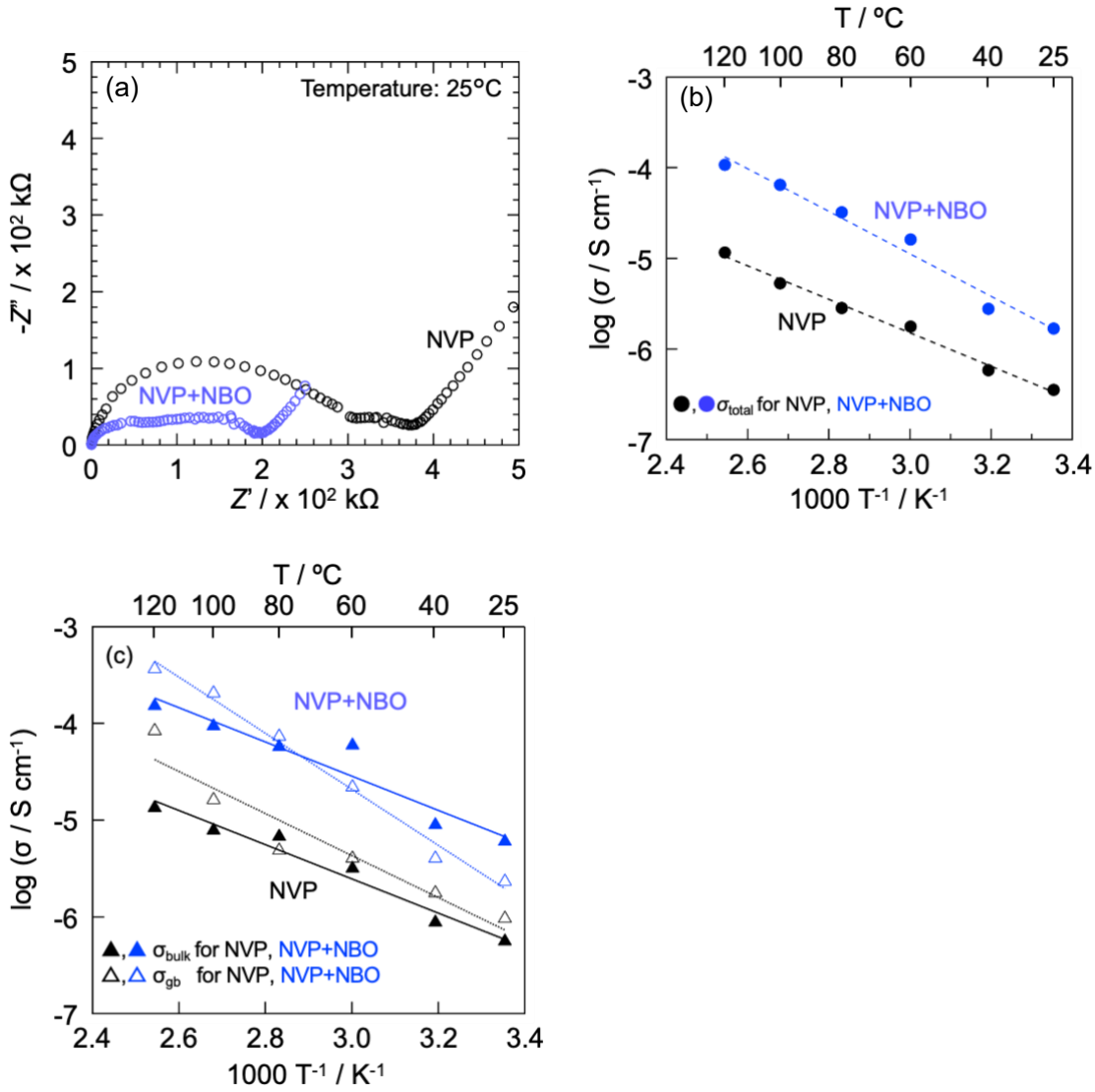

Figure 4-5 (a) Nyquist plots measured at 25 °C, (b) Arrhenius plots of the total electrical conductivity (σ_{total}), and (c) Arrhenius plots of the bulk (σ_{bulk}) and grain boundary (σ_{gb}) electrical conductivity for the Pt/NVP/Pt and Pt/NVP+NBO/Pt cells.

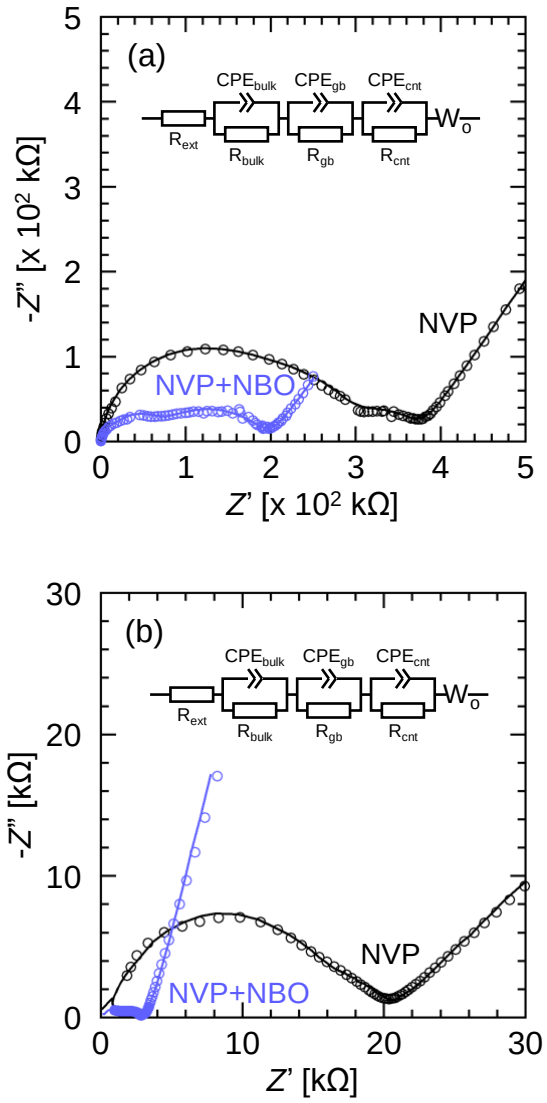

Figure 4-6 Nyquist plots (circle marker) and fitting results (solid line) at (a) 25 °C and (b) 100 °C for the Pt/NVP/Pt and Pt/NVP+NBO/Pt cells. R_{ext}, R_{bulk}, R_{gb}, R_{cnt} and CPE represent the external resistance, bulk resistance, grain boundary resistance, contact resistance and constant-phase element, respectively.

Table 4-1 Bulk, grain boundary and total electrical conductivity of the NVP and NVP+NBO (95:5) pellets (σ = electrical conductivity, gb = grain boundary).

	NVP@25 °C (S cm^{-1})	NVP+NBO@25 °C (S cm^{-1})	NVP@100 °C (S cm^{-1})	NVP+NBO@100 °C (S cm^{-1})	E_a (NVP) (eV)	E_a (NVP+NBO) (eV)
σ_{bulk}	5.6×10^{-7}	6.0×10^{-6}	7.9×10^{-6}	9.4×10^{-5}	0.37	0.37
σ_{gb}	9.6×10^{-7}	2.3×10^{-6}	1.6×10^{-5}	2.0×10^{-4}	0.34	0.60
σ_{total}	3.5×10^{-7}	1.7×10^{-6}	5.3×10^{-6}	6.5×10^{-5}	0.35	0.49

4.3.3. Charge and Discharge Properties

Figs. 4-7a and 4-7b shows charge/discharge curves and the cycling properties for the Pt/NVP/Pt and Pt/NVP+NBO/Pt cells as single-phase ASSBs. The charge capacity was regulated to 30 μAh to maintain a constant state of charge each time because the single-phase all-solid-state battery did not have a clear electrode area, and the progressing area of the *in-situ* formed electrode was varied in each experiment in the measurement by potential regulation. The average charge/discharge voltage at ca. 1.7 V was almost comparable to the NVP half-cell data, where the V^{3+}/V^{4+} and V^{2+}/V^{3+} redox reactions had plateaus at 3.4 and 1.7 V vs. Na/Na^+, respectively [17]. In addition, the overpotential was suppressed by the addition of NBO, which corresponds to the results of the impedance measurements, where the total resistance decreased and the potential loss due to the IR drop was reduced by the addition of NBO. The effect of NBO addition was also evident in the improvement of the charge-discharge cycle properties. The discharge capacity of the Pt/NVP/Pt cell rapidly decreased after the third cycle, while that of the Pt/NVP+NBO/Pt cell increased after each cycle. The increase in the discharge capacity of the Pt/NVP+NBO/Pt cell peaked around 23 μAh during charge/discharge cycling,

which could be due to hysteresis of the charge/discharge process in the NVP material. The cause of the increase in the reversible capacity of the Pt/NVP+NBO/Pt cell by cycling should be clarified in future research.

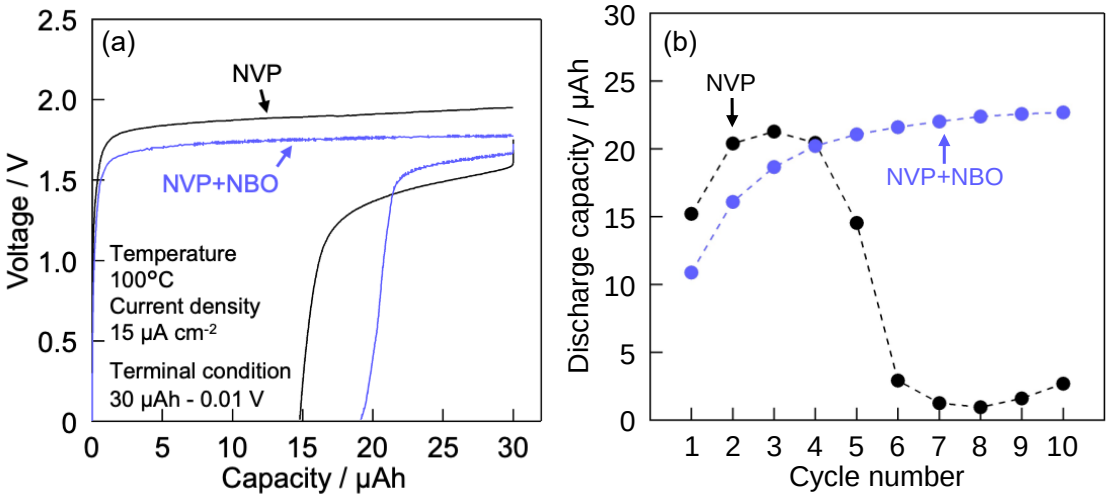

Figure 4-7 (a) Charge-discharge profiles and (b) cycling properties measured at 100 °C for the Pt/NVP/Pt and Pt/NVP+NBO/Pt cells as single-phase ASSBs.

4.3.4. Investigation of *in-situ* Formed Electrode

Figure 4-8a shows charge profiles of the Pt/NVP/Pt and Pt/NVP+NBO/Pt cells under a terminal charge voltage of 3 V. The Pt/NVP+NBO/Pt cell showed a larger charge capacity of 168 μAh than the Pt/NVP/Pt cell at 144 μAh. SEM images and EDS mapping images for the negative electrode side of a charged Pt/NVP/Pt pellet are shown in Figs. 4-8(b)–(d), and those for the surface of the initial pellet and the positive electrode side after charging are shown in Figs. 4-9a–f. Compared with the EDS maps, the dark areas in the SEM image of the negative electrode side indicate the presence of excess Na and little V, which suggests that Na^+ ions had migrated to a specific place on the negative electrode

side. On the other hand, no color change was observed on the positive electrode side, although a decrease in the amount of Na was observed in the central part of the positive electrode side. Therefore, I focused on the color change of the negative electrode side to compare the *in-situ* formed electrode between NVP and NVP+NBO.

Figs. 4-8e and 4-8f show optical micrographs of the surface of the negative electrode side of the Pt/NVP/Pt and Pt/NVP+NBO/Pt pellets after charging under a terminal charge voltage of 3 V. For the initial Pt/NVP/Pt pellet, the surface was a bright green color, as shown in Fig. 4-10, while the area appeared black after the charging process. Moreover, the Pt/NVP+NBO/Pt pellet showed larger and more dense black areas. The black areas in the optical microscopy images corresponded with the dark areas in the SEM image, which indicated that these were regions with large distributions of Na. The results were different after polishing away the surface of the negative electrode side for the Pt/NVP/Pt and Pt/NVP+NBO/Pt cells. For the Pt/NVP/Pt cell, a 112 μm thick layer was removed until the dark color area disappeared. On the other hand, for the Pt/NVP+NBO/Pt cell, only a 20 μm thick layer was removed until the dark colored area disappeared. Therefore, the Pt/NVP/Pt cell formed a deep *in-situ* electrode over a small area, while the Pt/NVP+NBO/Pt cell formed a shallow depth *in-situ* electrode over a wide area which led to larger charging capacity. This phenomenon may be due to the many voids in the NVP pellet, so that the current passes through only a limited area, which results in the formation of a narrow and deep area electrode, and a low charge capacity, whereas the NVP+NBO pellet has a high degree of densification and the current is applied evenly over a wider area. This resulted in the higher charge capacity of the Pt/NVP+NBO/Pt cell than that of the Pt/NVP/Pt cell due to the densification even though the NBO addition might slightly reduce the electronic conductivity which decided how the maximum capacity was.

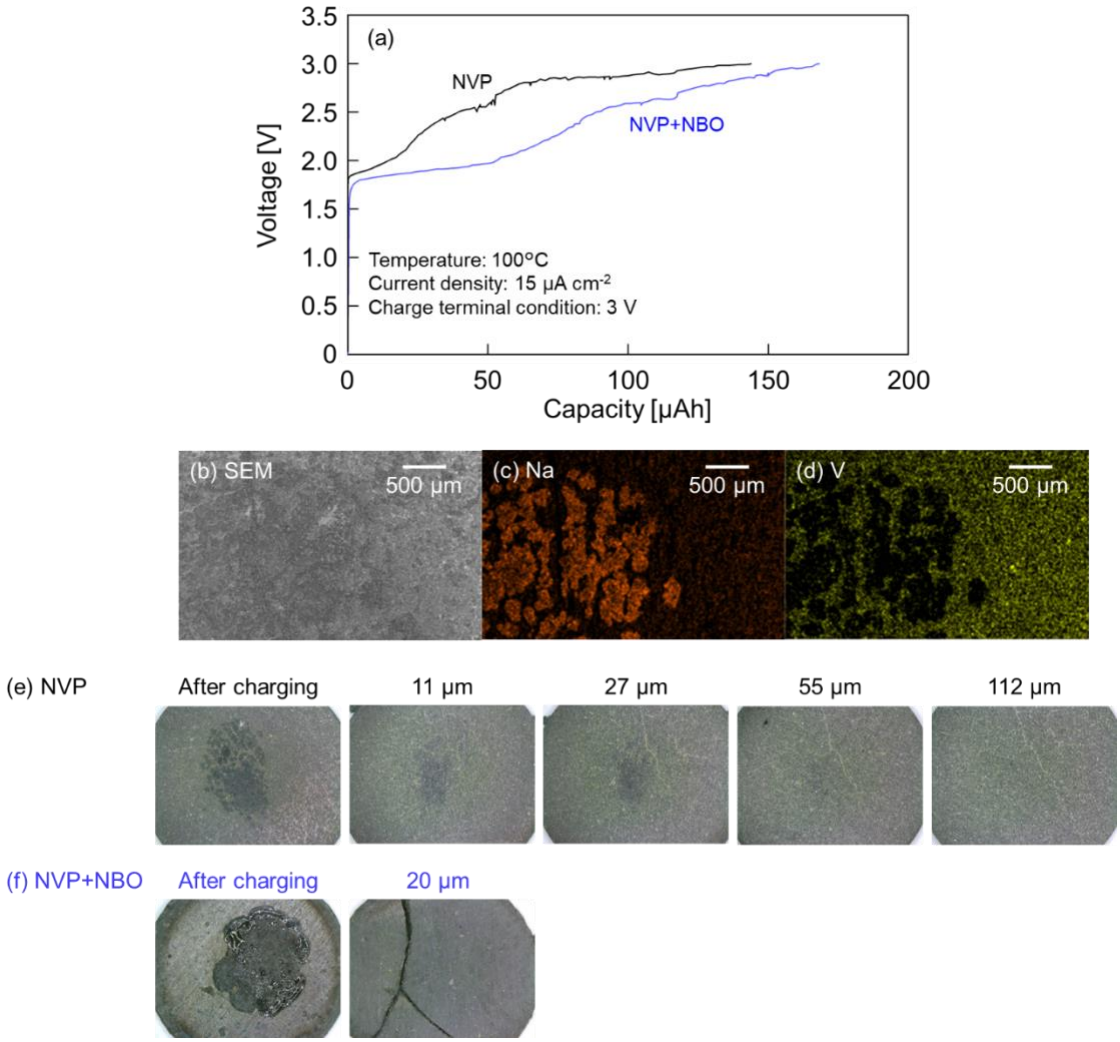

Figure 4-8 (a) Charge profiles for the Pt/NVP/Pt and Pt/NVP+NBO/Pt cells under a terminal charge voltage of 3 V at 100 °C. (b) SEM micrograph and EDS maps for (c) Na and (d) V on the Pt/NVP/Pt pellet. Optical micrographs of the surface on the negative electrode side of the (e) Pt/NVP/Pt and (f) Pt/NVP+NBO/Pt pellets after the charge process at a terminal voltage of 3 V at arbitrary thicknesses by polishing with sandpaper until the surface of the pellets showed no color-change areas.

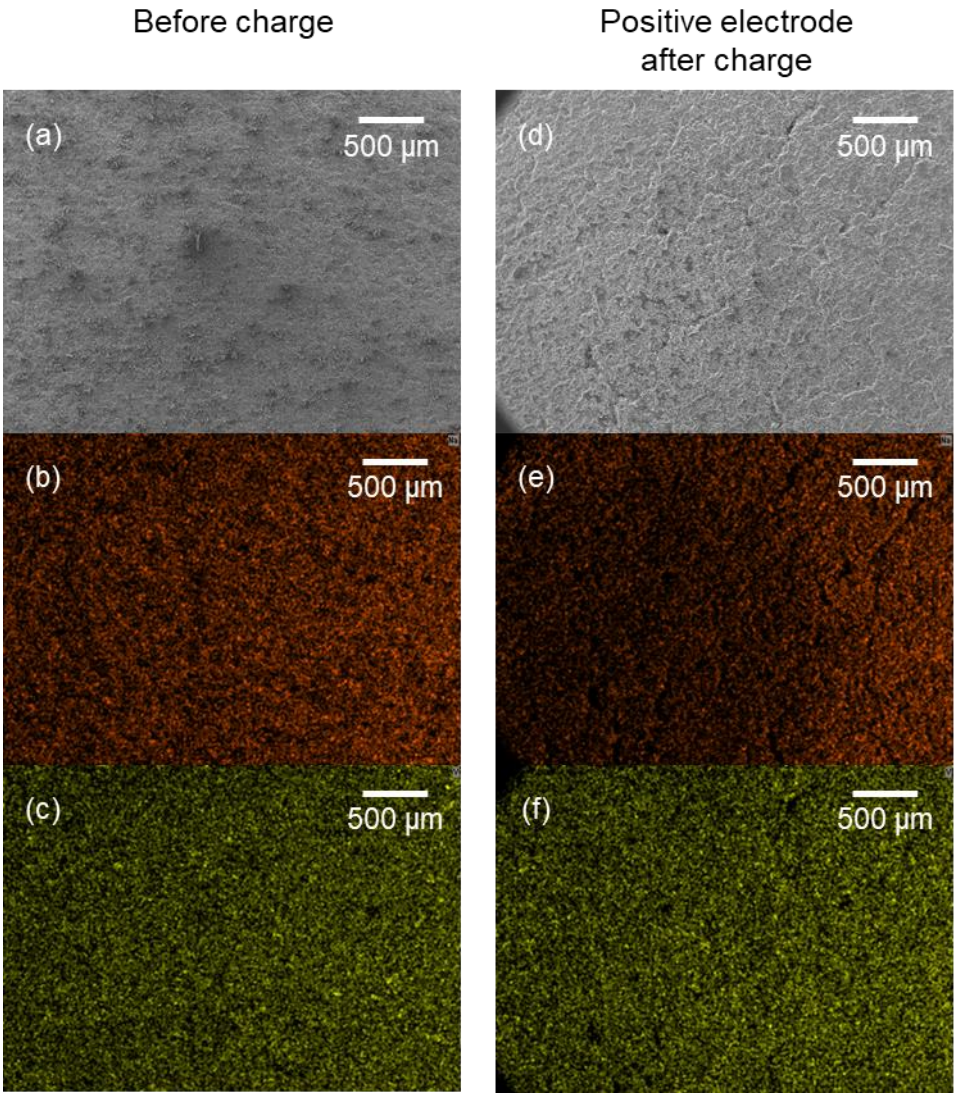

Figure 4-9 SEM micrographs and EDS maps for the surface of (a)-(c) the NVP pellet before charging and (d)-(f) the positive electrode side of the Pt/NVP/Pt cell after charging. (b) and (e) show the Na distribution, while (c) and (f) show the V distribution.

Figure 4-10 Optical image of the initial state of the Pt/NVP/Pt cell.

4.4. Conclusions

The addition of NBO to NVP was effective for improving the battery properties of a single-phase all-solid-state NIB. NVP and NBO powder were successfully synthesized and the optimal amount of NBO addition to NVP was determined to be 5 %. The voids in the NVP sintered body were filled by NBO powder according to SEM observations, which increased the relative density of NVP+NBO pellets compared to the NVP pellets. The NVP+NBO (90:10) pellets had the highest relative density; however, the NVP+NBO (95:5) pellets exhibited the highest electrical conductivity of 8.5×10^{-5} S cm^{-1}. On the other hand, the activation energy for the total and grain boundary was increased due to the low ionic conductivity of NBO and the generation of the grain boundaries between NVP and NBO. The Pt/NVP+NBO/Pt cell exhibited excellent cyclability compared to the Pt/NVP/Pt cell, although the charge/discharge profiles showed a lower reversible capacity at the first cycle for NVP+NBO. The 3 V terminal charge voltage measurements revealed that the Pt/NVP+NBO/Pt cell showed larger capacity than the Pt/NVP/Pt cell, and excess Na^+ was observed at the surface of the negative electrode side of the cells after 3 V charging. The *in-situ* formation of the electrodes differed depending on the porosity of the pellets; it suggested that electrochemical reactions occur in more narrow and deep regions when the porosity is high, and in more wide and shallow depth regions when the porosity is low and the pellets are dense which the current is applied uniformly and the capacity gets larger.

References

[1] M. Tatsumisago, M. Nagao, A. Hayashi, *J. Asian Ceram. Soc.* **1** (2013) 17–25.

[2] K. Takada, *J. Power Sources*. **394** (2018) 74–85.

[3] M. Shoji, E.J. Cheng, T. Kimura, K. Kanamura, *J. Phys. D. Appl. Phys.* **52** (2019) 103001.

[4] J.B. Goodenough, H.Y.P. Hong, J.A. Kafalas, *Mater. Res. Bull.* **11** (1976) 203–220.

[5] C. Masquelier, L. Croguennec, *Chem. Rev.* **113** (2013) 6552–6591.

[6] X. Lu, G. Xia, J.P. Lemmon, Z. Yang, *J. Power Sources*. **195** (2010) 2431–2442.

[7] K. Takada, *Langmuir*. **29** (2013) 7538–7541.

[8] F. Han, T. Gao, Y. Zhu, K.J. Gaskell, C. Wang, *Adv. Mater.* **27** (2015) 3473–3483.

[9] A. Inoishi, T. Omuta, E. Kobayashi, A. Kitajou, S. Okada, *Adv. Mater. Interfaces*. **4** (2017) 3–7.

[10] A. Inoishi, T. Omuta, Y. Yoshioka, E. Kobayashi, A. Kitajou, S. Okada, *ChemistrySelect*. **2** (2017) 7925–7929.

[11] A. Inoishi, A. Nishio, Y. Yoshioka, A. Kitajou, S. Okada, *Chem. Commun.* **54** (2018) 3178–3181.

[12] A. Inoishi, A. Nishio, A. Kitajou, S. Okada, *ChemistrySelect*. **3** (2018) 9965–9968.

[13] C. Yada, Y. Iriyama, T. Abe, K. Kikuchi, Z. Ogumi, *J. Electrochem. Soc.* **153** (2006) A1148.

[14] Y. Iriyama, C. Yada, T. Abe, Z. Ogumi, K. Kikuchi, *Electrochem. Commun.* **8** (2006) 1287–1291.

[15] T. Yamamoto, Y. Sugiura, H. Iwasaki, M. Motoyama, Y. Iriyama, *Solid State Ionics*. **337** (2019) 19–23.

[16] A. Nishio, A. Inoishi, A. Kitajou, S. Okada, *J. Ceram. Soc. Japan*. **127** (2019) 18–21.

[17] Y. Uebou, T. Kiyabu, S. Okada, J. Yamaki, *Reports Inst. Adv. Mater. Study, Kyushu Univ.* **16** (2002) 1–5.

Chapter 5

An Eldfellite-type Cathode Material, $NaV(SO_4)_2$, for Na-ion Batteries

5.1. Introduction

So far, the following sulphates with Fe^{2+}/Fe^{3+} redox couple have been reported as cathode active materials for Na-ion batteries; $Na_2Fe_2(SO_4)_3$ (3.8 V (vs. Na/Na^+)) [1], $Na_2Fe(SO_4)_2$ (3.6 V) [2], $NaFeSO_4F$ (3.5 V) [3,4], $NaFe(SO_4)_2$ (3.3 V) [5], $Na_2Fe(SO_4)_2 \cdot 2H_2O$ (3.25 V) [6], $Fe_2(SO_4)_3$ (3.2 V) [7,8], and $NaF–FeSO_4$ (3.0 V) [9]. Although there are some variations in the potential, it is noteworthy that sulphates show higher potential of about 1 V than phosphates such as $Na_3Fe_2(PO_4)_3$ (2.5 V) [10–12]. On the other hand, the disadvantage of the polyanionic cathode is that the theoretical capacity is limited by the heavy molecular weight. In particular, the eldfellite-type $NaFe(SO_4)_2$ (theoretical capacity: 99 mAh g^{-1}), which contains a large amount of polyanions relative to Fe, has a theoretical capacity 25% smaller than the NASICON-type $Na_2Fe_2(SO_4)_3$ (theoretical capacity: 134 mAh g^{-1}). However, this disadvantage of eldfellite can be reversed by replacing Fe with V, which is capable of not only M^{2+}/M^{3+} but also M^{3+}/M^{4+} redox. This is because the eldfellite-type $Na_xV(SO_4)_2$ has a theoretical capacity of 201

mAh g^{-1} in the composition range of $0 < x < 2$, while the NASICO-type $Na_xV_2(SO_4)_3$ has only a theoretical capacity of 137 mAh g^{-1} in the composition range of $0 < x < 2$.

For $NaV(SO_4)_2$, crystallographic studies and simple synthesis methods have already been reported [13–15]. High potentials of 2.42 and 4.61 V against Na/Na^+ have been predicted for the V^{2+}/V^{3+} and V^{3+}/V^{4+} redoxes by DFT calculations by Banerjee *et al* [16]. However, to the best of our knowledge, no experimental studies on the electrochemical properties of $NaV(SO_4)_2$ have yet been reported.

In the present study, eldfellite-type $NaV(SO_4)_2$ was synthesized by sol-gel method and the reversible capacity exceeding one electron reaction was confirmed in a wide voltage range between 1.5 and 4.8 V. The charge–discharge reaction mechanism was clarified through various *ex-situ* measurements using X-rays in a laboratory or a synchrotron light facility, and these results were confirmed by computational calculations.

5.2. Experimental

5.2.1. Materials Synthesis

$NaV(SO_4)_2$ powder was synthesized by referring to the reported method [15]. $H_2C_2O_4 \cdot 2H_2O$ (FUJIFILM Wako; min 99.5–102.0%) and V_2O_5 (Nacalai Tesque; min 99.0%) were mixed and agitated in ultrapure water at 80 °C for 1 h on a hotplate stirrer. The solution was initially orange and changed to green and then blue, indicating that V was reduced from the pentavalent to the tetravalent state. $(NH_4)_2SO_4$ (FUJIFILM Wako; min 99.5%) and Na_2SO_4 (FUJIFILM Wako; min 99.0%) were then added, and the resultant aqueous solution was continuously stirred at 80 °C for 4 h. The solution was evaporated to dryness in an electric furnace at 120 °C for 12 h, resulting in a precursor powder. Finally, 0.8 g of the precursor powder was placed in an alumina crucible and heated in a tubular furnace at 375 °C (0.5 °C min^{-1} heating rate) for 9 h under flowing Ar + 5% H_2 gas. Each reaction process in this synthesis, as previously reported [15], is shown below (5-1, 5-2):

$$V_2O_5 + 3H_2C_2O_4 \cdot 2H_2O \rightarrow 2VOC_2O_4 + 9H_2O + 2CO_2 \quad (5\text{-}1)$$

$$2VOC_2O_4 + Na_2SO_4 + 3(NH_4)_2SO_4 \rightarrow 2NaV(SO_4)_2 + 6NH_3 + 3H_2O + 3CO_2 + CO \quad (5\text{-}2)$$

5.2.2. Materials Characterization

Powder XRD profiles of $NaV(SO_4)_2$ were recorded to identify its crystal structure at room temperature. The profiles were obtained using an X-ray diffractometer

(TTRIII; Rigaku) equipped with a Cu Kα radiation source. The samples were measured in steps of 0.01° in the 2θ angular range from 10° to 130° at a scan rate of 0.1° min^{-1}. An enclosed sample holder was used to exclude the effects of moisture in the air. The crystal structure was refined using the RIETAN-FP program [17], and the crystal models were visualized using the VESTA software [18]. The sample morphology was observed by field-emission scanning electron microscopy (FE-SEM, JSM-IT700HR; JEOL).

5.2.3. Electrochemical Characterization

$NaV(SO_4)_2$ and acetylene black (AB, Denka) were mixed in a ratio of 70:25 (by weight) using the ball-milling method (Premium line P-7; Fritsch) at 200 rpm for 3 h under an Ar atmosphere to increase the electronic conductivity of the electrode. The cathode was then prepared by blending the composite with PTFE (Daikin) binder in a ratio of 95:5 (by weight) and then drying the electrode material at 80 °C under vacuum for 12 h. For electrochemical measurements, 2032 coin-type cells (Hohsen Co.) were washed ultrasonically with acetone and dried at 120 °C under vacuum before being transferred to a glove box for cell assembly. Na metal (Sigma-Aldrich) was used as the counter and reference electrode. A polypropylene separator (Celgard) and a glass-fiber filter (GA-55; Advantec) were used as a separator in the cell. A 1 M $NaPF_6$ solution in EC:DEC (1:1 by volume) (Tomiyama Pure Chemical) or a 1 M $NaClO_4$ solution in EC:DMC (1:1 by volume) (Tomiyama Pure Chemical) was used as the electrolyte. All cathodes and cells were produced and assembled in an Ar-filled glove box (dew point < −80 °C). Electrochemical charge–discharge measurements were conducted via the galvanostatic method using a charge–discharge cycle instrument (BTS2400W; Nagano

Electric Co.). The current density was 0.2 mA cm^{-2}, and the galvanostatic measurements were conducted in a thermostated chamber at 25 °C.

5.2.4. *ex-situ* X-ray Measurement

ex-situ XRD measurements were performed to characterize the phase transitions during the charge–discharge processes. The XRD patterns were recorded at room temperature using an X-ray diffractometer (TTRIII; Rigaku) equipped with a Cu Kα radiation source. The measurements were performed in steps of 0.01° in the 2θ angular range from 10° to 40° at a scan rate of 0.02° min^{-1}. The samples were obtained from coin cells disassembled in an Ar-filled glove box (dew point < −80 °C) after the electrochemical measurements and were dried under vacuum after being washed with DMC (Kishida Chemical) to remove the electrolyte on the pellet surface. An enclosed sample holder was used to exclude the effects of moisture in the air.

ex-situ XPS measurements were conducted with Al Kα radiation using an ESCA 1600 (ULVAC-PHI) spectrometer. The samples were prepared in the same manner as those for *ex-situ* XRD analysis. The obtained binding-energy data were corrected using the signal of adventitious carbon added to prevent charging up of the sample.

ex-situ X-ray absorption near-edge structure (XANES) measurements and *ex-situ* near-edge X-ray absorption fine structure (NEXAFS) measurements were performed at the BL11 beamline (2100–23000 eV), BL12 beamline (40–1500 eV), and BL15 (3500–23000 eV) of the Saga Light Source. Synchrotron radiation was used in the transmission mode (TM) for XANES measurements and total fluorescence yield (TFY) mode for NEXAFS measurements at room temperature to determine the oxidation state of V during

the charging and discharging processes. Samples were prepared using the same procedure described for the XPS samples, including washing with DMC. XANES data analysis was performed using the Athena software [19].

For the XPS and NEXAFS measurements, a sample transfer vessel was used to avoid exposure to the air and to achieve a high-vacuum condition before the sample was introduced into the apparatus [20,21].

5.2.5. Computational Calculation

First principle calculations using DFT were performed with the Vienna *Ab-initio* Simulation Package (VASP) [22,23]. The projector augmented wave (PAW) method was used [24,25], and the plane-wave cutoff energy was set to 520 eV. The Perdew–Burke–Ernzerhof (PBE) exchange-correlation functional was applied [26]. The Hubbard U value for vanadium was set to 4.0 eV. The pymatgen package in Python was used for all DFT calculations to generate input files and analyze the results [27]. A unit cell (*C*2/*m*) was used for the calculations, and a Γ-centered 4 × 4 × 4 k-point mesh was employed for the density of state (DOS) and electronic structure calculations. The 30 structures with the lowest electrostatic energies for each composition were subjected to the DFT calculations using the supercell program [28], and the most stable configuration was determined. The average voltage between each composition of $Na_xV(SO_4)_2$ was obtained using bellow equation (5-3);

$$V = -\frac{E(\mathrm{Na_{x_1}V(SO_4)_2}) - E(\mathrm{Na_{x_2}V(SO_4)_2}) - (x_1 - x_2)E(\mathrm{Na})}{(x_1 - x_2)F} \quad (5\text{-}3)$$

where $E(Na_{x1}V(SO_4)_2)$, $E(Na_{x2}V(SO_4)_2)$ and $E(Na)$ are DFT energies of $Na_{x1}V(SO_4)_2$, $Na_{x2}V(SO_4)_2$ and Na metal, respectively. Bader charge analysis was conducted based on the calculation results of DOS using the Bader analysis program developed by Henkelman *et al* [29−31].

5.3. Results & Discussion

5.3.1. Computational Calculations for $Na_xV(SO_4)_2$

The structural optimization was conducted to evaluate the characteristics of $NaV(SO_4)_2$ for each sodiated/desodiated composition. The first state formed a stable eldfellite structure with a monoclinic prismatic crystal class. Figure 5-1a shows the formation energy convex hull construction of $Na_xV(SO_4)_2$. The formation energy of the composition x = 1.5 is above the convex hull line, which means this composition is unstable. Therefore, the compositions of x = 0, 0.5, 1, and 2 in $Na_xV(SO_4)_2$ were adopted for further calculations and analyses. Figure 5-1b presents the DFT-calculated average potential profiles of $Na_xV(SO_4)_2$ (x = 0, 0.5, 1, 2). Two potential plateaus are identified at ~2.2 and ~4.6 V, with two more-detailed potential plateaus at the higher potential of ~4.6 V. Starting from the initial state of $NaV(SO_4)_2$, the theoretical capacity was estimated to be 101 mAh g^{-1} for a one-electron reaction and 202 mAh g^{-1} for a two-electron reaction. The results of the potential calculations show good agreement with previously reported results [16]. For the desodiation from $NaV(SO_4)_2$, we expected operation at a high potential such as ~4.7 V vs. Na/Na^+ using common electrolytes to be feasible because some materials have been reported to operate at higher potentials [32−34].

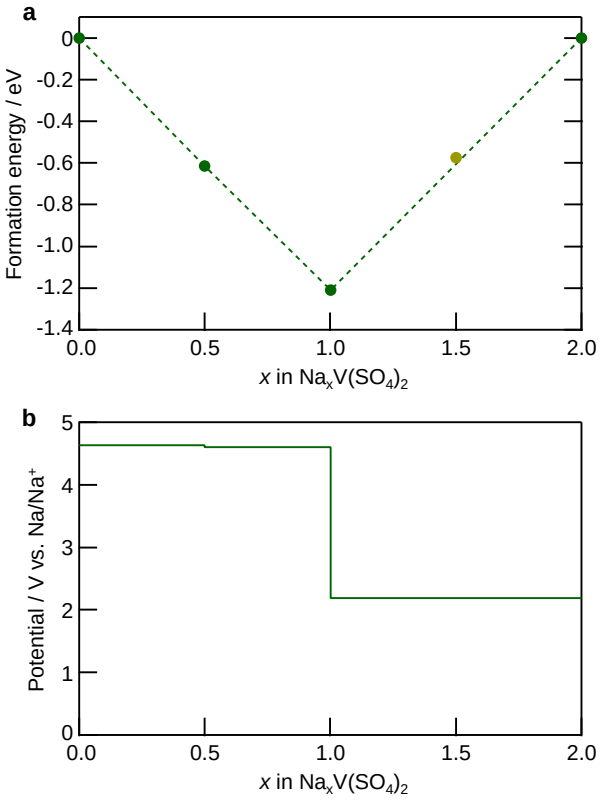

Figure 5-1 (a) Formation energy convex hull construction and (b) potential profile for each content of $Na_xV(SO_4)_2$.

5.3.2. Materials Characterisation

$NaV(SO_4)_2$ was synthesized using the previously reported sol–gel method. We optimized the sintering time and temperature at 9 h and 375 °C by attempting several sinter time/temperature combinations, although some small unknown impurities remained. The crystal structure of the synthesized $NaV(SO_4)_2$ was determined by powder XRD via Rietveld refinement using RIETAN-FP [17] (Fig. 5-2a). The results revealed that the compounds could be indexed to a monoclinic lattice of space group *C*2/*m* and

that the lattice parameters were a = 8.09(1), b = 5.180(6), c = 7.185(9), β = 92.067(7)°, and V = 300.9(6) Å^3, which is larger than the unit-cell volume of $NaFe(SO_4)_2$ [5] because of the larger ionic radius of V^{3+} (0.640 Å) compared with that of Fe^{3+} (0.61 Å) in a hexagonal system. These parameters are consistent with the previous research on the synthesis of $NaV(SO_4)_2$ [15]. The Rietveld-refined parameters were satisfactory, with R_{wp} = 6.16%, R_p = 4.63%, and S = 1.29. However, ~3 wt% of $V_2O_3(SO_4)_2$ was confirmed as a sub-phase material; this material has been reported to be lithiated between 1.95 and 4.20 V [35]. The crystal structure was obtained from the Rietveld refinement results (Fig. 5-2b). Na ions were connected to the VO_6 octahedra and SO_4 tetrahedra via six surrounding oxygen atoms. The morphologies of the as-prepared $NaV(SO_4)_2$ powder were confirmed by SEM observation (Fig. 5-2c and 5-2d). The powder exhibited moisture-absorbent character; the samples were therefore carefully transported to the measuring equipment without exposure to moisture in the air. The particle shape and grain size were dramatically changed and refined by ball milling.

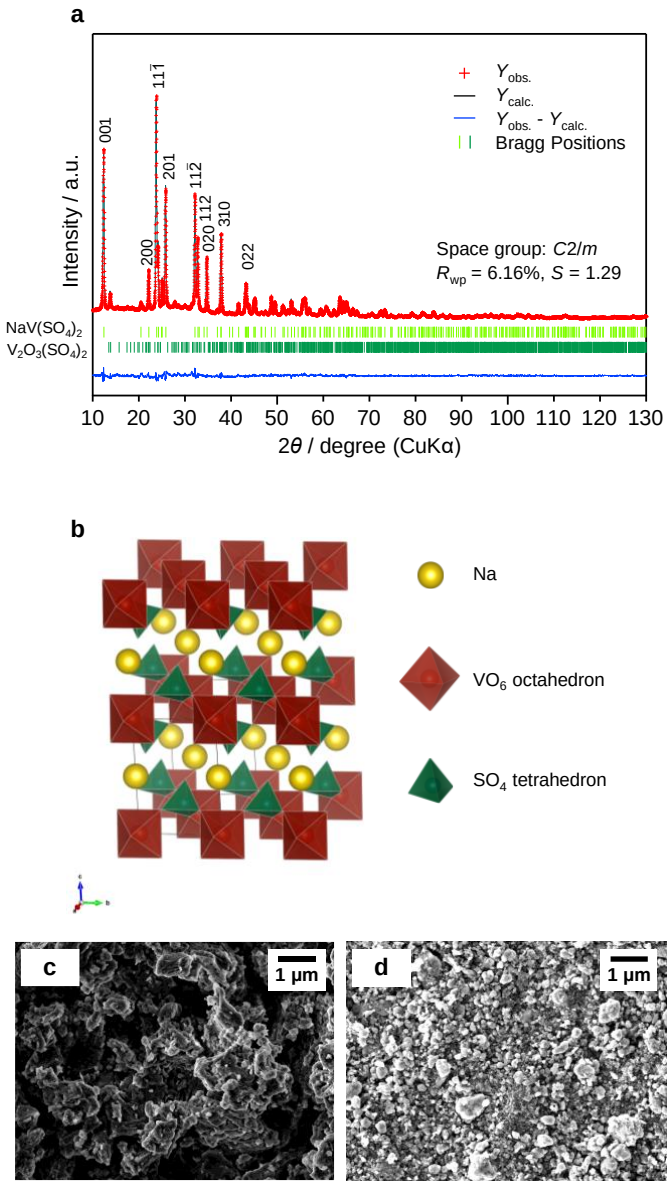

Figure 5-2 (a) XRD pattern and the results of Rietveld refinement of as-prepared $NaV(SO_4)_2$; (b) the crystal structure obtained from the Rietveld-refined $NaV(SO_4)_2$. The structure was visualized using VESTA. SEM images of (c) as-prepared $NaV(SO_4)_2$ and (d) carbon-coated $NaV(SO_4)_2$ by ball milling.

Table 5-1 Crystallographic parameters of as-synthesized $NaV(SO_4)_2$ obtained from Rietveld refinement using RIETAN-FP program [17].

Chemical formula	$NaV(SO_4)_2$
Formula weight	266.056
Crystal system, space group	Monoclinic, *C*2/*m*
Temperature	~ 298 K (ambient)
a, *b*, *c* / Å	8.0289(16), 5.16063(10), 7.1370 (17)
α, *β*, *γ* / Å	90, 91.870(12), 90
V / Å^3	295.56(11)
Z	2
Calculated density / g cm^{-3}	2.989
R_{wp}	6.16%
R_p	4.63%
R_e	4.76%
R_B	2.80%
R_F	1.58%
S	1.29
Goodness of fit	1.68
Radiation	CuKα

Atom	Wyckoff site	*x*	*y*	*z*	occ.	B_{iso} / Å^2
Na1	2c	0	0	1/2	1	2.03(6)
V1	2a	0	0	0	1	0.41(2)
S1	4i	0.3619(15)	0	0.2211(15)	1	1.06(3)
O1	4i	0.2351(3)	0	0.0605(3)	1	1.28(3)
O2	4i	0.2884(3)	0	0.4066(3)	1	1.28(3)
O3	8j	0.4686(18)	0.2343(3)	0.2005(19)	1	1.28(3)

5.3.3. Electrochemical Properties

The galvanostatic properties of the composite electrode, including $NaV(SO_4)_2$ as the active material, are presented in Fig. 5-3. The composite electrode consisted of $NaV(SO_4)_2$, AB (as an electronic conductor), and PTFE (as a binder) in a weight ratio of 70:25:5. The measurement voltage range was regulated to 1.5–3.2 V (vs. Na/Na^+) for the sodiation/desodiation process ($1 \leq x \leq 2$ in $Na_xV(SO_4)_2$) from the initial state of $NaV(SO_4)_2$ and to 3.3–4.8 V with a theoretical capacity limitation of 101 mAh g^{-1} for the desodiation/sodiation process ($0 \leq x \leq 1$ in $Na_xV(SO_4)_2$). The current density was 0.2 mA cm^{-2}, and the galvanostatic measurements were conducted in a thermostated chamber at 25 °C. In this electrochemical research, two electrolytes were employed: 1 M $NaPF_6$ in EC:DEC (1:1 by volume) and 1 M $NaClO_4$ in EC:DMC (1:1 by volume). For the sodiation/desodiation process in Fig. 5-3a, a potential plateau was observed at 2.3 V (vs. Na/Na^+). From the reversible capacity and potential values, the average working potential was calculated to be 2.1 V, which is consistent with the average potential calculated by DFT. This value is the highest potential reported for the V^{2+}/V^{3+} redox couple in any material because of the greater inductive effect of SO_4^{2-} compared with that of other counter anions. The reversible capacity in the first cycle was 77 mAh g^{-1}, which is greater than 75% of the theoretical capacity. After the second cycle, $NaV(SO_4)_2$ showed good cyclability, with better than 95% coulombic efficiency, and the capacity retention was 60% at the 30th cycle. The discharge–charge capacities of $NaV(SO_4)_2$ are comparable to those of $NaFe(SO_4)_2$ (Fe^{2+}/Fe^{3+}) [5]. The potential difference of 1 V between $NaV(SO_4)_2$ and $NaFe(SO_4)_2$ was reasonably attributed to the typical potential gap between V^{2+}/V^{3+} and Fe^{2+}/Fe^{3+}, similar to the difference observed between the NASICON-type materials $Na_3V_2(PO_4)_3$ (1.5 or 1.6 V) and $Na_3Fe_2(PO_4)_3$ (2.5 V) [10−12,36−38].

Different electrolyte types did not affect the discharge–charge properties in the sodiation/desodiation process from the initial state of $NaV(SO_4)_2$, as compared in Fig. 5-3a and 5-3c. However, in terms of the desodiation/sodiation process from the initial composition, different electrolyte types resulted in different galvanostatic charge–discharge profiles. For the $NaPF_6$-type electrolyte, the potential of the $NaV(SO_4)_2$ cell decreased and remained ~3.7 V; in addition, the cell charged beyond its theoretical capacity based on the one-electron reaction in $NaV(SO_4)_2$ after reaching 4.1 V at a charging capacity of 19 mAh g^{-1} (Fig. 5-4). By contrast, for the $NaClO_4$-based electrolyte, no potential decrease was observed even after the highest potential was reached in the charging process. These charging profiles likely indicate electrolyte decomposition even though the literature includes few examples of redox reactions that operate at equal or higher potentials than those in the present study [32,33]. Therefore, the capacity was regulated at 101 mAh g^{-1} for this process to force this decomposition reaction to stop at the one-electron theoretical capacity of $NaV(SO_4)_2$. Fig. 5-3b and 5-3d shows the charge–discharge profiles for the two electrolytes. Similar profiles to those in the aforementioned data (Fig. 5-4) were observed when cells were charged to high potentials, whereas differences were detected between the two electrolytes with respect to the reversible capacity. A small reversible capacity of 2 mAh g^{-1} was observed in the cell with 1 M $NaPF_6$ in EC:DEC (1:1 by volume), whereas a reversible capacity of 25 mAh g^{-1} was obtained with an average working potential of 3.9 V in the cell with 1 M $NaClO_4$ in EC:DMC (1:1 by volume) at the first cycle. In the second cycle, the reversible capacity increased to 31 mAh g^{-1}, which is 30% of the one-electron theoretical capacity of $NaV(SO_4)_2$, and then gradually decreased from the third cycle. No difference was observed in these operations because of the solvent in the electrolyte (Fig. 5-5). Oxidative decomposition of the electrolyte is unavoidable in this material during charge–discharge

operations at high potential, resulting in lower capacities and working potentials than those calculated. $NaV(SO_4)_2$ was found to be reversibly charged and discharged, at least in the $NaClO_4$-based electrolyte. However, the longer the rest time after charging, the more the discharge capacity decreased (Fig. 5-6). Thus, even in the $NaClO_4$-based electrolyte, the progression of the side reactions or electrolyte decomposition caused by holding the electrolyte at high potential cannot be suppressed according to Fig. 5-5. If the oxidative decomposition of the electrolyte can be prevented at high voltages, the working potential and reversible capacity should increase further because the capacity corresponding to the sloped part of the charging curve coincides with that corresponding to the discharging curve.

A charge–discharge diagram corresponding to a broader potential range (1.5–4.8 V) is shown in Fig. 5-3e. The charging capacity was regulated to 101 mAh g^{-1} from the open-circuit potential at the first cycle; from the second cycle onward, the charging capacity was also regulated to 101 mAh g^{-1} after charging from 1.5 V to 3.2 V. Both the charge and discharge capacities exceeded 101 mAh g^{-1}, and the discharge capacity reached 102 mAh g^{-1} for the second cycle. As demonstrated in Fig. 5-3f, the decrease in charge capacity with each cycle mostly stopped at a certain level; however, the discharge capacity and coulombic efficiency decreased with each cycle, likely because of electrolysis of the electrolyte caused by repeated cycling at high potentials.

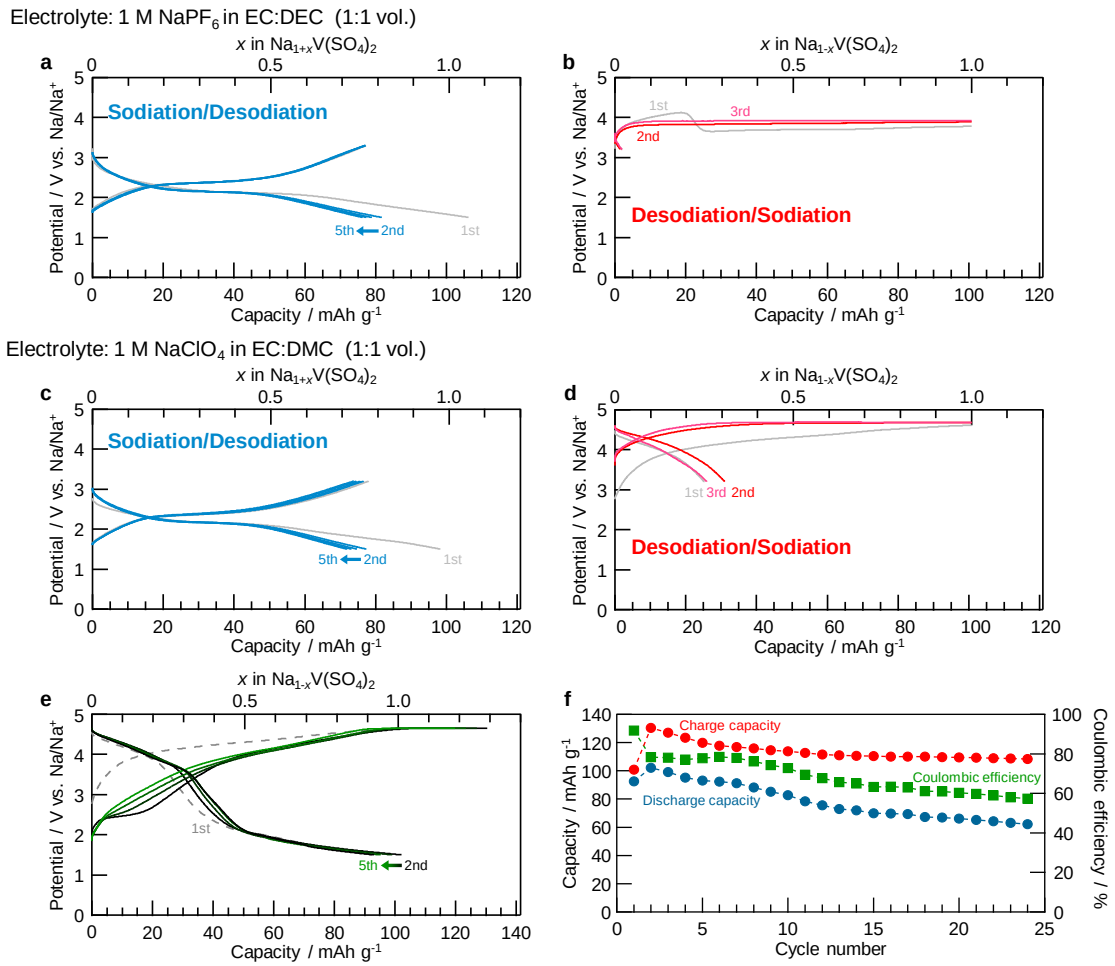

Figure 5-3 Charge/discharge profiles of $NaV(SO_4)_2$ from sodiation and desodiation with the two types of electrolyte; 1 M $NaPF_6$ in EC:DEC (1:1 vol.) (a) and (b), 1 M $NaClO_4$ in EC:DMC (1:1 vol.) (c) and (d), respectively. (e) Charge/discharge profiles and (f) cycle performances of $NaV(SO_4)_2$ in the voltage region of 1.5−4.8 V using 1 M $NaClO_4$ in EC:DMC (1:1 vol.).

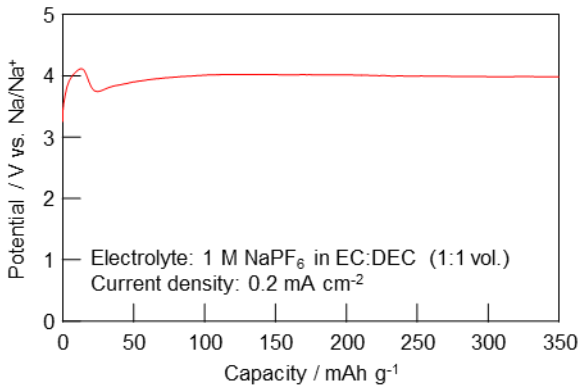

Figure 5-4 Charge curves of $NaV(SO_4)_2$ after charging (desodiation) toward to high potentials using 1 M $NaPF_6$ in EC:DEC (1:1 vol.) as the electrolyte at the first cycle.

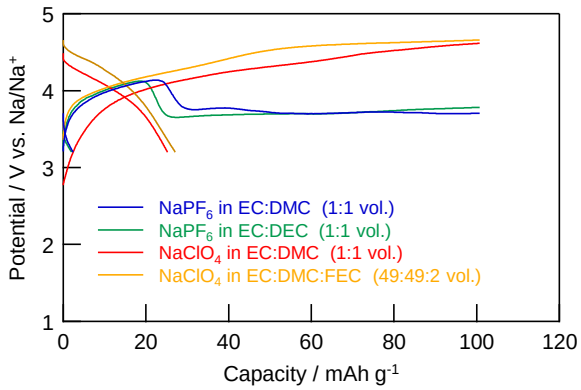

Figure 5-5 Charge/discharge curves of $NaV(SO_4)_2$ for the first cycle using the four different types of electrolytes. The charge capacity was regulated to 101 mAh g^{-1}, and the cutoff voltage and current density was set as 1.5–4.8V and 0.1 mA cm^{-2}.

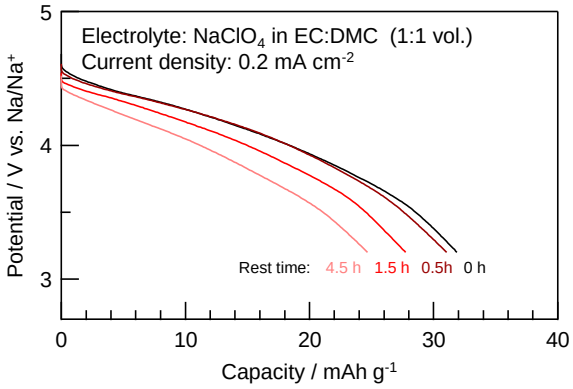

Figure 5-6 Discharge curves of $NaV(SO_4)_2$ after charging (desodiation) for 101 mAh g^{-1} toward to high potentials using 1 M $NaClO_4$ in EC:DMC (1:1 vol.) as the electrolyte at the first cycle. Rest time was varied from 0 h to 4.5 h.

5.3.4. Surface Analysis on the Composite Electrode

The electrode surface was investigated by *ex-situ* XPS to investigate what caused the decomposition or dissolution into the electrolyte and how different the degree of the decomposition was between the two electrolytes at high potential. The measured samples were prepared without any washing processes to remain the dissolved materials on the electrode surface. Figure 5-7 demonstrated the *ex-situ* XPS spectra during the charge/discharge process using two electrolyte types: 1 M $NaPF_6$ in EC : DEC (1 : 1 vol.) and 1 M $NaClO_4$ in EC : DMC (1 : 1 vol.). The states of charge during the sodiation/desodiation or desodiation/sodiation process were pointed out in Fig. 5-8. To verify the decompositions in the electrolyte, the spectra of consistent elements were investigated for F 1*s* and Cl 2*p*. The XPS spectra of F 1*s* and Cl 2*p* were not changed after 1.5 V discharging and 3.2 V charging for the sodiation/desodiation process, so the

decomposition of the electrolyte or solute had not happened for the two types of electrolytes at the low potential cycling. On the other hand, we found that $NaPF_6$ was dynamically decomposed, but $NaClO_4$ was not much at the high potential. In Fig. 5-9, the peak separations of F 1*s* spectra were shown for the initial state, after cycling the sodiation/desodiation and the desodiation process using 1 M $NaPF_6$ in EC : DEC (1 : 1 vol.) as the electrolyte. At the initial state, only the peaks for the bonding of P-F and C-F implied $NaPF_6$ and PTFE, which were the electrolyte solute and the binder in the composite electrode. At the end of the sodiation/desodiation process, the spectra resulting from Na-F bonding implied forming NaF were barely observed. In contrast, after the desodiation process at the high potential, the peak implying the generation of NaF intensively increased, which meant the part of $NaPF_6$ was decomposed to NaF; these results were also apparent in Fig. 5-9. The $NaPF_6$-type electrolyte was not favourable for the high-potential performance of $NaV(SO_4)_2$, although some reports about cathode materials including polyanionic compounds adopted $NaPF_6$-type electrolytes for the high-potential cycling [32−34,39]. In contrast, in the system using 1 M $NaClO_4$ in EC : DMC (1 : 1 vol.) as the electrolyte, the spectra of Cl 2*p* did not much change even at the high potential, and only the peak of Cl $2p_{1/2}$ increased during the desodiation/sodiation that was not likely to be concerned with any side reactions.

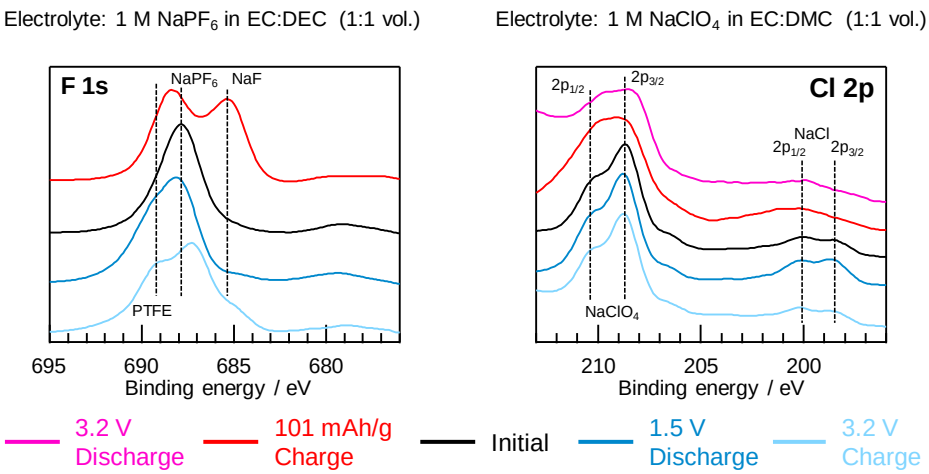

Figure 5-7 *ex-situ* XPS spectra of $NaV(SO_4)_2$ at the different charge/discharge states during the first cycle using two electrolyte types: 1 M $NaPF_6$ in EC:DEC (1:1 vol.) and 1 M $NaClO_4$ in EC:DMC (1:1 vol.). The measured samples were obtained from the disassembled coin cells without any washing processes.

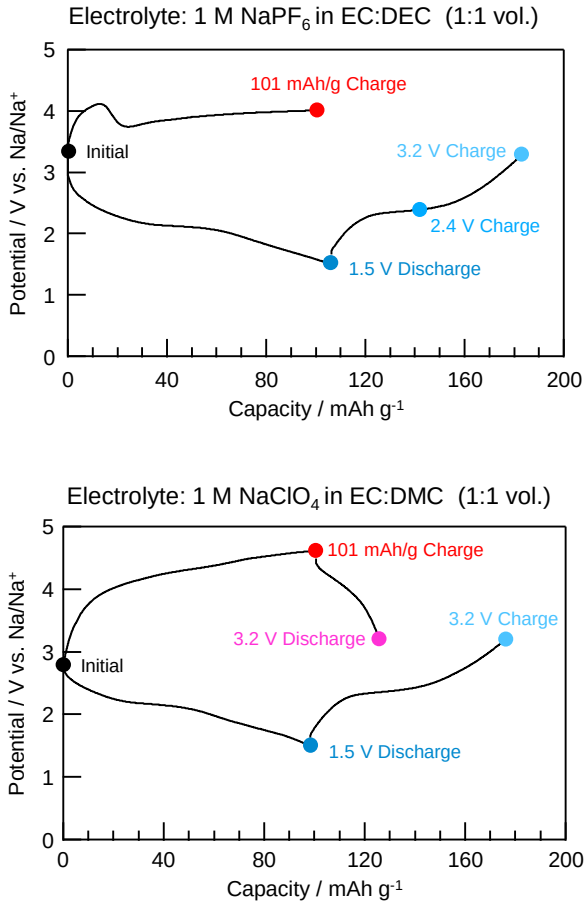

Figure 5-8 Charge/discharge curves of $NaV(SO_4)_2$ for the first cycles using two types of electrolytes during the sodiation/desodiation or desodiation/sodiation process and pointed out the state of charge by circle-colored dots.

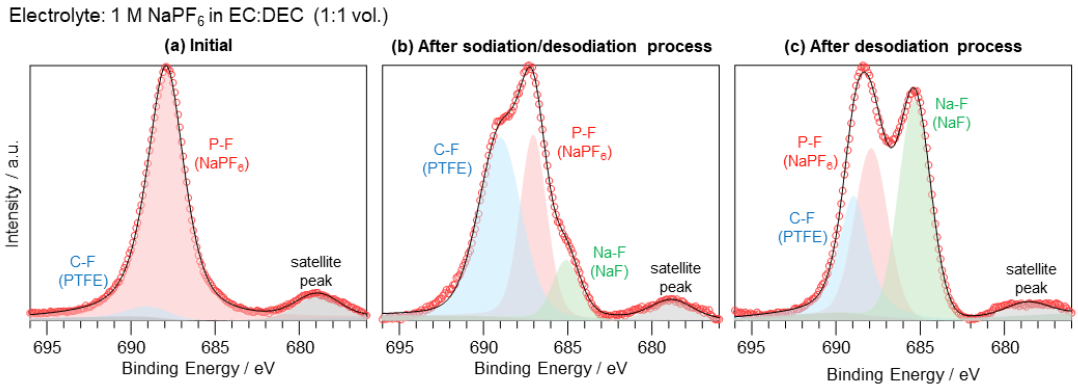

Figure 5-9 Peak separation results of ex-situ XPS spectra in the binding energies between 676 and 696 eV to identify F 1*s* state. The samples were removed from the coin cells

using 1 M $NaPF_6$ in EC:DEC (1:1 in vol.) as the electrolyte at each condition; (a) initial state, (b) after sodiation/desodiation process and (c) after desodiation process.

5.3.5. Crystal Structure Analysis

Figure 5-10 shows the *ex-situ* XRD patterns during the charge–discharge process for the first cycle. The states of charge during the sodiation/desodiation or desodiation/sodiation process are indicated in the charge–discharge profiles next to the XRD profiles. All of the patterns were applied without any corrections because Soller slits were installed for the parallel-beam method for the XRD measurements as a consequence of the peak of PTFE appearing at the same angle (18°) for all the samples. For the sodiation/desodiation process (blue and sky-blue lines), peak shifts to lower angles were observed from the initial state to the 1.5 V discharged stated, and the peaks were recovered to original position by 3.2 V charging at 12.3°, 23.7°, 25.8°, and 32.1°, which were assigned as the (001), (11$\bar{1}$), (201), and (11$\bar{2}$) Bragg peaks, respectively. The shift to smaller angles indicates that the insertion of Na^+ led to an increase in the lattice parameter. In addition, the peak intensity ratios for the peak groups at ~12°, ~25°, and ~32.5° were reversibly changed. Therefore, they tended to be comparable to the simulated XRD patterns visualized by VESTA[18] on the basis of the DFT calculations (Fig. 5-11). Moreover, two new peaks appeared at 22.6° and 34° (pointed out by filled stars), indicating a two-phase mechanism after discharge to 1.5 V; these peaks fully recovered after charging to 3.2 V.

Similarly, for the desodiation/sodiation process lined in red and pink, the intensity ratios between the peak groups of 12° and 25° were reversibly changed: the peak

group at ~12° increased after 101 mAh g^{-1} charging and then recovered to the initial state after discharge to 3.2 V. New peaks were also observed at ~27.5° and ~31.2° (pointed out by unfilled stars) after the desodiation by charging to 101 mAh g^{-1}; the intensities of these peaks then decreased upon sodiation by discharging to 3.2 V, but the initial patterns were not fully recovered. These results confirm that single-phase and two-phase reactions occur during both the sodiation/desodiation and desodiation/sodiation processes from the initial composition.

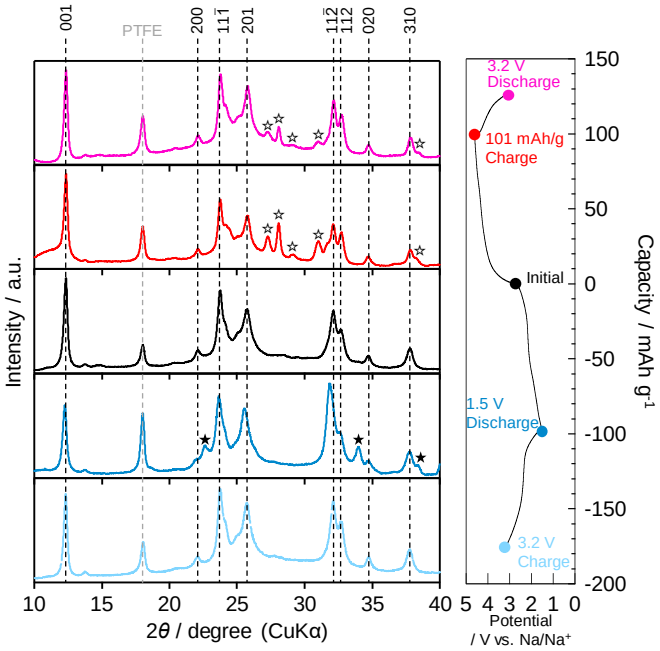

Figure 5-10 *ex-situ* XRD patterns during galvanostatic measurements using 1 M $NaClO_4$ in EC:DMC (1:1 by volume) as the electrolyte for the initial state (black line), the desodiation/sodiation process (red and pink lines), and sodiation/desodiation process (blue and light-blue lines). Black and white star icons show the new diffraction peaks on discharging and charging process, respectively.

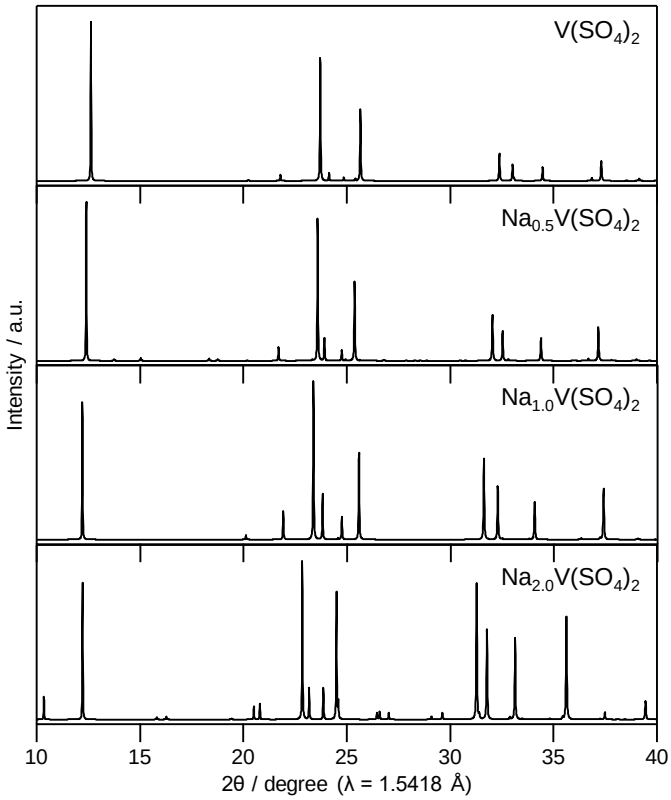

Figure 5-11 Calculated XRD patterns for each content of Na^+ for $Na_xV(SO_4)_2$. The stabilized crystal structures were obtained using the DFT calculation and the XRD patterns were exported using VESTA software[18] based on the DFT-calculated structure.

5.3.6. Oxidation State Analysis

Oxidation-state analysis was conducted to investigate the redox center of $NaV(SO_4)_2$ during the charge–discharge process by *ex-situ* XANES measurements using hard X-rays and *ex-situ* NEXAFS measurements using soft X-rays. All the samples used in the measurements were removed from disassembled cells and washed with dimethyl carbonate (DMC) more than 1 day after the respective charge–discharge measurements for the first cycle. Here, we used two different beamlines for soft (40–1500 eV) and hard

(2100–23,000 eV) X-rays to cover the targeted energy range. The V *K*-edge XANES spectra were obtained in the hard X-ray range to determine the oxidation state of V during the charge–discharge measurements (Fig. 5-12 and 5-12c). Each state of charge was found to match the charge–discharge profiles in Fig. 5-12a. In the sodiation/desodiation process from the initial state (Fig. 5-12b), the *K*-edge of V shifted to lower energy upon discharge to 1.5 V and shifted to higher energy and returned to the initial position upon charging to 3.2 V. These results indicate that a reversible V redox reaction occurred. Compared with the standard samples of vanadium oxides of VO (V^{2+}) and V_2O_3 (V^{3+}) in Fig. 5-13, the initial oxidation state of V^{3+} changes to V^{2+} upon sodiation and then returns to the original V^{3+} upon desodiation. However, during the desodiation/sodiation process from the initial state, the shift at the absorption edge was negligible (Fig. 5-12c). However, the second-derivative profiles of the adsorption edge imply a minor shift toward higher energy by desodiation and toward lower energy upon sodiation (Fig. 5-12d). Moreover, from the pre-edge region at ~5467 eV, which represents the forbidden transition from the 1*s* to 3*d* orbitals, the peak increased upon charging and decreased upon discharging, indicating the introduction and disappearance of a hole in the electronic state of V in the 3*d* orbitals. When 1 M $NaPF_6$ in EC:DEC (1:1 by volume) was used (Fig. 5-13), none of the spectra changed during the desodiation/sodiation process, indicating that no reaction occurred during charging/discharging, although a similar valence change was observed in the sodiation/desodiation process.

The *ex-situ* NEXAFS measurements using soft X-rays reveal that the oxidation states of O also changed at the respective states of charge (Fig. 5-12e). The photon energy values in the NEXAFS spectra were corrected on the basis of the binding energy of the adventitious carbon in another synchrotron XPS measurement. Fig. 5-12e shows the O *K*-edge TFY spectrum. The spectral features that originate from O 2*p* orbitals hybridized

with surrounding elements are well known to reflect the electronic states around oxide ions [33,40−42]. The NEXAFS O *K*-edge spectra of $NaV(SO_4)_2$ were likely constructed from the O 2*p* orbitals hybridized with V 3*d* (t_{2g} and/or e_g) and V 4*sp*, and S–O σ-bond signals appeared at approximately 529.6, 531.6, 545, and 538 eV [42]. The peak at 529.6 eV corresponds to the unoccupied hybridized orbital of the O 2*p* orbital and V 3*d* (t_{2g}) orbital [42 − 44], and this peak partially reversibly changed during the desodiation/sodiation process (i.e., increasing in intensity during desodiation and decreasing during sodiation). Meanwhile, the spectra at 538 and 545 eV did not change, and the corresponding hybridized orbitals, which were S–O σ-bonding and O 2*p*–V 4*sp*, respectively, did not play a prominent role in the charge-transfer mechanism. These XANES and NEXAFS measurements imply charge compensation of V and O during the desodiation/sodiation process in $NaV(SO_4)_2$. The *ex-situ* XPS measurements dynamically revealed the redox reaction of V and O (Fig. 5-14). Given the difference in the depth of detection for each measurement (i.e., through the entire sample in the case of XANES-TM, several hundred nanometers to one micrometer in the case of NEXAF-TFY, and several nanometers in the case of XPS), the redox reaction can be assumed to have proceeded best near the electrode surface.

The DFT calculations for the electronic structure support the assigned oxidation state of each element, as demonstrated in Fig. 5-15 for the projected density of states (pDOS) diagrams. The overall diagrams of the pDOS are shown in Fig. 5-16. The pDOS in $Na_xV(SO_4)_2$ reveal that $NaV(SO_4)_2$ holds the V 3*d* and O 2*p* hybridization state just below the Fermi level and that the V–O hybridized bands emerge above the bandgap upon desodiation. Notably, the S bands configurated at the deep level and the S element did not play roles in the charge compensation (Fig. 5-16). In addition, the Bader charge analysis (Fig. 5-17; the raw values are shown in Table 5-2) undoubtedly suggest that

charge transfer occurred at the V–O hybridized orbitals. The Bader charges increased with decreasing amount of Na ions in $Na_xV(SO_4)_2$, and charge compensation by V and O was assumed, whereas V mainly compensated for the charge transfer in the sodiation process from $NaV(SO_4)_2$ to $Na_2V(SO4)_2$. In addition, the magnetic moments (Table 5-2) enable us to estimate the electron configurations of the ions, and the oxidation states of the redox-centric element can therefore be assumed for compositions with various Na contents [45]. In $NaV(SO_4)_2$, the magnetic moment on V is 1.912, corresponding to a *d*-electron configuration of d^2. Upon desodiation, the magnetic moments on both V and O decreased, indicating the oxidation of V and O ions even though the decrease in the magnetic moment in O was not dramatic. These NEXAFS spectral changes and DFT calculation results indicate that charge transfer occurred during the desodiation/sodiation process and provide evidence of charge compensation of V 3*d* and O 2*p*.

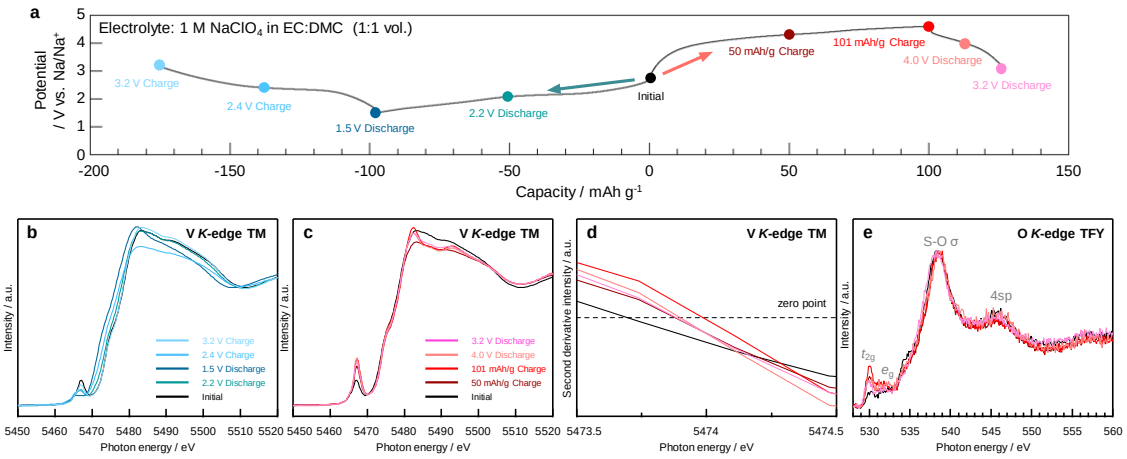

Figure 5-12 (a) Charge/discharge profiles of $NaV(SO_4)_2$ to show the state of charge using 1 M $NaClO_4$ EC:DMC (1:1 vol.). V K-edge XANES spectra of $NaV(SO_4)_2$ at the different charge/discharge states during the first cycle for (b) the sodiation/desodiation process and (c) desodiation/sodiation process from the initial contents. (d) Second derivative profiles

during the desodiation/sodiation process to check the shift of the inflection point at the absorption edge. TM was employed for the XANES measurement. (e) O *K*-edge NEXAFS spectra of $NaV(SO_4)_2$ at the different charge/discharge states during the first cycle for the desodiation/sodiation process from the initial contents. TFY mode was employed for the NEXAFS measurement.

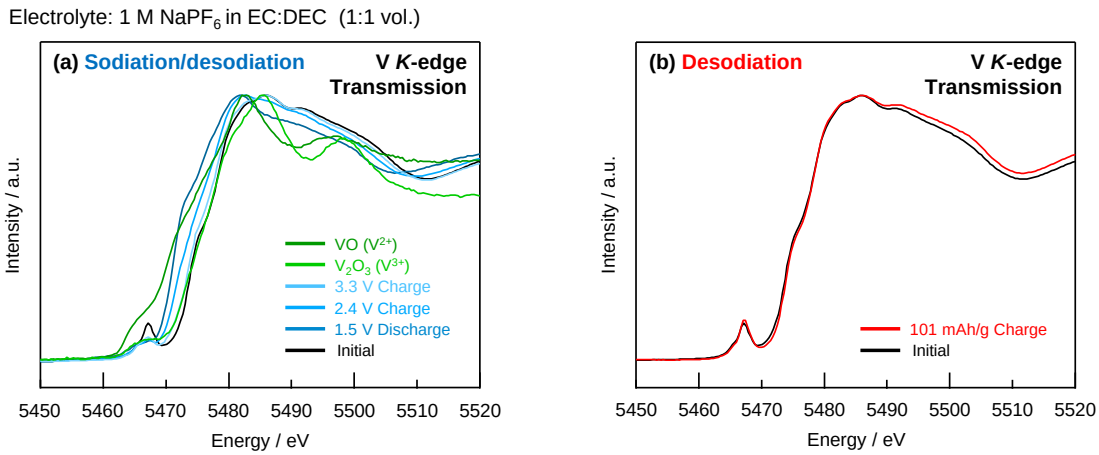

Figure 5-13 V K-edge XANES spectra of $NaV(SO_4)_2$ at the different charge/discharge states during the first cycle for (a) the sodiation/desodiation process and (b) desodiation process from the initial contents using 1 M $NaPF_6$ EC:DEC (1:1 vol.). Transmission mode was employed for the measurement using a hard X-ray.

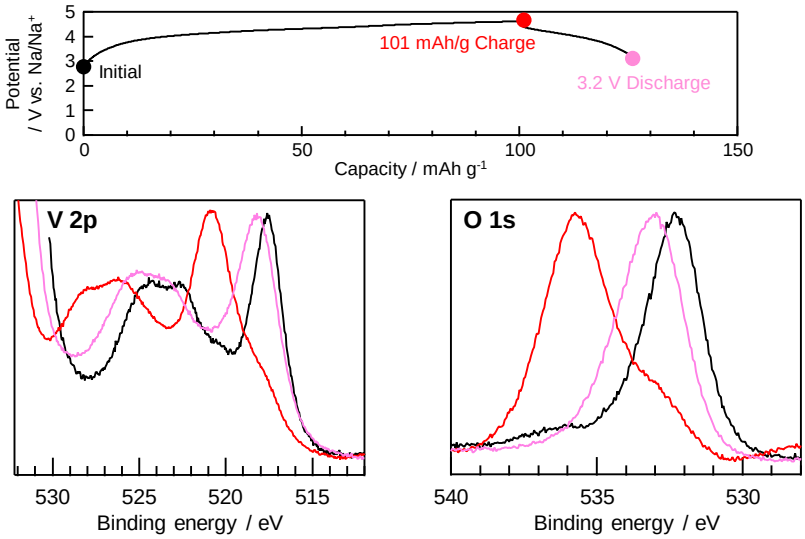

Figure 5-14 *ex-situ* XPS spectra of $NaV(SO_4)_2$ at the different charge/discharge states during the first cycle using 1 M $NaClO_4$ in EC:DMC (1:1 vol.). The measured samples were obtained from the disassembled coin cells after washing by DMC.

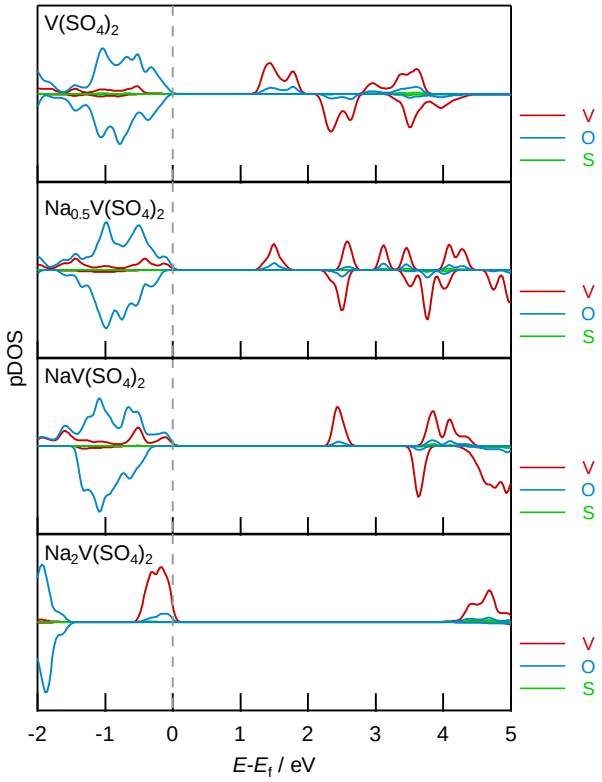

Figure 5-15 Calculated partial density of states (pDOS) for $Na_xV(SO_4)_2$ (x = 0, 0.5, 1, 2) obtained using DFT calculations. The dashed line is the Fermi energy level.

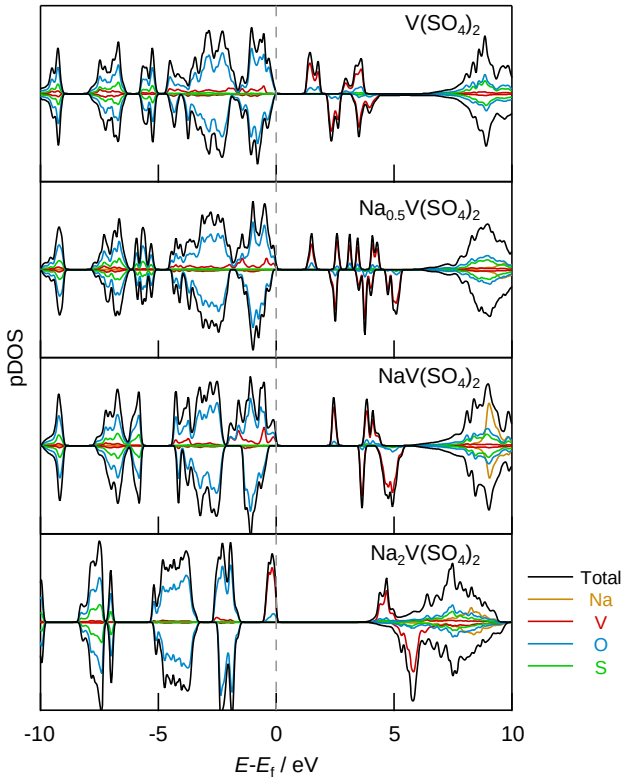

Figure 5-16 Calculated partial density of states (pDOS) for $Na_xV(SO_4)_2$ (x = 0, 0.5, 1, 2) obtained using DFT calculations. The dashed line is the fermi energy level.

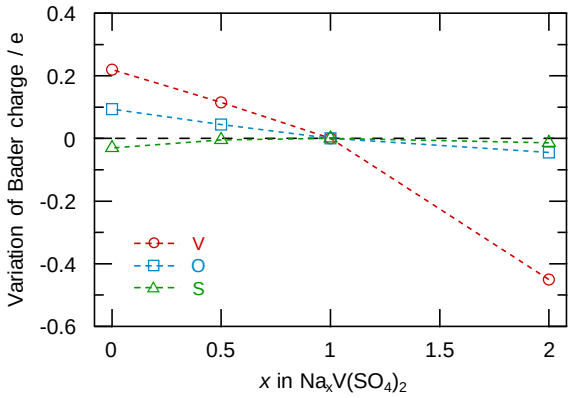

Figure 5-17 Variation of Bader charge for V, O and S in $Na_xV(SO_4)_2$ (x = 0, 0.5, 1, 2) obtained using DFT calculations. The Bader charges were normalized based on the Bader charge of $NaV(SO_4)_2$. Raw data of the Bader charges for O and V are shown in Table 5-2.

Table 5-2 Magnetic moment and Bader charge on V and O sites in $Na_xV(SO_4)_2$ structures (x = 0, 0.5, 1, 2)

	Magnetic moment / μ_B		Bader Charge / e	
	V	O	V	O
$Na_2V(SO_4)_2$	2.752	0	1.574	-1.373
$NaV(SO_4)_2$	1.912	-0.004	2.024	-1.328
$Na_{0.5}V(SO_4)_2$	1.511	-0.013	2.139	-1.284
$V(SO_4)_2$	1.093	-0.018	2.244	-1.234

5.4. Conclusions

Eldfellite-type $NaV(SO_4)_2$ was investigated via experimental measurements and computational calculations. First-principles calculations predicted $Na_xV(SO_4)_2$ to act at an average potential of 2.2 and 4.6 V for the process of $Na_2V(SO_4)_2 \rightarrow NaV(SO_4)_2 \rightarrow V(SO_4)_2$. $NaV(SO_4)_2$ electrochemically delivered a maximum reversible capacity of 77 and 31 mAh g^{-1} with working potentials of 2.1 and 3.9 V for the sodiation/desodiation and desodiation/sodiation processes, respectively. By enlarging the regulation potential to employ a two-step redox reaction, we obtained a maximum discharge capacity of 102 mAh g^{-1}. *Ex situ* XRD measurements revealed phase transitions, including a reversible expansion/contraction or a transformation to an unknown phase, during the charge–discharge process. The charge compensation in the charge–discharge process was carried out by V in sodiation/desodiation and by strong V and small O contributions in desodiation/sodiation. This mechanism was supported by the variation of the pDOS and the Bader charges for $Na_xV(SO_4)_2$.

References

[1] D. Dwibedi, P. Barpanda, *Mater. Today Proc.* **5** (2018) 23439–23442.

[2] W. Pan, W. Guan, S. Liu, B. Bin Xu, C. Liang, H. Pan, M. Yan, Y. Jiang, *J. Mater. Chem. A.* **7** (2019) 13197–13204.

[3] P. Barpanda, J.N. Chotard, N. Recham, C. Delacourt, M. Ati, L. Dupont, M. Armand, J.M. Tarascon, *Inorg. Chem.* **49** (2010) 7401–7413.

[4] R. Tripathi, T.N. Ramesh, B.L. Ellis, L.F. Nazar, *Angew. Chemie - Int. Ed.* **49** (2010) 8738–8742.

[5] P. Singh, K. Shiva, H. Celio, J.B. Goodenough, *Energy Environ. Sci.* **8** (2015) 3000–3005.

[6] P. Barpanda, G. Oyama, C.D. Ling, A. Yamada, *Chem. Mater.* **26** (2014) 1297–1299.

[7] S.C. Chung, J. Ming, L. Lander, J. Lu, A. Yamada, *J. Mater. Chem. A.* **6** (2018) 3919–3925.

[8] C.W. Mason, I. Gocheva, H.E. Hoster, D.Y.W. Yu, *Chem. Commun.* **50** (2014) 2249–2251.

[9] A. Kitajou, H. Momida, T. Yamashita, T. Oguchi, S. Okada, *ACS Appl. Energy Mater.* **2** (2019) 5968–5974.

[10] Y. Uebou, T. Kiyabu, S. Okada, J. Yamaki, *Reports Inst. Adv. Mater. Study, Kyushu Univ.* **16** (2002) 1–5.

[11] R. Rajagopalan, B. Chen, Z. Zhang, X.L. Wu, Y. Du, Y. Huang, B. Li, Y. Zong, J. Wang, G.H. Nam, M. Sindoro, S.X. Dou, H.K. Liu, H. Zhang, *Adv. Mater.* **29**

(2017) 1605694.

[12] Y. Liu, Y. Zhou, J. Zhang, Y. Xia, T. Chen, S. Zhang, *ACS Sustain. Chem. Eng.* **5** (2017) 1306–1314.

[13] R. Fehrmann, S. Boghosian, G.N. Papatheodorou, K. Nielsen, R.W. Berg, N.J. Bjerrum, A.E. Underhill, *Acta Chem. Scand.* **45** (1991) 961–964.

[14] S. Boghosian, R. Fehrmann, K. Nielsen, G. Liptay, R. Snoeck, J. Balzarini, B. Fransson, U. Ragnarsson, G.W. Francis, *Acta Chem. Scand.* **48** (1994) 724–731.

[15] L.L. Driscoll, A.J. Wright, P.R. Slater, *Dalt. Trans.* **47** (2018) 13535–13542.

[16] A. Banerjee, R.B. Araujo, R. Ahuja, *J. Mater. Chem. A.* **4** (2016) 17960–17969.

[17] F. Izumi, K. Momma, *Solid State Phenom.* **130** (2007) 15–20.

[18] K. Momma, F. Izumi, *J. Appl. Crystallogr.* **44** (2011) 1272–1276.

[19] B. Ravel, M. Newville, *J. Synchrotron Radiat.* **12** (2005) 537–541.

[20] E. Kobayashi, J. Meikaku, H. Setoyama, T. Okajima, *J. Surf. Anal.* **19** (2012) 2–5.

[21] E. Kobayashi, D. Yoshimura, H. Setoyama, T. Okajima, *J. Vac. Soc. Japan*. **59** (2016) 341–345.

[22] G. Kresse, J. Furthmüller, *Comput. Mater. Sci.* **6** (1996) 15–50.

[23] G. Kresse, J. Furthmüller, *Phys. Rev. B - Condens. Matter Mater. Phys.* **54** (1996) 11169–11186.

[24] P.E. Blöchl, *Phys. Rev. B.* **50** (1994) 17953–17979.

[25] D. Joubert, *Phys. Rev. B - Condens. Matter Mater. Phys.* **59** (1999) 1758–1775.

[26] J.P. Perdew, K. Burke, M. Ernzerhof, *Phys. Rev. Lett.* **77** (1996) 3865–3868.

[27] S.P. Ong, W.D. Richards, A. Jain, G. Hautier, M. Kocher, S. Cholia, D. Gunter, V.L. Chevrier, K.A. Persson, G. Ceder, *Comput. Mater. Sci.* **68** (2013) 314–319.

[28] K. Okhotnikov, T. Charpentier, S. Cadars, *J. Cheminform.* **8** (2016) 17.

[29] G. Henkelman, A. Arnaldsson, H. Jónsson, *Comput. Mater. Sci.* **36** (2006) 354–360.

[30] W. Tang, E. Sanville, G. Henkelman, *J. Phys. Condens. Matter*. **21** (2009) 084204.

[31] M. Yu, D.R. Trinkle, *J. Chem. Phys.* **134** (2011) 064111.

[32] K. Kawai, W. Zhao, S. Nishimura, A. Yamada, *ACS Appl. Energy Mater.* **1** (2018) 928–931.

[33] K. Kawai, D. Asakura, S.I. Nishimura, A. Yamada, *Chem. Mater.* **33** (2021) 1373–1379.

[34] M. Sun, G. Rousse, M. Saubanère, M.L. Doublet, D. Dalla Corte, J.M. Tarascon, *Chem. Mater.* **28** (2016) 6637–6643.

[35] S.F. Linnell, J.L. Payne, D.M. Pickup, A. V. Chadwick, A.R. Armstong, J.T.S. Irvine, *J. Mater. Chem. A.* **8** (2020) 19502–19512.

[36] Y. Ishado, A. Inoishi, S. Okada, *Electrochemistry*. **88** (2020) 457–462.

[37] Q. Wang, J. Xu, W. Zhang, M. Mao, Z. Wei, L. Wang, C. Cui, Y. Zhu, J. Ma, *J. Mater. Chem. A.* **6** (2018) 8815–8838.

[38] J.N. Chotard, G. Rousse, R. David, O. Mentré, M. Courty, C. Masquelier, *Chem. Mater.* **27** (2015) 5982–5987.

[39] M. Nose, H. Nakayama, K. Nobuhara, H. Yamaguchi, S. Nakanishi, H. Iba, *J. Power Sources*. **234** (2013) 175–179.

[40] D. Asakura, E. Hosono, M. Okubo, Y. Nanba, H. Zhou, P.A. Glans, J. Guo, *ChemPhysChem*. **17** (2016) 4110–4115.

[41] D. Asakura, Y. Nanba, Y. Makinose, H. Matsuda, P.A. Glans, J. Guo, E. Hosono, *ChemPhysChem*. **19** (2018) 988–992.

[42] C.J. Patridge, C. Jaye, T.A. Abtew, B. Ravel, D.A. Fischer, A.C. Marschilok, P. Zhang, K.J. Takeuchi, E.S. Takeuchi, S. Banerjee, *J. Phys. Chem. C*. **115** (2011) 14437–14447.

[43] M. Abbate, H. Pen, M.T. Czyzyk, F.M.F. de Groot, J.C. Fuggle, Y.J. Ma, C.T. Chen, F. Sette, A. Fujimori, Y. Ueda, K. Kosuge, *J. Electron Spectros. Relat. Phenomena*. **62** (1993) 185–195.

[44] Y. Kim, G.Y. Song, R. Nandi, J.Y. Cho, J. Heo, D.Y. Cho, *RSC Adv.* **10** (2020) 26588–26593.

[45] H. Gao, I.D. Seymour, S. Xin, L. Xue, G. Henkelman, J.B. Goodenough, *J. Am. Chem. Soc.* **140** (2018) 18192–18199.

Chapter 6

Conclusions

Against the background of the SDGs issued by the UN in 2015 and the requirement for societies to have a reduced environmental footprint, there is an urgent need to build energy storage systems that can store electricity generated from renewable energy sources and intermittent power sources. Also, there is an immediate need to convert the power sources in gasoline-fueled vehicles to electrical energy sources powered by batteries. Rechargeable batteries are a key technology in energy storage systems, and further development is required. The insertion reaction is a critical part of the operating mechanism of current secondary batteries, and improvements in the performance of insertion compounds will contribute to the growth and uptake of such energy storage devices. This thesis is concerned with phosphate and sulphate materials that undergo insertion reactions in single-phase ASSBs and high-potential cathode materials in NIBs.

As described in Chapter 2, a single-phase all-solid-state battery using a NASICON-type material, $Li_{1.5}Cr_{0.5}Ti_{1.5}(PO_4)_3$, was studied. The primary problem in the commercialization of ASSBs is the resistance at the electrode/solid electrolyte interface. One means of solving this problem is the formation of a dense interface between the electrode and the solid electrolyte. To this end, an *in-situ* formation mechanism can be

used to self-generate the electrode phase from the solid electrolyte. $Li_{1.5}Cr_{0.5}Ti_{1.5}(PO_4)_3$ was adopted for the single-phase ASSB because the material has good ionic conductivity and a large potential gap of 2.2 V between the two redox pairs for Cr^{3+}/Cr^{4+} and Ti^{3+}/Ti^{4+} in line with the potentials of the positive and negative electrodes.

The ionic conductivity of $Li_{1.5}Cr_{0.5}Ti_{1.5}(PO_4)_3$ was estimated to be 2×10^{-4} S cm^{-1} by impedance measurements, which is an excellent value for superior oxide solid electrolytes. It was demonstrated that the *in-situ* formed electrode resulted in a charge-discharge profile with low interfacial resistance, and that the battery could be charged and discharged at a rate of 0.1 mA cm^{-2}, which is high for oxide ASSBs operating at room temperature. Furthermore, it was shown that charging and discharging was possible even at -40°C. From *ex-situ* XPS measurements of charged/discharged samples, the redox couples Cr^{3+}/Cr^{4+} and Ti^{3+}/Ti^{4+} contributed to the charging/discharging in the positive electrode and the negative electrode, respectively.

In Chapter 3, the addition of Li_3BO_3 as an additive to $Li_{1.5}Cr_{0.5}Ti_{1.5}(PO_4)_3$ was used to enhance the ionic conductivity and properties of single-phase ASSBs. Given that $Li_{1.5}Cr_{0.5}Ti_{1.5}(PO_4)_3$ has a high porosity when in pellet form, a key aim was to enhance the electrochemical properties by adding Li_3BO_3, which has a low melting point, to reduce the porosity and increase the relative density. Evaluations using SEM and the Archimedes method showed that the density of the $Li_{1.5}Cr_{0.5}Ti_{1.5}(PO_4)_3$ pellets prepared with Li_3BO_3 was increased compared to those prepared without the addition of Li_3BO_3.

The effect of the addition of Li_3BO_3 was also observed in the electrochemical properties. Impedance measurements were used to estimate the ionic conductivity, which was found to be enhanced from 1.4×10^{-4} S cm^{-1} to 2.6×10^{-4} S cm^{-1} due to the presence of Li_3BO_3 in comparison with the same lot of unmodified $Li_{1.5}Cr_{0.5}Ti_{1.5}(PO_4)_3$ material. Furthermore, the reversible capacity and cycle performance in the charge/discharge

profile were also improved. This enhanced performance was probably because the ion conduction paths were more readily connected due to the denser pellet, and the fact that the reversibility of Li-ion conduction during charging/discharging was increased. The addition of Li-ion-conductive Li_3BO_3 extended the self-discharge time and suppressed electron leakage, suggesting that the ratio of ionic conduction to electrical conduction increased.

In Chapter 4, the effect of the addition of Na_3BO_3 to $Na_3V_2(PO_4)_3$ single-phase ASSBs was investigated. By adding the synthesized Na_3BO_3 to $Na_3V_2(PO_4)_3$, the relative density increased and became a maximum for a 10 wt% addition; however, 5 wt% produced the highest ionic conductivity. The ionic conductivity was improved by about one order of magnitude compared to the $Na_3V_2(PO_4)_3$ pellets without any addition.

Charge-discharge measurements showed that addition of Na_3BO_3 reduced the reversible capacity, but the cycle characteristics were improved; this is a reflection of the higher pellet densification by Na_3BO_3 addition. Optical comparison of the pellets after charging revealed that the $Na_3V_2(PO_4)_3$ pellets by themselves underwent deep *in-situ* electrode formation, while $Na_3V_2(PO_4)_3$ pellets with Na_3BO_3 showed much shallower electrode formation.

In Chapter 5, a novel eldfellite-type cathode material, $NaV(SO_4)_2$, for NIBs was studied. This was designed as a cathode material for NIBs, in which the cell voltage was lower than that for LIBs, in anticipation of the strong inductive effect of sulphate and the multi-step redox reactions of V. It was confirmed that the $NaV(SO_4)_2$ electrode material had average working potentials of 3.9 and 2.1 V vs. Na/Na^+ during the desodiation/sodiation and sodiation/desodiation processes, respectively; and a reversible capacity of about one electron was obtained by operating over a wide potential range.

An *ex-situ* X-ray diffraction study suggested that the change in crystal structure during charging/discharging occurs due to the coexistence of single-phase and two-phase reactions. The oxidation states of $NaV(SO_4)_2$ during charging/discharging are affected by the reversible redox reactions of V^{2+}/V^{3+} during the sodiation/desodiation process; however, in the desodiation/sodiation process, a contribution of V and O to charge compensation was suggested based on consideration of *ex-situ* XAFS measurements using synchrotron radiation. This change in the oxidation states was also supported by the density of states and the Bader charge obtained from DFT calculations.

Acknowledgements

I would like to express my sincere gratitude to Professor Shigeto Okada for his generous guidance in my research program, allowing me to acquire a vast amount of experience and knowledge on the subject matter. His passion for batteries impressed me, and I was fascinated by his interest in battery research.

I sincerely appreciate Professor Atsushi Inoishi for supporting me right from the outset in my battery research to completion of my Ph.D. program. The discussions and suggestions on various materials and ideas on a daily basis were stimulating and established the groundwork for me as a battery researcher.

I express my appreciation to my thesis committee: Professors Michitaka Otaki, Shin Nishimura, and Ayuko Kitajou for helpful discussions and their guidance with my thesis. In particular, I would like to thank Professor Kitajou for her analytical advice since my Master's degree.

I would like to express my gratitude to Professor Ken Albrecht, Drs. Liwei Zhao, Hironobu Hori, Nikolay Dimov, Kosuke Nakamoto, Masaki Furusawa, Masahiro Hokazono, Yuji Ishado and Ryo Sakamoto for all their helpful comments and ideas from various perspectives, and for providing an environment where all researchers can carry out research in the lab without any inconvenience. In particular, I would like to thank Dr. Ryo Sakamoto for his kind support and for providing me with counsel about my research as well as my personal life. I want to express my special gratitude to Dr. Yuji Ishado for gently teaching me the basics of materials for NIBs and DFT calculation methods. I also thank Ms. Miyuki Fujimoto for her kindness and lots of help.

I thank all former and present members of the Okada-Sakaebe-Albrecht Laboratory for their assistance and cooperation; I will always remember the good times I had there.

I appreciate the support given to me by Drs. Eiichi Kobayashi and Hiroyuki Setoyama of the Kyushu Synchrotron Light Research Center for not only assisting in the synchrotron radiation X-ray measurements and analysis of the obtained results, but also for explaining the underlying theory.

I would like to show my gratitude to Professor Duncan H. Gregory, Drs. Cappelluti Mauro Davide, Sen Sudeshna, Fan Chen, and Ms. Siobhan Stevenson at the University of Glasgow for supporting my stay and research in Glasgow, and for continuing to collaborate with me afterwards.

I would like to express my appreciation to Drs. Kazunori Takada, Tsuyoshi Ohnishi, Narumi Ohta, and Shogo Miyoshi at the National Institute for Materials Science (NIMS) for letting me stay and research there for one month. The direct contact with professional researchers at NIMS has made me more self-aware as a researcher.

I am very grateful to Professors Takamasa Sagara, Hiroto Murakami, Hironobu Tahara, and Bun Chen for guiding me through my fourth year of undergraduate study at Nagasaki University. During the year I spent in the Chemistry of Dynamic Molecules laboratory, I found that “Research is Interesting” and it motivated me to pursue my Ph.D.

I would like to thank all the staff and professors of the GA office, and Ms. Rumiko Ide of the ASEM office for supporting me in my PhD program.

I would like to give thanks to my GA course classmates, Drs. Kazuya Ishibashi, Aira Kamito, and Yukun Wang for encouragement to reach this stage of our careers by working together from an early stage to obtain the PhD degree.

Finally, I would like to thank my parents, siblings, grandparents, friends, and wife for countless support; I owe it to them that I am here today.

Akira Nishio

February 2022